Control of Proton Diffusion and Electrical Transport Properties in Transition Metal Oxides Strained Thin Films for Iontronic Switching Device Application

UMAR SIDIK

September 2024

Control of Proton Diffusion and Electrical Transport Properties in Transition Metal Oxides Strained Thin Films for Iontronic Switching Device Application

A dissertation submitted to

THE GRADUATE SCHOOL OF ENGINEERING SCIENCE

OSAKA UNIVERSITY

in partial fulfillment of the requirements for the degree of

DOCTOR OF PHILOSOPHY IN SCIENCE

BY

UMAR SIDIK

September 2024

ABSTRACT

Transition metal oxides with 3*d*-correlated systems have potential to enable densely scaled resistive switching for emerging nonvolatile memory and neuromorphic computing applications. From scientific perspective, the remarkable switching feature in these materials can be attributed to their complex electronic phase diagrams which are extremely sensitive to orbital occupancy of electrons and external stimuli, i.e., proton doping. In recent years, proton doping on perovskite nickelate thin films via gas-phase-chemical reaction (hydrogenation) has been intensively investigated due to its feature to completely reconstruct the electronic band structures, resulting in an immense resistance change of the materials. The vast resistance modulation is thought to be directly related to the proton diffusion within the perovskite lattice of the nickelates. Nevertheless, the nanoscopic understanding of how protons diffuse in these films, especially under intrinsic factors such as lattice strain, has not been clearly revealed. Finding the root correlation between proton diffusion and lattice strain in perovskite nickelates is essential in the field of correlated iontronics. This finding may lead to solve the long-standing issue in resistive switching device area, where a novel approach to enhance the switching operation speed is indispensable.

In this dissertation, I have successfully established the correlation between proton diffusion and lattice strain in strongly correlated perovskite nickelate, namely $NdNiO_3$ thin film, resulting in an enhanced resistance modulation and switching speed. In essence, my achievements are listed in these following points:

(1) I have clearly elucidated the correlation between proton diffusion and lattice strain in $NdNiO_3$ thin film. The experimental results, supported by a first-principle calculation,

provide a deep insight of how protons dynamically behave under a regulated strain in perovskite nickelate lattice.

(2) I have successfully demonstrated that the proton diffusion speed critically affects the resistance state of $NdNiO_3$ thin film. External controls such as electric field and substrate selection were shown to effectively boost the diffusion speed which, in return, results in a remarkable resistance modulation and switching speed.

(3) I have provided a fundamental understanding of strain-controlled proton diffusion, which can lead to an important strategy for overcoming the bottleneck in designing iontronic switching devices.

Contents

CHAPTER 1

General Introduction

1.1. Scope of Study

Among functional materials, strongly correlated RNiO$_3$ (R = rare earth) have attracted particular attention due to their remarkable structural and electronic properties. Such characteristics expands the potential for development of novel protonic device applications. A distinctive feature of this complex 3*d*-correlated system lies on the competition between electronic phases close to phase boundaries, which are often highly sensitive to the motion of interstitial protonic species. In conjunction with the increasing interest in the development of protonic memristive device, recent years have seen great advances of proton-induced electronic transition in RNiO$_3$ thin films. These include investigations of particular RNiO$_3$ materials, fabrication of high quality epitaxial RNiO$_3$ heterostructures, memristive device performance, and synaptic-like characteristics for neuromorphic applications.[1–5] While such efforts have opened up the potential implementation of proton-induced electronic transition, however, elucidation of fundamental phenomena, namely proton diffusion, in this research area is still lacking. Finding the root correlation between proton diffusion in RNiO$_3$ lattice and the corresponding resistance modulation is essential in the field of protonic correlated RNiO$_3$.

In this work, I conducted a systematic study to specifically provide a solution to the long-standing issue in the field of iontronic switching device, namely, relatively slow switching speed compared to that of solid-state electronic device.[6,7] In this regard, enhancement of operating speed is crucially needed to realize a reliable protonic memristive device. For this purpose, I focus on the investigation of the effect of lattice strain to enhance the proton diffusion in NdNiO$_3$ (NNO) thin film. Lattice strain — reported as a principal factor determining the rich landscape of physical properties of RNiO$_3$ — is expected to play a major role in modulating the diffusion behavior of proton.[8–11] The originality of this work lies on the established correlation between the proton diffusion and the regulated lattice strain in RNiO$_3$,

which has been successfully revealed via theoretical and empirical approaches. Following this establishment, I demonstrated this correlation to provide an enhanced proton diffusion resulting in improved performance of protonic memristive device. Moreover, I have successfully shown that the proton diffusion speed critically affects the resistance state of NNO film. External controls such as electric field and substrate selection were shown to effectively boost the diffusion speed which, in return, results in a remarkable resistance modulation. In addition, some analysis techniques were also established in this work. These techniques through both experimental and simulation approaches have successfully elucidated the kinetics of proton diffusion in NNO film. Altogether, this work necessarily fills the void where the fundamental understanding of proton diffusion is lacking nowadays in the field of proton-induced electronic transition of RNiO$_3$. Taking advantage of this set of study, important strategy can be drawn to tackle the bottleneck in the field of iontronic switching device, i.e., enhancement of the relatively slow switching speed.

The general introduction of this work is covered in Chapter 1. This includes the fundamental understanding of perovskite RNiO$_3$, gas-phase annealing proton doping (hydrogenation), and functional protonic memristive device as well as its long-standing issue. The experimental techniques for sample fabrication and characterization are described in detail in Chapter 2. Chapter 3 explains the initial approach and achievement of this work. Here, lattice strain was intentionally regulated into the NNO film for systematic study and analysis. After hydrogenation, I found that lattice strain plays an important role in determining proton diffusion and the consequent electrical behavior. My set of measurements particularly revealed the significance of strain dependence on resistance modulation and proton distribution area. The results were explained and supported by a first-principle calculation study. In Chapter 4, I investigated the effect of electric field on proton diffusion during the catalytic hydrogenation.

By conducting this process together with electric field assist, I was able to demonstrate the correlation between electric field control and proton diffusion in NNO during proton doping process. In more detail, the combination of electric field and gas-phase annealing was shown to enable elegant control of the diffusional proton doping in NNO. Electric field was able to suppress or diffuse proton deeper in the NNO lattice. Completing the aforementioned findings, in Chapter 5, I utilized these knowledges to improve the performance of protonic memristive NNO device. I showed that in addition to electric field control, regulated strain tuning can effectively improve the performance of NNO switching device. This demonstration verified the crucial role of strain engineering in designing a high-performance protonic memristive RNiO$_3$ device. Finally, in Chapter 6, I summarized the scientific achievements of this work and gave a further post-study outlook. In particular, this work could be useful in the future to guide process envelopes for the gas-phase doping and memristive device of perovskites whose properties are sensitive to hydrogen. Additionally, the results of the presented study will enrich the fundamental studies involving both strongly correlated perovskite nickelates and ionic transport.

1.2. Peculiar Property of *R*NiO$_3$ Perovskites and Its Tuning Potential

The discovery of thermally driven metal-insulator transitions (MIT) in the RNiO$_3$ perovskites[12] has stimulated intense researches in this family of materials. Such characteristic expands the potential for the development of novel electronic architectures, where the electronic state transition can be manipulated for resistive switching function. A series of metal-insulator transition temperature (T_{MIT}) for typical RNiO$_3$ materials is shown in **Figure 1.1**.[12] The resistive state changes from metallic to insulating when the temperature reaches its transition point. From scientific perspective, the remarkable MIT in these materials can be attributed to the strong correlations between localized transition metal valence *d* electrons. In

particular, this peculiar feature is extremely sensitive to subtle structural changes, where the electronic phases close to phase boundaries are considerably affected, and that way, a method of fine control via structural engineering is available. For example, the transition temperature (T_{MIT}) between the high-temperature metallic state and the low-temperature insulating state, as shown in Figure 1.1, rises systematically as the rare-earth size becomes smaller.[12] Furthermore, it is evident from **Figure 1.2** that the transitions observed in RNiO$_3$ form a coherent pattern as a function of tolerance factor (t) and <Ni-O-Ni> angle, indicating high dependency of the transitions on structural properties.[13] Here, tolerance factor indicates the tendency of the lattice to distort and is defined as $t = (r_A + r_B) / \sqrt{2}(r_B + r_O)$, where r_A, r_B, and r_O denote the radii of the A, B and O ions of ABO$_3$ perovskites, respectively.

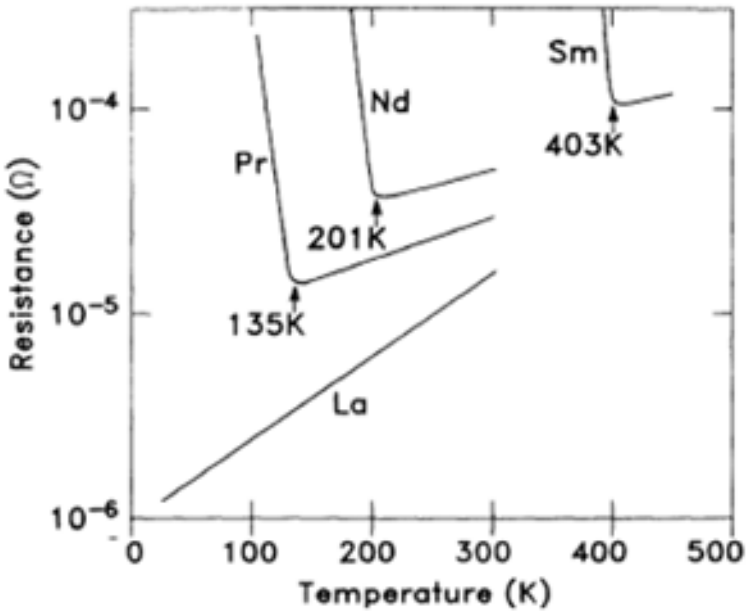

Figure 1.1. Resistivity of La-, Pr-, Nd-, and SmNiO$_3$ showing their metal-insulator transitions.[12]

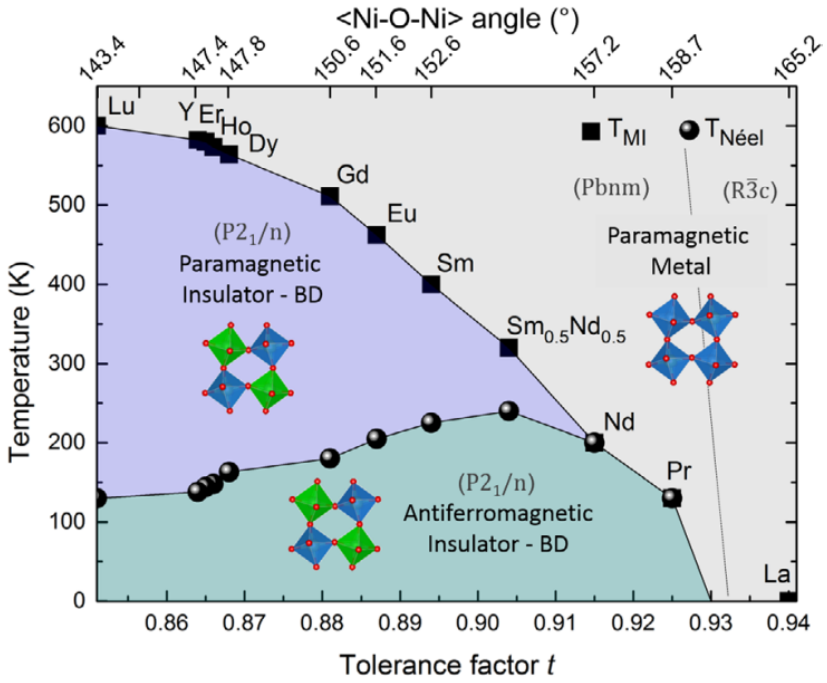

Figure 1.2. Insulator-metal-antiferromagnetic phase diagram for RNiO$_3$ as a function of the tolerance factor and <Ni-O-Ni> angle.[13]

However, despite its potential for future resistive switching device, thermally driven MIT mechanism faces limitations such as operating temperature curb, as well as low resistance modulation magnitude and speed. In this regard, researchers have worked on alternative external stimuli to trigger this transition phenomena, such as via pressure, strain, electrostatic charge, and proton doping.[14–20] Among these approaches, proton doping has been intensively investigated in recent years due to its promising resistance switching control in RNiO$_3$ lattice. Thanks to the corelated system and distinguish structural properties of RNiO$_3$, proton doping can completely reconstruct the electronic band structures resulting in colossal resistance modulation. In conjunction with this, a systematic study of how a subtle change in RNiO$_3$ structure, i.e., lattice strain, may promise a significant improvement of proton-induced mechanism in RNiO$_3$-based resistive switching device.

1.3. Hydrogenation: Proton Doping in *R*NiO_3 via Chemical Gas-Phase Annealing

Resistive state change exploiting abrupt Mott phase transition in strongly correlated *R*NiO_3 has the potential to enable high speed and densely scaled non-volatile memories for emerging neuromorphic computing applications.[21] While the metal-insulator phase transition can be triggered by electrostatic or thermal excitation, ion doping via chemical gas-phase reactions (hydrogenation) as an emerging field can completely reconstruct the electronic band structures by introducing extremely high carrier density resulting in giant resistivity modulation.[22] In recent years, the vast resistivity modulation in the *R*NiO_3 family has been successfully demonstrated through this chemical route. For example, proton-doped $SmNiO_3$ (SNO) thin film, where protons are dissociated from hydrogen molecules by utilizing Pt catalytic effect and then doped into the thin film, can lead to a colossal and reversible resistivity modulation.[23] The colossal resistivity modulation is considered to be governed by proton motion in lattice, such as diffusion in the thin film.

Figure 1.3 schematically illustrates typical hydrogenation process in SNO thin film. The Pt serves as a catalyst, which dissociates hydrogen during hydrogenation process. Firstly, H_2 dissociates to atomic hydrogen at the triple phase boundary (Pt-SNO-H_2/Ar), and then splits to H^+ and e^-, which are incorporated into SNO lattice. Here, H^+ acts as interstitial dopant which can be reversibly intercalated, realizing a sharp phase transition in SNO thin film. On the other hand, e^- from the dissociation process serves as an extra electron in e_g orbital of $Ni^{3+}t_{2g}^6e_g^1$, forming a strongly correlated $Ni^{2+}t_{2g}^6e_g^2$ leading to the emergence of new insulating phase. The schematic electron configuration of this process is illustrated in **Figure 1.4.**

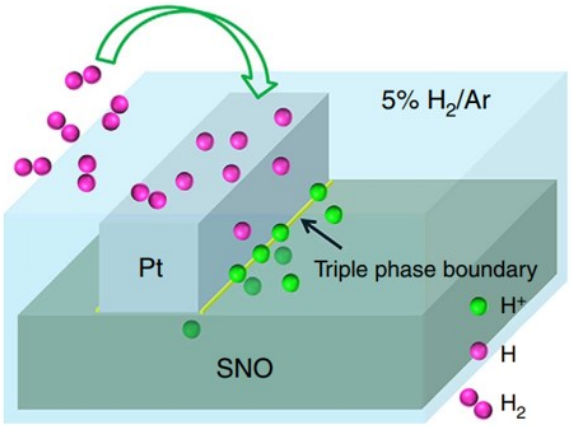

Figure 1.3. Proton intercalation process utilizing Pt-catalytic effect at the triple phase boundary (Pt-SNO-H_2/Ar).[23]

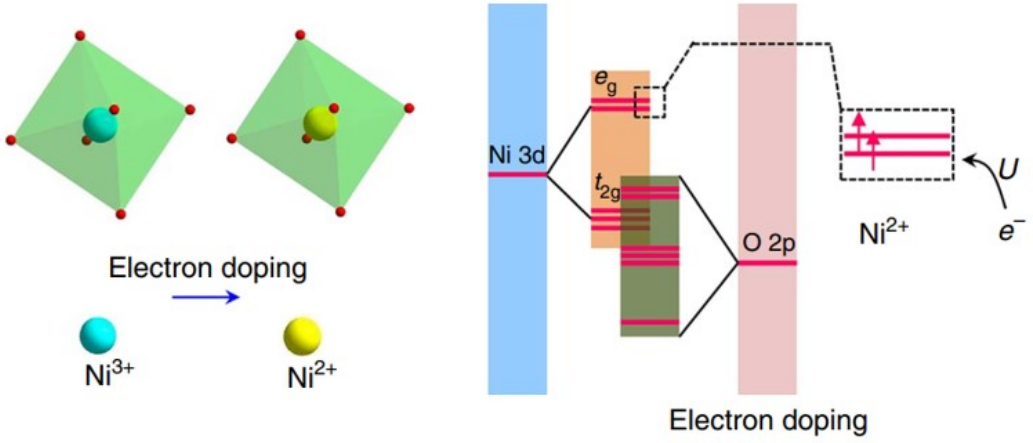

Figure 1.4. Proton intercalation process utilizing Pt-catalytic effect at the triple phase boundary (Pt-SNO-H_2/Ar).[23]

A demonstration of hydrogenation at typical temperature of 473 K can lead to an ~10^8 of giant and reversible resistivity modulation, as shown in **Figure 1.5**a.[23] This colossal resistivity modulation is followed by change of color of SNO film becoming translucent as shown in Figure 1.5b, indicating the emergence of the new insulating phase is caused by the proton diffusion in SNO lattice.[23] An ultra-large and reversible resistivity modulation

demonstrated in this report opened up new directions to explore emerging resistive switching device, where the diffusional proton transport serve as the base principle resulting in large resistance change and band gap modulation.

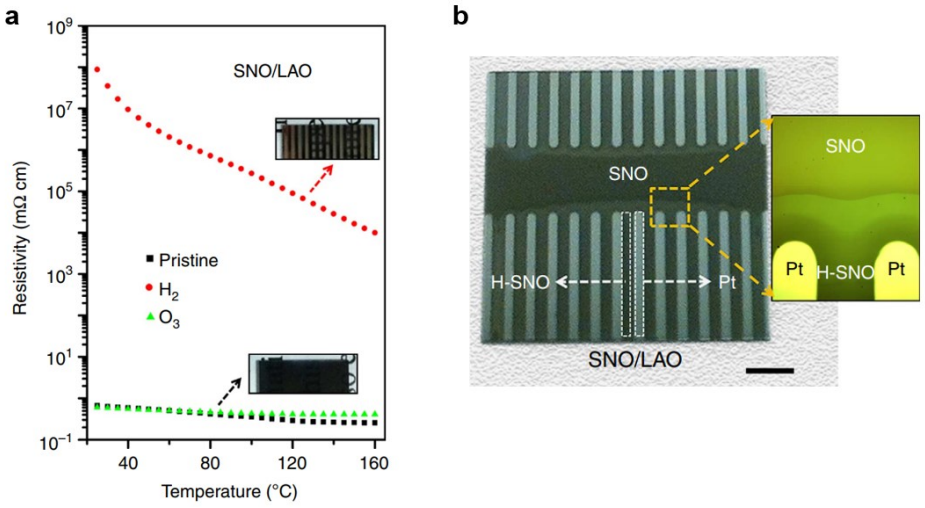

Figure 1.5. (a) Resistivity plotted against temperature for pristine, hydrogenated and ozone-annealed SNO on LAO substrate, respectively, recorded in air. Insets are the corresponding images of the samples.[23] (b) Image of hydrogenated SNO on LAO (Scale bar, 2 mm). The sample shows a dark grey color (which is identical to the pristine one) on the region further away from Pt bars (marked as 'SNO'). In the space between Pt bars (marked as 'H-SNO'), the sample becomes translucent indicating a diffusional proton transport. Right inset shows the optical image of the transient region.[23]

1.4. Functional Protonic Resistive Switching Device: Potential and Challenge

As human civilization enters big data era, high-speed data processing and huge data storage are in great demand nowadays. Resistive switching in oxides has the potential to realize an emerging device with energy-efficient, densely scaled non-volatile memories functions where both memory and computation capabilities are inherent.[24] This device, which usually

involves a metal-insulator-metal structure, can switch its resistance between low resistance state (LRS) and high resistance state (HRS) by migration of ions (protons) through an application of bias voltage. A schematic concept of electric-field-assisted proton migration device is shown in **Figure 1.6**a.[22] Here, electric field induces proton migration in the crystal lattice, leading to modulation of the physical properties. An ion-migration device with in-plane geometry is illustrated in Figure 1.6b.[22] The applied electric field between two electrodes induces the migration of protons and consequently leads to the modulation of the spatial proton distribution. This phenomenon eventually results in the change of resistive state of the device, where non-volatility and abrupt switching characteristics can be observed. Such proton-based resistive switching can be realized by, for example, fabricating in-plane resistive device with asymmetric contacting electrodes of Pt and Au. Utilizing Pt-catalytic effect via the solid-gas interface hydrogenation method, protons can be injected into the channel film only near the Pt electrode, and not in the vicinity of Au electrode. An application of a positive bias at the Pt electrode migrates protons into the entire film leading to an expansion of the hydrogenated area (HRS), while an applied negative bias can reduce the hydrogenated area (LRS). Such function has been demonstrated using, for instance, strongly correlated oxides of SNO with asymmetric contacting electrodes of Pd and Au. Here, Pd serve as hydrogenation catalyst. As shown in **Figure 1.7**, with this setup, multi-state resistive switching across the device has been successfully demonstrated by application of different voltage bias.[25]

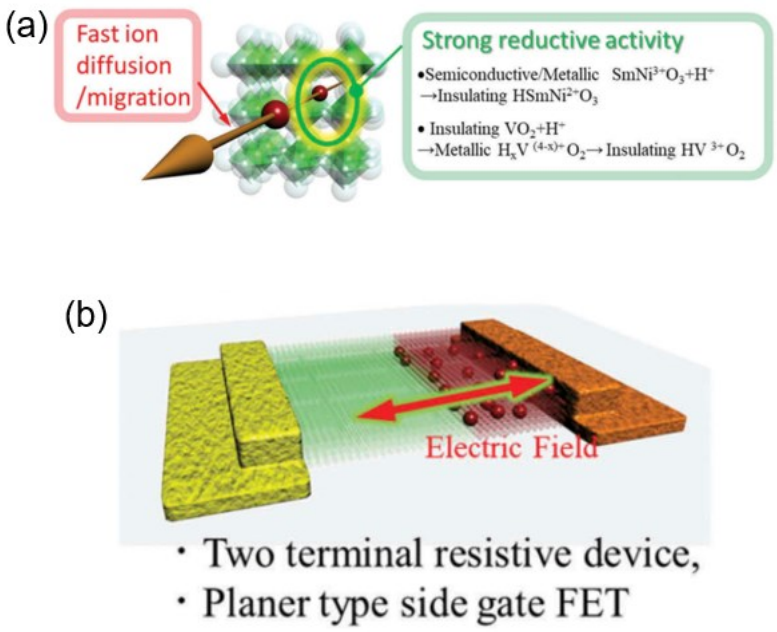

Figure 1.6. (a) Schematic illustration of proton migration under electric field in strongly correlated lattice for resistive switching function. (b) Protonic resistive switching device with in-plane geometry.[22]

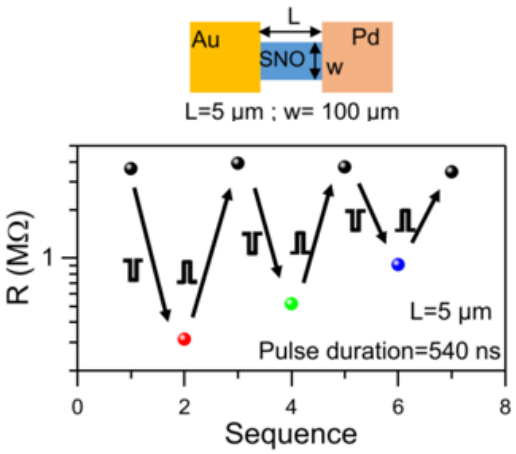

Figure 1.7. Multi-state switching due to re-distribution of protons across the device by application different voltage bias (V = −5.9 V, −7.8 V, −9.6 V for LRS and V = 9.6 V for HRS). Top panel illustrates the dimension of the device.[25]

After years of research, the maturity of the protonic resistive switching device in various applications, i.e., nonvolatile memory and artificial neural networks, could be foreseen. However, at the same time, there is a need to innovate in physical phenomena for state switching and electric-field driven operation of resistive switching devices. In particular, although proton has advantage due to its small radii and high ion mobility compared to other ionic species, its diffusion speed is still subpar for a reliable device performance. For example as shown in **Figure 1.8**, one of its best switching speed ever reported is about ~10^{-7} s, which is about 2 order of magnitude slower than that of typical solid-state electronics (~10^{-9} s).[7] In other words, the switching speed of protonic switching device needs to be enhanced up to the level of that of its counterpart. Future development in this aspect is crucial for the realization of a reliable high-speed and densely scaled non-volatile memory and logic devices.

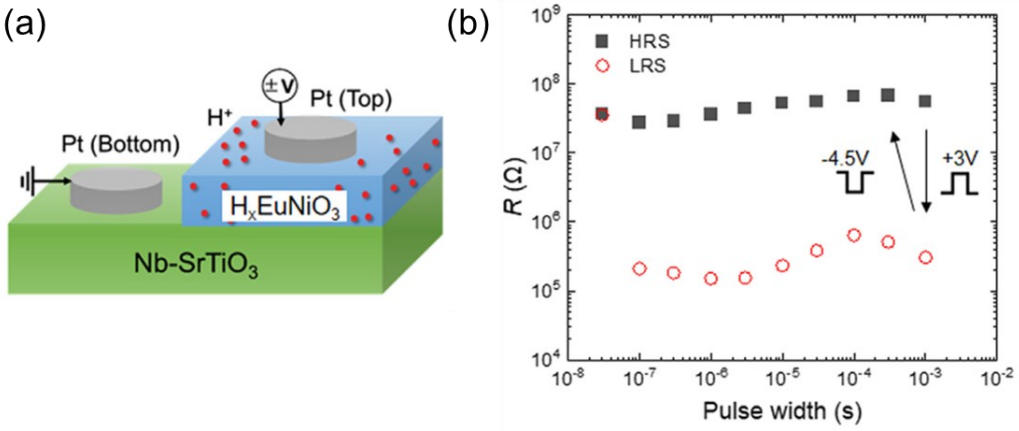

Figure 1.8. (a) Schematic illustration of protonic switching device with top and bottom electrode. The top Pt electrode works as a catalyst as well. (b) Resistance switching measurement with pulse durations of VSET/VRESET = +3.0 V/-4.5 V. The switching speed can reach 10^{-7} s. [7]

1.5. Reference

1) Catalan, G. Progress in Perovskite Nickelate Research. *Phase Transitions.* **2008**, *81.7–8*, 729–749.

2) Ha, S. D.; Aydogdu, G. H.; Ramanathan, S. Metal-Insulator Transition and Electrically Driven Memristive Characteristics of $SmNiO_3$ Thin Films. *Appl. Phys. Lett.* **2011**, *98*, 012105.

3) Meijer, G. I. Who Wins the Nonvolatile Memory Race?. *Science* **2008**, *319*, 1625–1626.

4) Shi, J.; Ha, S. D.; Zhou, Y.; Schoofs, F.; Ramanathan, S. A Correlated Nickelate Synaptic Transistor. *Nat. Commun.* **2013**, *4.1*, 1–9.

5) Ha, S. D.; Shi, J.; Meroz, Y.; Mahadevan, L.; Ramanathan, S. Neuromimetic Circuits with Synaptic Devices Based on Strongly Correlated Electron Systems. *Phys. Rev. Appl.* **2014**, *2*, 064003.

6) Wang, L.; Zhang, Q.; Chang, L.; You, L.; He, X.; Jin, K.; Gu, L.; Guo, H.; Ge, C.; Feng, Y.; Wang, J. Electrochemically Driven Giant Resistive Switching in Perovskite Nickelates Heterostructures. *Adv. Electron. Mater*. **2017,** *3*, 1700321.

7) Taniguchi, Y.; Li, H.B.; Shimoyama, K.; Hattori, A.N.; Tanaka, H. Epitaxial Growth of $EuNiO_3$ On $SrTiO_3$ and Its Application to Stacked Protonation Resistance Switching Devices. *Appl. Phys. Lett.* **2023**, *122*, 263502.

8) Catalano, S.; Gibert, M.; Fowlie, J.; Íñiguez, J.; Triscone, J.M.; Kreisel, J. Rare-Earth Nickelates $RNiO_3$: Thin Films and Heterostructures. *Rep. Prog. Phys.* **2018,** *81*, 046501.

9) Kumar, Y.; Choudhary, R.J.; Sharma, S.K.; Knobel, M.; Kumar, R. Strain Dependent Stabilization of Metallic Paramagnetic State in Epitaxial $NdNiO_3$ Thin Films. *Appl. Phys. Lett.* **2012,** *101*, 132101.

10) Xiang, P.H.; Zhong, N.; Duan, C.G.; Tang, X.D.; Hu, Z.G.; Yang, P.X.; Zhu, Z.Q.; Chu, J.H.; Strain Controlled Metal-Insulator Transition in Epitaxial $NdNiO_3$ Thin Films. *J. Appl. Phys.* **2013,** *114*, 243713.

11) Ojha, S.K.; Ray, S.; Das, T.; Middey, S.; Sarkar, S.; Mahadevan, P.; Wang, Z.; Zhu, Y.; Liu, X.; Kareev, M.; Chakhalian, J. Anomalous Electron Transport in Epitaxial $NdNiO_3$ Films. *Phys. Rev. B*, **2019**, *99*, 235153.

12) Lacorre, P.; Torrance, J.B.; Pannetier, J.S.A.I.; Nazzal, A.I., Wang, P.W.; Huang, T.C. Synthesis, Crystal Structure, and Properties of Metallic $PrNiO_3$: Comparison with Metallic $NdNiO_3$ and Semiconducting $SmNiO_3$. *J. Solid State Chem.* **1991,** *91*, 225.

13) Torrance, J.B.; Lacorre, P.; Nazzal, A.I.; Ansaldo, E.J.; Niedermayer, C. Systematic Study of Insulator-Metal Transitions in Perovskites RNiO$_3$ (R= Pr, Nd, Sm, Eu) due to Closing of Charge-Transfer Gap. *Phys. Rev. B*, **1992**, *45*, 8209.

14) Jaramillo, R.; Schoofs, F.; Ha, S. D.; Ramanathan, S. High Pressure Synthesis of $SmNiO_3$ Thin Films and Implications for Thermodynamics of The Nickelates. *J. Mater. Chem. C*. **2013**, *1*, 2455.

15) Torriss, B.; Margot, J.; Chaker, M. Metal-Insulator Transition of Strained $SmNiO_3$ Thin Films: Structural, Electrical and Optical Properties. *Sci. Rep.* **2017**, *7*, 40915.

16) Newns, D.M.; Misewich, J.A.; Tsuei, C.C.; Gupta, A.; Scott, B.A.; Schrott, A. Mott Transition Field Effect Transistor. *Appl. Phys. Lett.* **1998**, *73*, 780.

17) Asanuma, S.; Xiang, P.H.; Yamada, H.; Sato, H.; Inoue, I.H.; Akoh, H.; Sawa, A.; Ueno, K.; Shimotani, H.; Yuan, H.; Kawasaki, M. Tuning of The Metal-Insulator Transition in Electrolyte-Gated $NdNiO_3$ Thin Films. *Appl. Phys. Lett.* **2010,** *97*, 142110.

18) Ha, S. D.; Vetter, U.; Shi, J.; Ramanathan, S. Electrostatic Gating of Metallic and Insulating Phases in $SmNiO_3$ Ultrathin Films. *Appl. Phys. Lett.* **2013**, *102*, 183102.

19) Chen, J.; Zhou, Y.; Middey, S.; Jiang, J.; Chen, N.; Chen, L.; Shi, X.; Döbeli, M.; Shi, J.; Chakhalian, J.; Ramanathan, S. Self-Limited Kinetics of Electron Doping in Correlated Oxides. *Appl. Phys. Lett.* **2015**, *107*, 031905.

20) Chen, J.; Mao, W.; Gao, L.; Yan, F.; Yajima, T.; Chen, N.; Chen, Z.; Dong, H.; Ge, B.; Zhang, P.; Cao, X. Electron-Doping Mottronics in Strongly Correlated Perovskite. *Adv. Mater.* **2020,** *32*, 1905060.

21) Ielmini, D.; Waser, R. eds. Resistive Switching: from Fundamentals of Nanoionic Redox Processes to Memristive Device Applications. *John Wiley & Sons*. **2015**.

22) Zhang, H.T.; Zhang, Z.; Zhou, H.; Tanaka, H.; Fong, D.D.; Ramanathan, S. Beyond Electrostatic Modification: Design and Discovery of Functional Oxide Phases via Ionic-Electronic Doping. *Adv. in Phys. X*, **2019**, *4*, 1523686.

23) Shi, J.; Zhou, Y.; Ramanathan, S. Colossal Resistance Switching and Band Gap Modulation in a Perovskite Nickelate by Electron Doping. *Nat. Commun.*, **2014**, *5*, 4860.

24) Ielmini, D.; Waser, R. Resistive Switching: From Fundamentals of Nanoionic Redox Processes to Memristive Device Applications. *Hoboken, NJ, USA: Wiley*, **2015.**

25) Ramadoss, K.; Zuo, F.; Sun, Y.; Zhang, Z.; Lin, J.; Bhaskar, U.; Shin, S.; Alam, M.A.; Guha, S.; Weinstein, D.; Ramanathan, S. Proton-Doped Strongly Correlated Perovskite Nickelate Memory Devices. *IEEE Elect. Dev. Lett.*, **2018**, *39*, 1500.

CHAPTER 2

Experiment Techniques

2.1. Sample Fabrication

This section covers the sample fabrication techniques. **Figure 2.1** shows the general process for fabricating typical NNO sample. Generally, this routine consists of film deposition, photolithography, electrode deposition, dry-etching, and lift-off processes. However, a particular step in this process could be skipped or adjusted based on sample design needs. The detail of each step will be described in Sections 2.1.1 and 2.1.2.

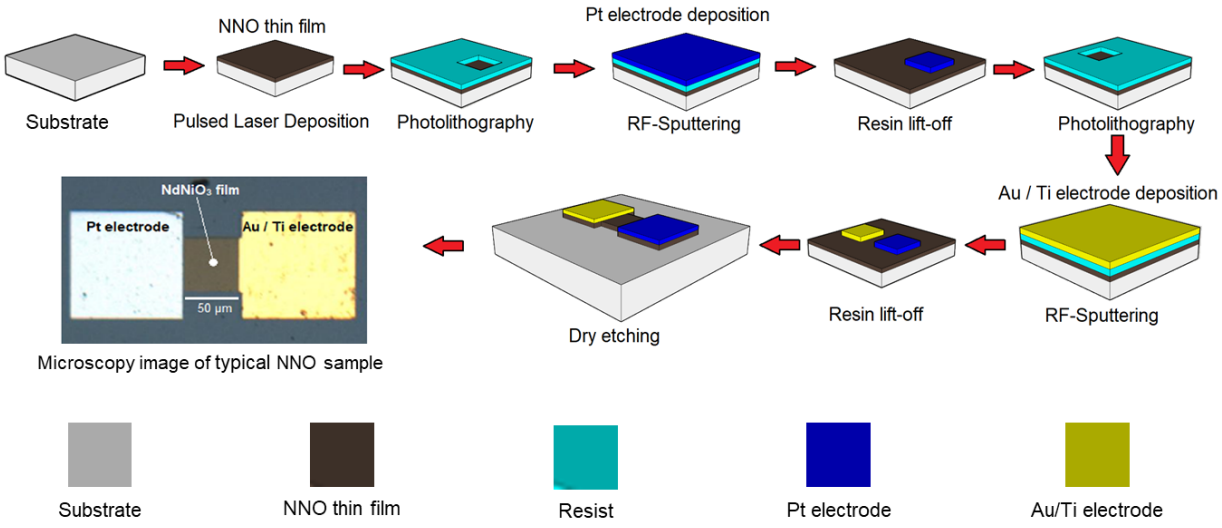

Figure 2.1. General fabrication process for typical NNO sample

2.1.1. Thin Film Deposition

NNO thin films were deposited by pulsed laser deposition (PLD). PLD is a type of physical vapor deposition (PVD) in which a laser having a high-power density and narrow frequency bandwidth is used as a source for vaporizing the desired material. PLD is considered as one of the best methods for high-quality epitaxial film fabrication. The capability of precise control of epitaxial growth of ultra-thin film and stoichiometry transfer between the target material and deposited film are ones among many beneficial characteristics of PLD. The

features of thin film synthesized by PLD are mainly reliant on parameters such as energy fluency, repetition rate, power of peak, cw versus pulse, wavelength oscillation, the composition of the target material, the pressure of the chamber, the flow along with the pressure of the buffer gas, and the distance between the target and the substrates.[1] A high-power laser beam source is placed close to an ultra-high vacuum (UHV) chamber. Inside the vacuum chamber, a target material is placed where the pulsed laser beam is directed. The laser beam then will ablate the target material and create plume where the ablated ions and atomic species are deposited onto the substrate. The illustration of this process is shown in **Figure 2.2**.

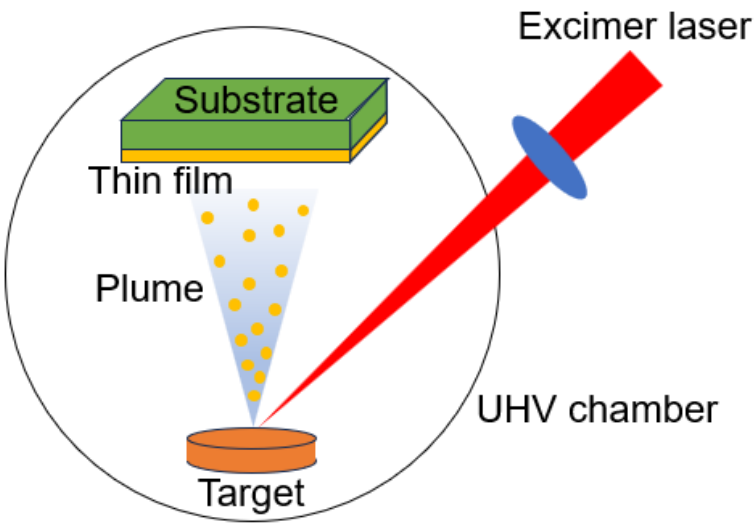

Figure 2.2. Typical laser ablation and plume creation in PLD technique

Figure 2.3 shows typical PLD set-up used in this study. Here, PLD system with ArF excimer laser (λ = 193 nm) was used to deposit NNO thin film. The laser energy was maintained at 90 mJ/pulse with a repetition rate of 3 Hz. The films were deposited at a temperature of 923 K and an oxygen pressure of 30 Pa. Prior to deposition, the growth chamber was evacuated to a base pressure of 1×10^{-6} Pa. In addition, the PLD chamber used in this research has key features such as; the substrate and target position can be adjusted, the deposition angle can be

tilted (0° to 60°), and the azimuth angle of the substrate can be circularly rotated. These features ensure the uniformity and quality of the deposited films.

Figure 2.3. Typical set-up of PLD system used in this study

2.1.2. Thin Film Patterning Process

The as-deposited films were typically patterned afterwards by utilizing photolithography technique (PLS 1000, PMT Corp.). This technique essentially enables fabrication of micrometer-scale patterns on thin film devices. Photolithography draws a pattern on the top of thin film by utilizing the chemical and physical properties of a resist through a reaction with ultra-violet (UV) light.[2] In this sense, the resolution limit of this method is set by the light diffraction. The typical photolithography setup used in this study is shown in **Figure 2.4**. At first, a promotor liquid and resist were spread sequentially and evenly on top of the film

by spin coating method. Then, the sample was baked for about 3 minutes at 95° C. After that, the photolithography process proceeded with a designated pattern by exposing the baked sample to UV light. Finally, the sample was submerged into a developer liquid and then rinsed in DI water.

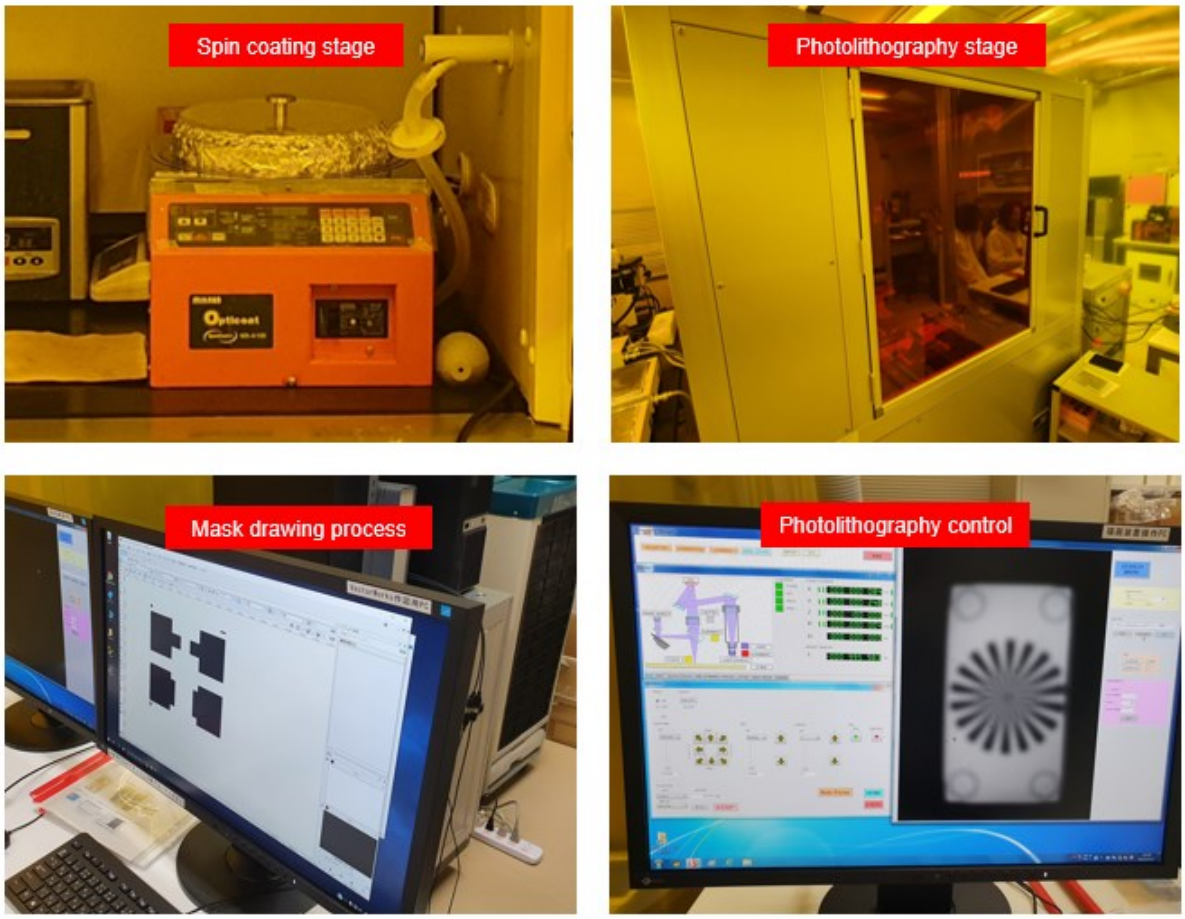

Figure 2.4. Typical lithography setup used in this study

After the film was masked with resist in a designated pattern, then RF-sputtering (SVC-700RFII, Sanyu Electron) was carried out to deposit metal electrode or catalyst on top of it. Depending on the desired pattern, the sample was subsequently dry-etched in between the masking processes using an Ar ion milling system (IBE-KDC75-EPD-OU-TA, Hakuto) to

remove the undesirable thin film or electrode in the sample. The sputtering and ion milling system is shown in **Figure 2.5** and **Figure 2.6**, respectively.

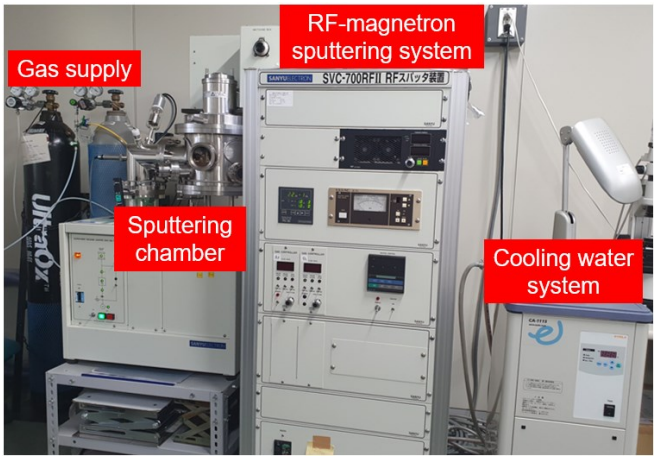

Figure 2.5. Typical RF-sputtering setup used in this study

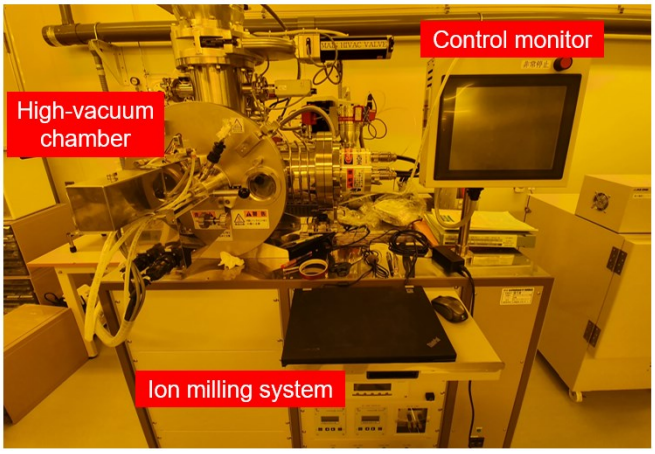

Figure 2.6. Typical ion milling setup used in this study

2.2. Characterization

Figure 2.8 shows a set of characterization tools used in this study. Temperature-dependent resistivity measurement was performed in a range of 10–250 K using a Physical Property Measurement System (PPMS, Quantum Design). Time-dependent two-probe resistance measurement was carried out using a Keithley 2634B source meter in a set of

temperature range to investigate the resistance modulation during hydrogenation and resistive switching operation. The hydrogenation was performed in H_2 gas flow (5% H_2/95% Ar) under atmospheric conditions in an originally developed instrument as shown in **Figure 2.8d**. It was a simple chamber with electrode probes connected to heater, gas source, electrical source meter. This system enables me to perform hydrogenation with simultaneous recording the change in the electrical properties of the film. The proton migration length along the thin film channel was determined using an optical microscope with a minimum length-scale resolution limit of 0.58 μm. The thin films were 2θ-ω-scanned (out-of-plane) using an X-ray diffraction (XRD) system (UltimaIV, Rigaku) to investigate its crystal structure. The diffraction peaks in precise reciprocal space map (RSM) were measured using Cu Kα_1 XRD system (SmartLab, Rigaku) equipped with Ge(220)×2 monochromator, six-axis goniometer, and hybrid pixel two-dimensional detector (775×385 pixels, HyPix-3000, Rigaku). The surface morphology of the films was investigated by atomic force microscope (AFM, AFM5000/AFM5300E, Hitachi High-Tech Science Corporation) and SEM (JSM7610F, JEOL). The film composition was measured using energy dispersive spectroscopy-scanning electron microscopy (EDS-SEM) system (JSM-F100, JEOL).

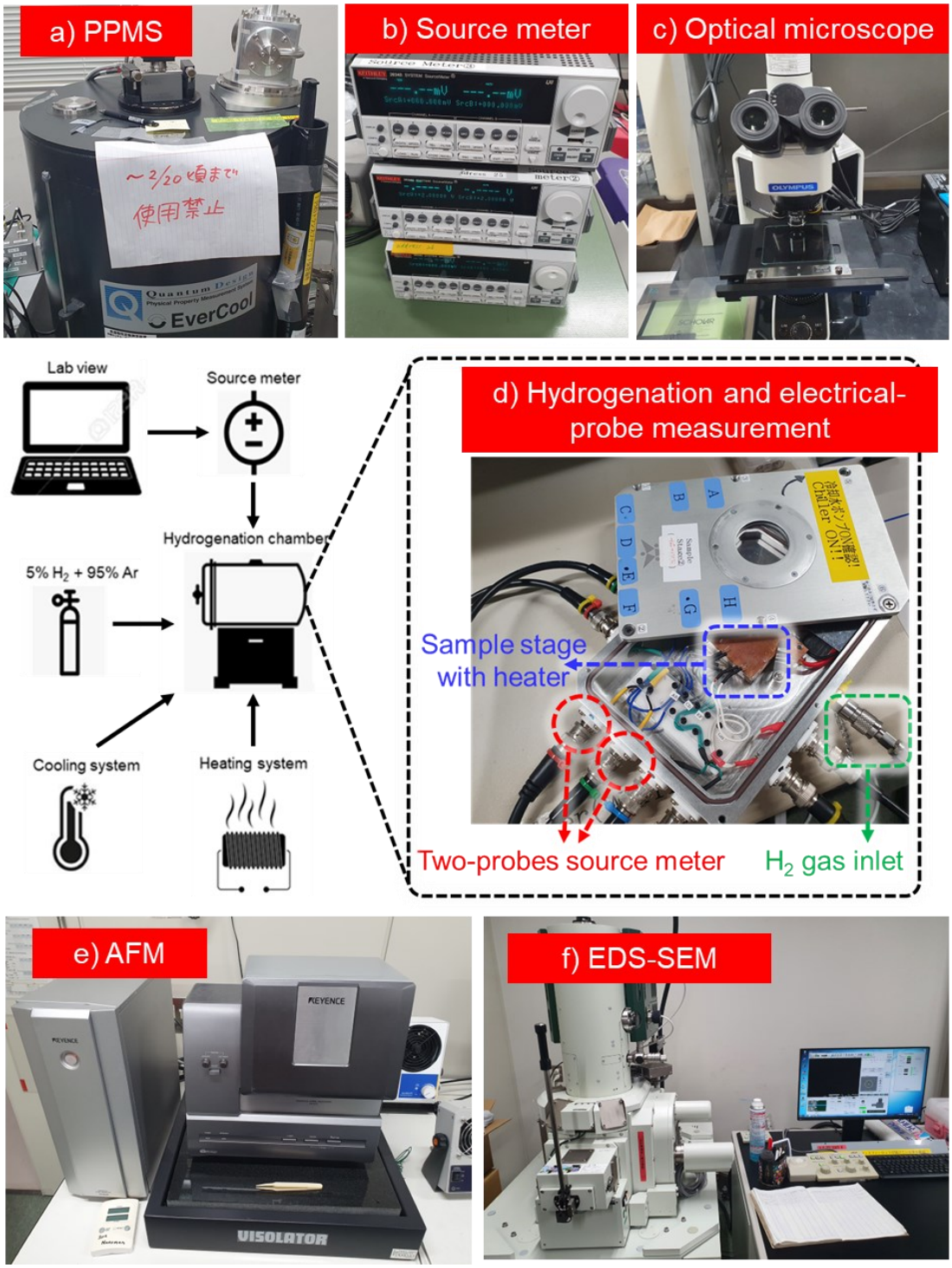

Figure 2.8. Set of characterization tools used in this study. (a) Physical Property Measurement System (PPMS, Quantum Design). (b) Keithley 2634B source meter. (c) Optical microscope. (d) Originally developed instrument for hydrogenation and electrical-probe measurement. (e) atomic force microscope (AFM, AFM5000/AFM5300E, Hitachi High-Tech Science Corporation). (f) SEM (JSM7610F, JEOL) and EDS-SEM (JSM-F100, JEOL) system.

2.3. Reference

1) Pulsed Laser Deposition of Thin Films, edited by Douglas B. Chrisey and Graham K. Hubler, John Wiley & Sons, 1994
2) Willson, C. Grant, Ralph R. Dammel, and Arnost Reiser. "Photoresist Materials: A Historical Perspective." *Metrology, Inspection, and Process Control for Microlithography XI*. Vol. 3050. SPIE, 1997.

CHAPTER 3

Tunable Proton Diffusion in $NdNiO_3$ Thin Films under Regulated Lattice Strains

ABSTRACT

Inspired by the discovery of proton-induced resistance switching in perovskite rare-earth nickelate (RNiO$_3$) films, control of a phase transition via proton doping in strongly-correlated systems is considered as a paradigm to explore emerging iontronics functions. Nevertheless, the microscopic proton dynamics under an intrinsic factor of RNiO$_3$ films, namely, lattice strain, has not been clarified in detail. Here I systematically demonstrate a tunable proton diffusion within the perovskite lattice by regulating structural strain in NdNiO$_3$ (NNO) films. The quantification of the proton dynamics, as well as the corresponding resistance modulation ratio (R_r) and proton diffusion coverage, is found to be significantly sensitive to the strain. Introducing +2.57% in-plane tensile strain into NNO leads to a suppressed proton diffusion, which ultimately results in a fairly small R_r of $\sim 10^2$. In contrast, NNO film with an in-plane compressive strain of −0.03%, of which R_r is $\sim 10^6$, shows a higher degree of proton diffusion. This finding, supported by results of a density functional theory calculation, reveals the role of lattice strain in controlling the proton diffusion in the RNiO$_3$ system and, in a broader context, in designing multifunctional iontronics devices.

3.1. Background

Complex electronic phase transition in 3*d*-correlated systems has great promise in enabling novel resistive switching applications, such as cognitive computing,[1,2] logic-memory,[3,4] photonic,[5,6] and high-performance energy conversion devices.[7,8] From the scientific perspective, the substantial switching feature can be attributed to the metal–insulator transition (MIT), which is exceptionally sensitive to the orbital occupancy of electrons and carrier/ionic doping.[9,10] Compared with doping with other ionic species, proton is particularly fascinating due to its small radii and high ion mobility.[11,12] Therefore, the proton diffusion and distribution

are highly tunable by applying external electric fields.[13] This facile proton-induced MIT can be utilized to realize extremely sensitive correlated-iontronics devices that use proton motion for function. The sharp phase transition and the tuning of resistivity upon proton doping have been conceptually employed to overcome current technological limitations of conventional semiconductors.[14,15] Unlike with prototypical semiconductors, proton interaction with 3*d*-correlated electron systems results in more complex effects as a consequence of the interplay between different degrees of freedom, for example, those of the correlated electronic state.[16] Recent demonstrations of proton-induced phase transition have been reported for 3*d*-correlated electron materials, such as correlated VO_2,[17,18] $SrCoO_x$,[19] and rare-earth nickelates ($RNiO_3$, *R* = rare-earth lanthanide).[13–16,20] Perovskite $RNiO_3$, in particular, is of broad interest owing to its colossal proton-induced resistivity modulation with reversible and nonvolatile switching behavior, which opens up new directions in exploring correlated iontronics devices.[21]

In previous reports, the hydrogenation-induced insulating state of $RNiO_3$ has been widely observed, and considered to be attributed to an abrupt electronic transformation of the e_g orbital of $Ni^{3+}t^6_{2g}e^1_g$ to strongly correlated $Ni^{2+}t^6_{2g}e^2_g$ owing to the injection of an extra electron from the hydrogen dissociation process (hydrogen molecule dissociates into proton and electron).[5–8,14,15,21] Despite inferring the complete reconstruction of electronic band structures, this understanding leaves out the role of the dynamics of a proton acting as an intercalated ion. Apart from this, recent investigations suggest that the rich landscape of the physical properties of $RNiO_3$ is mainly determined by the distorted NiO_6 octahedra networks, leading to feasible tuning of physical properties by structural parameters, such as lattice strain.[22–25] Although previous studies have shown the role of structural properties in the correlated electronic state of $RNiO_3$, none has clearly related or revealed their importance to the proton dynamics within the $RNiO_3$ lattice and the corresponding resistance modulation.

Finding the root correlation between the naturally existing condition in thin films, namely, lattice strain, and the dynamics of the proton-induced resistivity modulation is essential in the field of correlated iontronics.

3.2. Objective

Bulk $NdNiO_3$ (NNO) possesses an orthorhombic perovskite structure, conventionally treated as a pseudocubic (pc) structure, with ordered NiO_6 octahedral networks and Nd cations placed in cavities, as illustrated in Figure S3.1 (see: Supporting information of this chapter). The corner-sharing octahedral networks of NiO_6 forming a Ni–O–Ni open angle ($\theta_{Ni–O–Ni}$) and Ni–O bond length ($d_{Ni–O}$) determine the fundamental physical properties of NNO.[22–25] In this regard, the tuning of the biaxial strain of NNO films is expected to significantly affect not only the static physical properties but also the proton diffusion during catalytic proton doping. In addition, compared with the previously reported $SmNiO_3$ (SNO), which is a typical example of hydrogenated $RNiO_3$ materials, NNO has a lower thermally driven MIT temperature of ~200 K than that of SNO of ~400 K.[26] This essentially means that the as-deposited NNO at and above room temperature possesses a metallic phase, which enables me to examine the hydrogenation-induced MIT in this work. By utilizing the Pt-catalytic effect, which dissociates hydrogen molecules into protons and electrons, I was able to investigate the protonic doping behavior upon chemically driven resistance modulation. In this work, I demonstrate tunable proton doping and the corresponding resistance modulation as a function of regulated lattice strain in NNO thin films. On the basis of the results of our comprehensive study, I found that lattice strain plays a major role in controlling proton diffusion, which ultimately enables a distinct resistance modulation. The migration energy for proton diffusion (E_m) under various strain conditions, calculated via a density functional theory (DFT), shows that lattice strain can effectively tune the migration rate of proton, which supports my experimental results.

3.3. Results and Discussion

Deposition of $NdNiO_3$ (NNO) thin films: Approximately 80 nm-thick NNO films were deposited on (001)-oriented $KTaO_3$ (KTO), $SrTiO_3$ (STO), $(LaAlO_3)_{0.3}$ $(Sr_2AlTaO_6)_{0.7}$ (LSAT), and $(001)_{pseudocubic,\ (pc)}$-oriented $LaAlO_3$ (LAO) by pulsed laser deposition (PLD; ArF excimer, λ = 193 nm). The laser energy was maintained at 90 mJ/pulse with a repetition rate of 3 Hz. The films were deposited at a temperature of 923 K and an oxygen pressure of 30 Pa. Prior to deposition, the growth chamber was evacuated to a base pressure of 1×10^{-6} Pa.

Pattern of Pt catalyst pads: The as-deposited films were masked with a mesh-like pattern by a photolithography technique (PLS 1000, PMT Corp.). Then, RF sputtering (SVC-700RFII, Sanyu Electron) was carried out to deposit Pt on top of NNO films, forming pads of Pt catalyst. Dry etching using an Ar ion milling system (IBE-KDC75-EPD-OU-TA, Hakuto) was carried out to remove the unmasked region of the films. Finally, the resist remaining after the photolithography process was lifted off by submerging the samples in acetone at a temperature of 343 K for about 1 h.

Hydrogenation and characterization: The as-deposited NNO films were 2θ-ω-scanned (out-of-plane) using an X-ray diffraction (XRD) system (UltimaIV, Rigaku). Temperature-dependent resistivity (ρ–T) of the films was measured using a physical property measurement system (PPMS, Quantum Design) during cooling and heating cycles in the range of 10–250 K. The films were hydrogenated in H_2 (5% H_2–95% Ar) with gas flow rate of 100 mL/min under atmospheric conditions at a temperature of 473 K. During this process, the time-dependent two-probe resistance measurement was carried out using a source meter (2634B, Keithley). The proton diffusion region, which is represented by the optically translucent area of NNO films, was examined using an optical microscope with the minimum length-scale resolution

limit of 0.58 μm. The diffraction peaks in precise reciprocal space map (RSM) were measured using Cu Kα_1 XRD system (SmartLab, Rigaku) equipped with Ge(220)×2 monochromator, six-axis goniometer, and hybrid pixel two-dimensional detector (775×385 pixels, HyPix-3000, Rigaku). The precise RSMs were taken at 0.02° step in both 2θ and ω, using a one-dimensinoal mode, leading to the resolution of 0.0001–0.0002 Å^{-1} in RSM. The wide RSMs using Cu Kα without the monochromator were taken with scanning $2\theta/\omega$ from 15° to 120° at fixed χ from -5° to 65° (5 steps) in a two-dimensional mode of the detector.

3.3.1. Substrate-Dependent Resistance Modulation

To introduce different degrees of biaxial strains in the perovskite lattice, NNO films were deposited on various substrates with different lattice constants (Table S3.1), namely, KTO, STO, LSAT, and LAO, by pulsed laser deposition (PLD). 2θ-ω X-ray diffraction (XRD) curves of the deposited films show a $(002)_{pc}$ NNO peak near the $(002)_{(pc)}$ substrate peak (Figure S3.2). This shows that the deposited NNO films underwent *c*-axis-oriented growth along the out-of-plane direction regardless of the substrate. In addition, all NNO films were also epitaxially grown along the in-plane directions as demonstrated by wide reciprocal space maps (RSMs) (Figure S3.3), where $h0\ell_{pc}$ and $hh\ell_{pc}$ peaks of NNO were synchronized to $h0\ell_{(pc)}$ and $hh\ell_{(pc)}$ of the substrates in in-plane.

The intrinsic electrical properties of the grown films were investigated by examining temperature-dependent electrical resistivity (ρ–T), as shown in Figure S3.4. The result indicates that the MIT characteristics of the as-deposited NNO films vary depending on the substrate. To investigate the effect of each substrate on the catalytic proton doping process, a pattern of Pt catalyst pads was deposited on the surface of the as-deposited NNO films. The configuration of the Pt–NNO–substrate samples is shown in Figure S3.5. In this configuration, hydrogen

molecules first dissociate into atomic hydrogens, owing to the Pt-catalytic effect at the triple-phase boundary of Pt–NNO–H_2.[21] Then, they split into protons and electrons that are then incorporated into the NNO lattice. The hydrogenation was performed by placing the samples inside a chamber, then exposing them to H_2 gas (5% H_2–95% Ar) with a flow rate of 100 mL/min. The process proceeded preferentially at an elevated temperature of 473 K owing to the thermally assisted diffusion, enabling us to easily recognize the diffusional proton transport.[14]

The time-dependent resistance measurement, whose set-up is illustrated in Figure S3.5, was carried out to investigate the proton diffusion and the corresponding resistance modulation during hydrogenation. **Figure 3.1**a shows the real-time evolution of the resistance modulation ratio (R_r) during the hydrogenation; R_r is described as the resistance at time t divided by the initial resistance at $t = 0$, ($R_{(t)} / R_{(0)}$). Initially, R_r barely increases at $t < 3$ min, showing a short delay attributed to the hydrogen dissociation and adsorption before it can be incorporated into the NNO lattice.[13] R_r then drastically increases for ~25 min, after which it reaches an almost constant value of more than 10^2 and 10^3 for NNO deposited on KTO (NNO/KTO) and STO substrates (NNO/STO), respectively. The abrupt increase in R_r in NNO grown on LSAT (NNO/LSAT) and LAO (NNO/LAO) progresses longer than in that grown on STO and KTO. Herein, although R_r shows a noticeable evolution throughout the entire hydrogenation duration, the rapid increase starts to slow after ~40 min; after ~120 min, final modulation ratio becomes more than 10^5 and 10^6 for NNO/LSAT and NNO/LAO, respectively. The resistance modulation corresponds to the hydrogenated NNO film (HNNO) which, according to this observation, can be tuned by selecting an appropriate substrate. The reversibility and stability of the proton-induced resistance modulation are shown in Figure S3.6.

Figure 3.1b shows the microscopy image of NNO on each substrate after 120 min of hydrogenation. The apparent translucent yellow color in the vicinity of the Pt pads represents the occurrence of diffusional proton transport in HNNO, because as the doping progresses, a large band gap opens up making the film optically translucent.[13,21] From this, it is confirmed that the hydrogenated region varies for each NNO film depending on the substrate. The narrowest HNNO area is observed on NNO/KTO where a broad portion of undoped NNO retains its dark color. The HNNO area becomes notably broader on NNO/STO as the dark NNO region gradually shrinks. The expansion of the HNNO area on NNO/STO is followed by that on NNO/LSAT and then finally on NNO/LAO where the dark NNO eventually disappears. From Figures 3.1a and 3.1b, both the increasing R_r and the expanding HNNO area show an identical trend; the highest values of both are observed on NNO/LAO, followed by those on NNO/LSAT, NNO/STO, and NNO/KTO in this sequence. This demonstrates an established correlation between resistance modulation and proton migration in correlated perovskite oxides, which intriguingly, from both scientific and technological perspectives, can be finely tuned via regulated lattice strain.

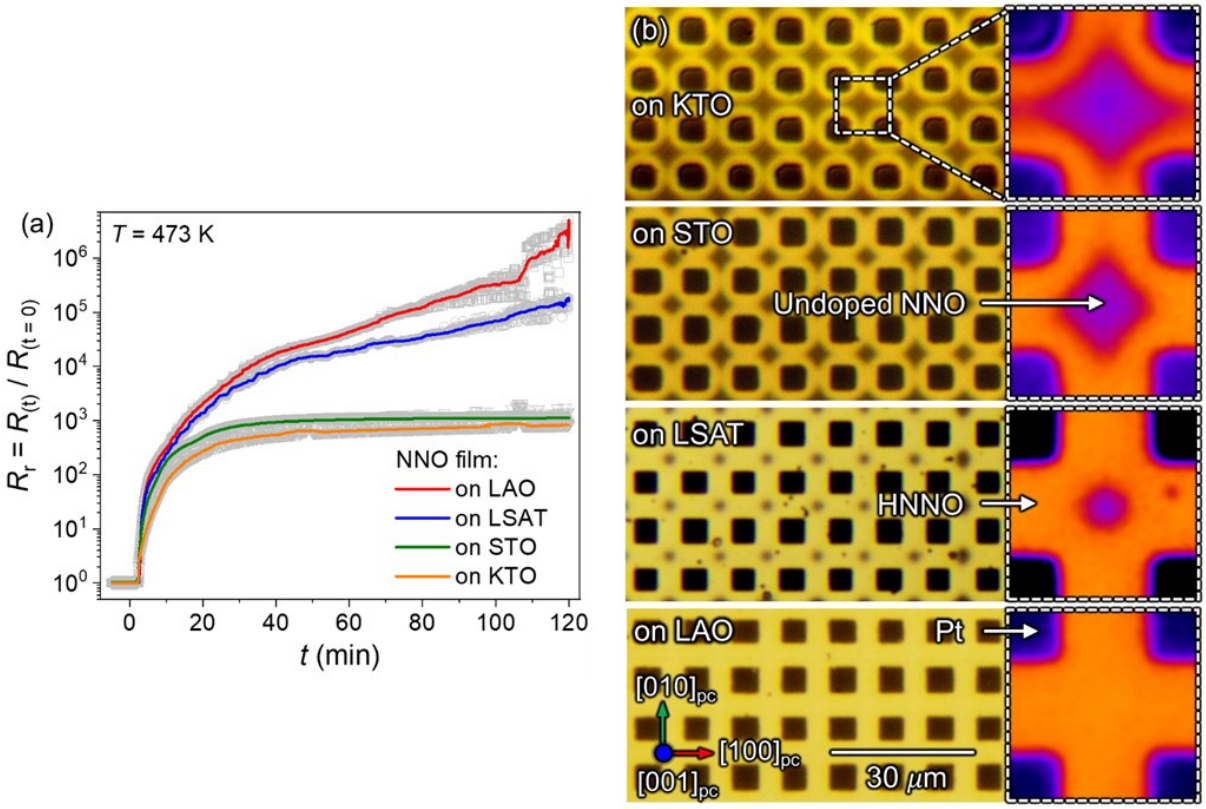

Figure 3.1. Catalytic proton doping of NNO films on LAO, LSAT, STO, and KTO substrates. (a) Real-time evolution of resistance modulation ratio (R_r) during hydrogenation. The raw data represented by the gray symbols were smoothed into the line graphs using a 50% percentile filter in OriginLab.[27] (b) Corresponding microscopy images of the samples after 120 min of hydrogenation. The difference in brightness of the translucent HNNO area among samples originated from the optical characteristics of the substrates. The color conversion (right panel) was carried out by applying a selected lookup table in ImageJ to the corresponding grayscale image.

3.3.2. Precise Observation of Structural Properties

To further investigate the effect of lattice mismatch-controlled structural strain on hydrogenation, a two-dimensional precise RSM measurement was carried out around 103_{pc} diffraction peaks (one of the peaks in wide RSMs in Figure S3.3a) of the NNO films on

different substrates under pristine and hydrogenated conditions. Relative to the lattice constant of bulk NNO ($a_{\text{pc, NNO-bulk}}$ = 3.807 Å), the lattice mismatch at the film–substrate interface, defined as (($a_{\text{pc, substrate-bulk}} - a_{\text{pc, NNO-bulk}}$) / $a_{\text{pc, NNO-bulk}}$) 100%, has tensile strains of +4.78%, +2.57%, and +1.60%, and a compressive strain of −0.47% for NNO/KTO, NNO/STO, and NNO/LSAT, and NNO/LAO, respectively. Diffractions for the pristine films are shown in **Figure 3.2**a as a function of in-plane ($Q_{/\!/}$, in substrate $[100]_{(pc)}$ direction) and out-of-plane ($Q_{\perp}$, in substrate $[001]_{(pc)}$ direction) reciprocal lattice distances. The yellow stars in Figure 3.2a, which mark the corresponding film peaks, are located in the vicinity of the in-plane reciprocal lattice rods (red dashed lines) of LAO, LSAT, and STO substrates caused by crystal truncation rod scattering.[28] This indicates that the epitaxially grown NNO films are well strained along the in-plane direction. The magnified RSMs of Figure 3.2a and the NNO peak positions are shown in Figure S3.7 and Table S3.2, respectively. Indeed, I can confirm that the in-plane peak position (a_{pc}*) of NNO 103_{pc} is well controlled by the substrates. In addition, I also confirmed that the epitaxial NNO films have homogeneous strain and the peaks are originated from the crystalline domain size (Figure S3.8).

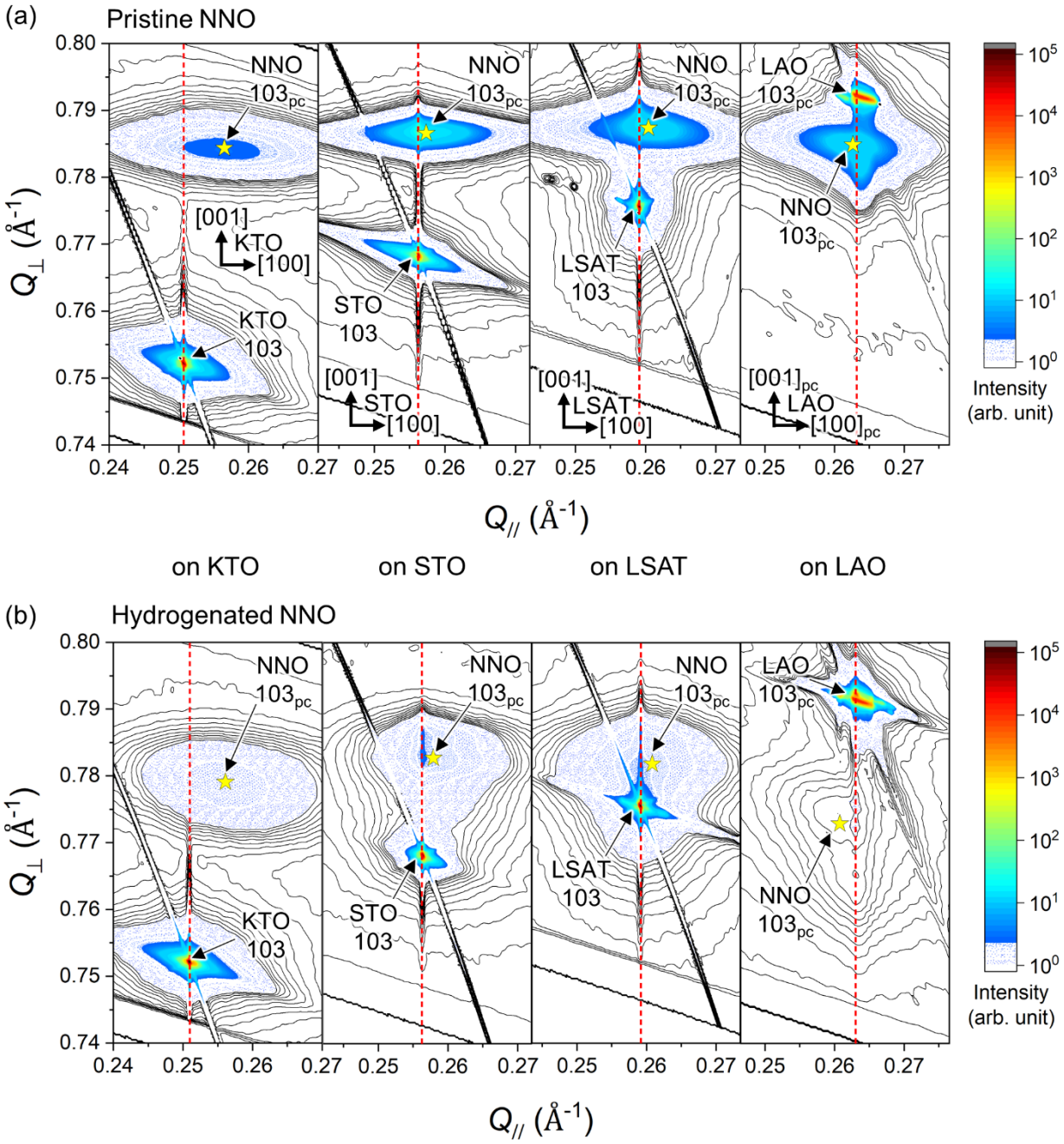

Figure 3.2. Precise RSM around $103_{(pc)}$ diffraction peaks of (a) pristine and (b) hydrogenated NNO films on KTO, STO, LSAT, and LAO substrates. $Q_{/\!/}$ and $Q_{\perp}$ represent the in-plane and out-of-plane directions in the reciprocal space map, respectively. The red dashed lines indicate the in-plane reciprocal lattice rods of the substrate surfaces. The yellow stars mark the 103_{pc} peak at $(Q_{/\!/}, Q_{\perp}) = (a_{pc}^*, 3c_{pc}^*)$ of the corresponding NNO films.

I noticed in Figure 3.2a that in addition to a_{pc}*, the out-of-plane peak positions ($3c_{pc}$*) of NNO 103_{pc} also change with different substrates. The measured values of a_{pc}* and $3c_{pc}$* are listed in Table S3.2. The measured in-plane (a_{pc}) and out-of-plane (c_{pc}) lattice constants of NNO films, of which are the inverse of a_{pc}* and c_{pc}*, respectively, are shown in **Figure 3.3**a as a function of bulk lattice constants of the substrates. a_{pc} of NNO/LAO is located below $a_{pc,\ bulk}$, which is different from a_{pc} of NNO/LSAT, NNO/STO, and NNO/KTO. This confirms that the distributed biaxial strain of the film, defined as $\varepsilon_{//} = ((a_{pc} - a_{pc,\ NNO\text{-}bulk}) / a_{pc,\ NNO\text{-}bulk})\ 100\%$, is compressive for NNO/LAO and tensile for NNO/LSAT, NNO/STO, and NNO/KTO, with $\varepsilon_{//}$ values of about −0.03%, +0.82%, +2.02%, and +2.57%, respectively. A film with a compressive strain ($a_{pc} < a_{pc,\ NNO\text{-}bulk}$) will generally exhibit $c_{pc} > c_{pc,\ NNO\text{-}bulk}$, whereas a tensile-strain film ($a_{pc} > a_{pc,\ NNO\text{-}bulk}$), in contrast, will exhibit $c_{pc} < c_{pc,\ NNO\text{-}bulk}$ owing to the elastic deformation of the lattice.[29] This tendency holds true for our compressive NNO/LAO film where c_{pc} is observed to be greater than that of bulk NNO. However, for the tensile NNO/LSAT, NNO/STO, and NNO/KTO films, the corresponding c_{pc} is greater than that of bulk NNO. This indicates that, compared with the tensile NNO in this experiment, my compressive film has better constraint to maintain the elastic deformation of the perovskite NNO lattice. The degree of deformation was estimated by calculating the pseudocubic lattice constant (a_0) that would correspond to that of the strained NNO film.

$$a_0 = \frac{2v a_{pc} + (1 - v) c_{pc}}{1 + v} \qquad (3.1)$$

Here, v is Poisson's ratio, which was set to be 0.30 for all films.[30–32] The results presented in Figure 3.3a show that a_0 closest to the bulk NNO value was obtained in compressive NNO/LAO. Moreover, a_0 deviated further from the bulk value as the tensile strain sequentially increased in NNO/LSAT, NNO/STO, and NNO/KTO in this sequence.

The lattice constants of the films change after hydrogenation since, as shown in Figure 3.2b, the HNNO diffractions move downwards from their initial positions (decreasing c_{pc}*, Table S3.2), resulting in increasing c_{pc}. This result demonstrates that an unavoidable structural change occurred during the incorporation and the transient diffusion of protons. Furthermore, the elongation of the perovskite cell upon hydrogenation preferentially occurs in c_{pc} over a_{pc} (details are shown in Figure S3.7 and Table S3.3). A similar tendency has been reported by He *et al.*; however, instead of hydrogenation, they investigated the phase transition and the corresponding structural change as a function of temperature.[33] The dominant change of c_{pc} was attributed to the clamping effect of a_{pc} by the substrate, leaving c_{pc} as the only variable responsible for the volume change across the phase transition. This, with regard to my results, indicates the importance of the substrate-dependent constraint in controlling the change in the structure and, in addition, the corresponding physical properties of NNO films upon hydrogenation.

3.3.3. Dominant Factor Rendering Colossal Resistance Modulation

The effect of the substrate dependence was then investigated for the hydrogenated samples. Figure 3.3b outlines this dependence on R_r and proton diffusion. Herein, the proton diffusion is represented by the estimated percentage of the HNNO translucent area (A) from Figure 3.1b. It is clear that the compressive film shows higher R_r and A than the tensile films. The tendency of A (proton coverage area) and R_r (proton-induced resistance modulation) well agreed against the lattice constant shown in Figure 3.3b, and this agreement implies that resistance modulation is dominated by proton diffusion length with the similar proton concentration in all NNO thin films. Namely, amount of protons is similar level in the protonated regions independent from lattice constant with negligible crystalline boundary effects.[34] Moreover, these values decrease with increasing tensile strain, which, as

demonstrated in Figure 3.3a, leads to a greater deviation from the bulk NNO lattice. This clearly indicates the importance of the bulk NNO perovskite structure, which can be finely tuned by adjusting the substrate conditions, in enabling the proton diffusion and the corresponding insulating state.

I continued our analysis by investigating the dominant structural factor rendering the colossal R_r. Typically, the strain in perovskite RNiO$_3$ is accommodated by the changes in $d_{Ni–O}$ and $\theta_{Ni–O–Ni}$.[9,10,22–25,29,35] May *et al.* conducted a high-flux XRD study and they reported that the strain strongly modifies the in-plane Ni–O bond length ($d_{Ni–O,\,//}$), whereas the in-plane Ni–O–Ni open angle ($\theta_{Ni–O–Ni,\,//}$) is insensitive to the strain.[36] Consequently, this leaves the modified $d_{Ni–O,\,//}$ as the dominant parameter in compensating for the structural deformation in the in-plane direction. In this regard, and since Figure 3.1b represents the in-plane diffusion of protons, here I attempted to estimate $d_{Ni–O,\,//}$ of our pristine film using the equation $d_{Ni–O,\,//} = a_{pc} / 2 \sin(\theta_{Ni–O–Ni,\,//} / 2)$, where $\theta_{Ni–O–Ni,\,//}$ is assumed to equal 157.1° of the bulk NNO.[37] The estimated $d_{Ni–O,\,//}$ is plotted against R_r in Figure 3.3c. NNO/LAO has the smallest $d_{Ni–O,\,//}$ of 1.941 Å, closest to that of bulk NNO of 1.942 Å. The estimated value increases to 1.958 Å, 1.982 Å, and 1.988 Å for NNO/LSAT, NNO/STO, and NNO/KTO, respectively. This enables us to observe the tendency of R_r with respect to $d_{Ni–O,\,//}$; where a pristine NNO film having shorter $d_{Ni–O,\,//}$ enables a higher proton distribution, resulting in a larger R_r. To further explain this tendency, a simulation based on a first-principles study is presented.

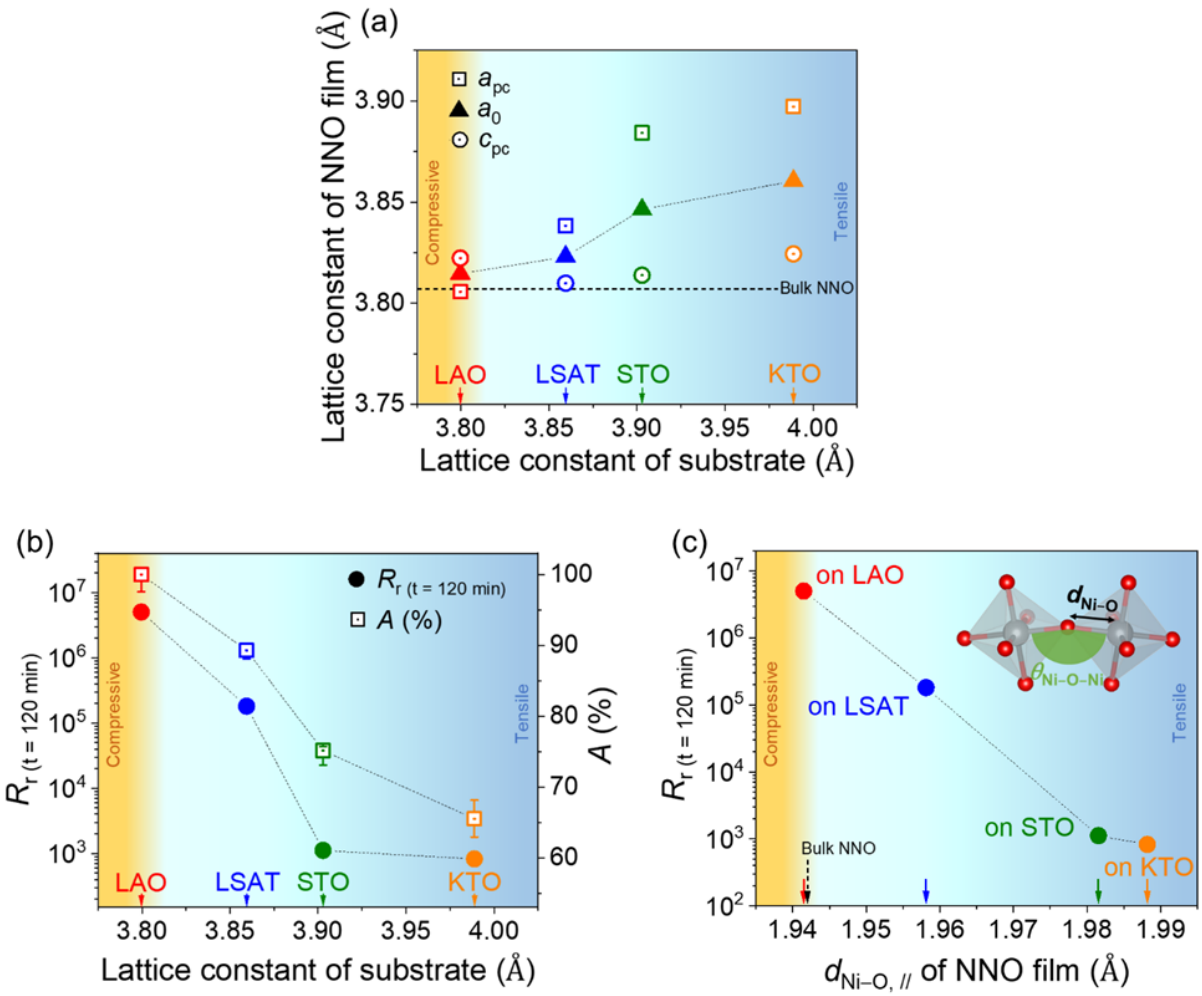

Figure 3.3. (a) In-plane (a_{pc}) and out-of-plane (c_{pc}) lattice constants of pristine NNO films deposited on LAO, LSAT, STO, and KTO substrates. a_0 represents the pseudocubic lattice constants of the strained films. (b) Plot of proton-induced resistance modulation (R_r) and translucent area (A) against substrate lattice constant. A represents the proton diffusion coverage. (c) R_r shown with respect to in-plane Ni–O bond length ($d_{Ni–O,\ //}$). The inset shows a schematic of the corresponding $d_{Ni–O,\ //}$ and in-plane Ni–O–Ni open angle ($\theta_{Ni–O–Ni,\ //}$).

3.3.4. Density Functional Theory Calculation of Proton Diffusion

Here, I elucidate the proton dynamics in strain-regulated NNO films using results of DFT calculation. For the structural determination, I started with a pristine $Nd_4Ni_4O_{12}$ pseudotetragonal cell for a film grown on the substrate, and then, I allowed the ionic position, cell shape, and size to relax when strain was applied. When simulating proton diffusion, an interstitial proton was incorporated in the NNO lattice thus forming $NdNiO_3:H_{0.25}$ ($NNO:H_{0.25}$) composition. The composition of $NNO:H_{0.25}$ is thought to be suitable to represent the progressing proton diffusion, which induces resistance modulation before it reaches a plateau resistance, as shown in Figure 3.1a. The details of the DFT parameters and conditions are described in Supporting Information.

I then investigated the proton migration along the in-plane [110] direction using a climbing-image nudge elastic band (CI-NEB). The proton diffusion pathway and the corresponding energy profiles are shown in **Figures 3.4**a and 3.4b, respectively. Here, the proton H is initially bonded to oxygen O1 and then reorients via O1–H bond rotation into a position facing O2 (reaction coordinate 0–6). Next, H diffuses via interoctahedra hopping from O1 to O2 (6–12), breaking the O1–H bonding and starts to form the H–O2 bond. H bonded to neither O1 nor O2 provides migration barrier energy at reaction coordinate 9, and then subsequently reorients toward O3 (12–18). The migration barrier for this motion (0–18) decreases with increasing compressive strain, as shown in Figure 3.4b, which is attributed to the shortened O1–O2 hopping distance. In contrast, the tensile lattice shows a high migration barrier. Further motion will form an O3–H bond via intraoctahedra hopping, where H reorients once again (see: O3' in Figure 3.4a) and then finally hops to the neighboring O (18–24). The migration barrier for this motion (18–24) increases from compressive to tensile strain. The effective migration energy, i.e., the highest migration energy in H diffusion is plotted in Figure

3.4c. The results show that the migration barrier in a −2% to +2% strained lattice increases from 0.39 to 0.76 eV. H is estimated to have a lower migration barrier when diffusing along the in-plane direction in a compressive-strain lattice. This is because compressive strain reduces the in-plane lattice constants, resulting in a shorter hopping distance that eventually stabilizes the transition state during H migration.[38] Furthermore, I found that the shortened hopping distance is accommodated by the reduced $d_{\mathrm{Ni–O,}\,/\!/}$, which shows a similar trend to that in Figure 3.3c. The respective lattice constants and $d_{\mathrm{Ni–O,}\,/\!/}$ used in the simulation are shown in Table S3.4. Moreover, when tensile strain is applied, the in-plane lattice constants and the corresponding hopping distance increase. The migration barrier increases and, consequently, the in-plane long propagation of H is hindered in the tensile lattice. The findings of the migration barrier presented here support my experimental results. The compressive lattice exhibits a higher proton diffusion rate than that of the tensile lattices when protons diffuse along the in-plane direction. This further clarifies the experimental results in Figure 3.1b because the observed HNNO region essentially represents the in-plane diffusion.

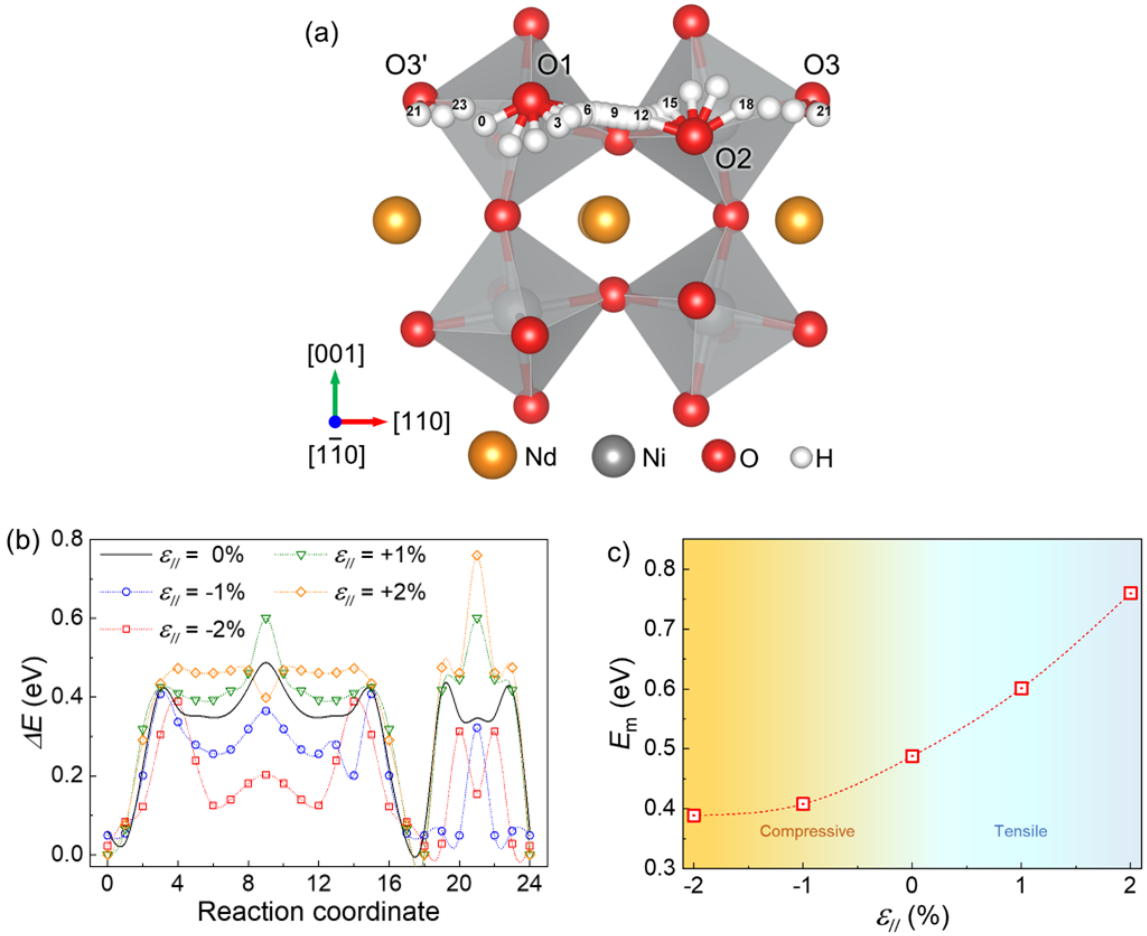

Figure 3.4. Strain-dependent proton diffusion obtained by DFT calculation. (a) Selected configuration along the in-plane [110] pathways and (b) associated energy profile for –2% compressive to +2% tensile strain, where the strain-free system is indicated by $\varepsilon_{//} = 0\%$. ΔE represents the relative energy from the initial state. Proton motion is depicted by the white spheres in (a), where its number represents the corresponding reaction coordinate. (c) Corresponding effective migration barrier E_m for proton motion series for each strained lattice.

Furthermore, on the basis of our DFT calculations, I estimated the proton diffusion rate from the motion probability. In the transition state theory, the transition rate of proton diffusion is given by[39]

$$k = v_0 e^{-\Delta G / k_B T}, \qquad (3.2)$$

where v_0 is the attempt frequency, ΔG is the migration free energy, k_B is the Boltzmann constant, and T is the absolute temperature.[40] From this estimation, I found that at room temperature, the transition rate the of proton along the in-plane direction k increases 48 times with –2% compressive strain compared with that in the case of the strain-free lattice. On the other hand, under +2% tensile strain, k is extremely suppressed and the rate is reduced by ~10^4 times. This reveals how the compressive strain is more effective than the tensile strain in distributing protons in the NNO lattice system. More importantly, this estimation has been successfully demonstrated by my experimental results, where I showed that the doping behavior and the corresponding resistance modulation can be finely tuned via the regulation of lattice strains.

3.4. Conclusion

I have demonstrated the fine tuning of proton doping in NNO thin films via the regulation of lattice strains. I show that the rational design of strain engineering is crucial for enabling diffusional doping in RNiO$_3$ perovskites whose properties are sensitive to gas-phase proton doping. Through my innovative experimental method, supported by computational analysis, I reveal the significance of strain-controlled proton diffusion in determining the resistance modulation during the hydrogenation-induced MIT. This strain-controlled proton diffusion will offer a promising strategy for designing multifunctional iontronics devices. Additionally, the results of the presented study will enrich the fundamental studies involving

both strongly correlated perovskite nickelates and ionic transport. Future improvement can be achieved by engineering thin film properties for sophisticated control of proton motion within a solid lattice to achieve high-performance device functions.

3.5. Reference

1) Jian, S.; Ha, S. D.; Zhou, Y.; Schoofs, F.; Ramanathan, S. A Correlated Nickelate Synaptic Transistor. *Nat. Commun.* **2013**, *4*, 2676.
2) Ha, S. D.; Shi, J.; Meroz, Y.; Mahadevan, L.; Ramanathan, S. Neuromimetic Circuits with Synaptic Devices Based on Strongly Correlated Electron Systems. *Phys. Rev. Appl.* **2014**, *2*, 064003.
3) Meijer, G. I. Who Wins the Nonvolatile Memory Race?. *Science* **2008**, *319*, 1625–1626.
4) Ha, S. D.; Aydogdu, G. H.; Ramanathan, S. Metal-Insulator Transition and Electrically Driven Memristive Characteristics of $SmNiO_3$ Thin Films. *Appl. Phys. Lett.* **2011**, *98*, 012105.
5) Li, Z.; Zhou, Y.; Qi, H.; Pan, Q.; Zhang, Z.; Shi, N. N.; Lu, M.; Stein, A.; Li, C. Y.; Ramanathan, S.; Yu, N. Correlated Perovskites as A New Platform for Super-Broadband-Tunable Photonics. *Adv. Mater.* **2016**, *28*, 9117–9125.
6) Chang, L.; Wang, L.; You, L.; Zhou, Y.; Fang, L.; Wang, S.; Wang, J. Band Gap Tuning of Nickelates for Photovoltaic Applications. *J. Phys. D: Appl. Phys.* **2016**, *49*, 44LT02.
7) Zhou, Y.; Guan, X.; Zhou, H.; Ramadoss, K.; Adam, S.; Liu, H.; Lee, S.; Shi, J.; Tsuchiya, M.; Fong, D. D.; Ramanathan, S. Strongly Correlated Perovskite Fuel Cells. *Nature* **2016**, *534*, 231–234.
8) Zhang, Y.; Knibbe, R.; Sunarso, J.; Zhong, Y.; Zhou, W.; Shao, Z.; Zhu, Z. Recent Progress on Advanced Materials for Solid-Oxide Fuel Cells Operating below 500 °C. *Adv. Mater.* **2017,** *29*, 1700132.

9) Catalan, G. Progress in Perovskite Nickelate Research. *Phase Transit.* **2008**, *81*, 729–749.

10) Medarde, M. L. Structural, Magnetic and Electronic Properties of Perovskites (R = Rare Earth). *J. Phys.: Condens. Matter* **1997**, *9*, 1679.

11) Zhang, H. T.; Zhang, Z.; Zhou, H.; Tanaka, H.; Fong, D. D.; Ramanathan, S. Beyond Electrostatic Modification: Design and Discovery of Functional Oxide Phases via Ionic-Electronic Doping. *Adv. Phys.: X* **2019**, *4*, 1523686.

12) Hanada, A.; Kinoshita, K.; Kishida, S. Resistive Switching by Migration of Hydrogen Ions. *Appl. Phys. Lett.* **2012**, *101*, 043507.

13) Oh, C.; Heo, S.; Jang, H. M.; Son, J. Correlated Memory Resistor in Epitaxial $NdNiO_3$ Heterostructures with Asymmetrical Proton Concentration. *Appl. Phys. Lett.* **2016,** *108*, 122106.

14) Oh, C.; Jo, M.; Son, J. All-Solid-State Synaptic Transistors with High-Temperature Stability using Proton Pump Gating of Strongly Correlated Materials. *ACS Appl. Mater. Interfaces* **2019**, *11*, 15733–15740.

15) Zhang, Z.; Schwanz, D.; Narayanan, B.; Kotiuga, M.; Dura, J. A.; Cherukara, M.; Zhou, H.; Freeland, J. W.; Li, J.; Sutarto, R.; He, F.; Wu, C.; Zhu, J.; Sun, Y.; Ramadoss, K.; Nonnenmann, S. S.; Yu, N.; Comin, R.; Rabe, K. M.; Sankaranarayanan, S. K. R. S.; Ramanathan, S. Perovskite Nickelates as Electric-Field Sensors in Salt Water. *Nature* **2018**, *553*, 68–72.

16) Chen, J.; Zhou, Y.; Middey, S.; Jiang, J.; Chen, N.; Chen, L.; Shi, X.; Döbeli, M.; Shi, J.; Chakhalian, J.; Ramanathan, S. Self-Limited Kinetics of Electron Doping in Correlated Oxides. *Appl. Phys. Lett.* **2015,** *107,* 031905.

17) Muraoka, K.; Kanki, T. Long-Range Propagation of Protons in Single-Crystal VO_2 Involving Structural Transformation to HVO_2. *Sci. Rep.* **2019,** *9*, 20093.

18) Yoon, H.; Choi, M.; Lim, T. W.; Kwon, H.; Ihm, K.; Kim, J. K.; Choi, S. Y.; Son, J. Reversible Phase Modulation and Hydrogen Storage in Multivalent VO_2 Epitaxial Thin Films. *Nat. Mater.* **2016**, *15*, 1113–1119.

19) Lu, N.; Zhang, P.; Zhang, Q.; Qiao, R.; He, Q.; Li, H. B.; Wang, Y.; Guo, J.; Zhang, D.; Duan, Z.; Li, Z.; Wang, M.; Yang, S.; Yan, M.; Arenholz, E.; Zhou, S.; Yang, W.; Gu, L.; Nan, C. W.; Wu, J.; Tokura, Y.; Yu, P. Electric-Field Control of Tri-State Phase Transformation with a Selective Dual-Ion Switch. *Nature* **2017,** *546*, 124–128.

20) Zuo, F.; Panda, P.; Kotiuga, M.; Li, J.; Kang, M.; Mazzoli, C.; Zhou, H.; Barbour, A.; Wilkins, S.; Narayanan, B.; Cherukara, M.; Zhang, Z.; Sankaranarayanan, S. K. R. S.; Comin, R.; Rabe, K. M.; Roy, K.; Ramanathan, S. Habituation Based Synaptic Plasticity and Organismic Learning in a Quantum Perovskite. *Nat. Commun.* **2017**, *8*, 240.

21) Shi, J.; Zhou, Y.; Ramanathan, S. Colossal Resistance Switching and Band Gap Modulation in a Perovskite Nickelate by Electron Doping. *Nat. Commun.* **2014,** *5*, 4860.

22) Catalano, S.; Gilbert, M.; Fowlie, J.; Íñiguez, J.; Triscone, J. M.; Kreisel, J. Rare-Earth Nickelates $RNiO_3$: Thin Films and Heterostructures. *Rep. Prog. Phys.* **2018**, *81,* 046501.

23) Alonso, J. A.; Martínez-Lope, M. J.; Casais, M. T.; Aranda, M. A. G.; Fernández-Díaz, M. T. Metal−Insulator Transitions, Structural and Microstructural Evolution of $RNiO_3$ (R= Sm, Eu, Gd, Dy, Ho, Y) Perovskites: Evidence for Room-Temperature Charge Disproportionation in Monoclinic $HoNiO_3$ and $YNiO_3$. *J. Am. Chem. Soc.* **1999**, *121*, 4754–4762.

24) Glazer, A. M. Simple Ways of Determining Perovskite Structures. *Acta Crystallogr. A* **1975**, *31*, 756–762.

25) Glazer, A. M. The Classification of Tilted Octahedra in Perovskites. *Acta Crystallogr. B* **1972**, *28*, 3384–3392.

26) Torrance, J. B.; Lacorre, P.; Nazzal, A. I.; Ansaldo, E. J.; Niedermayer, Ch. Systematic Study of Insulator-Metal Transitions in Perovskites $RNiO_3$ (R= Pr, Nd, Sm, Eu) due to Closing of Charge-Transfer Gap. *Phys. Rev. B* **1992**, *45*, 8209.

27) OriginLab, 18.1 Smoothing, https://www.originlab.com/doc/origin-help/smoothing, accessed: August, 2021.

28) Shirasawa, T.; Sekiguchi, K.; Iwasawa, Y.; Voegeli, W.; Takahashi, T.; Hattori, K.; Hattori, A. N.; Daimon, H.; Wakabayashi, Y. Interface Structure of an Epitaxial Iron Silicide on Si (111) Studied with X-Ray Diffraction. *e-J. Surf. Sci. Nanotechnol.* **2009,** *7*, 513–517.

29) Xiang, P. H.; Zhong, N.; Duan, C. G.; Tang, X. D.; Hu, Z. G.; Yang, P. X.; Zhu, Z. Q.; Chu, J. H. Strain Controlled Metal-Insulator Transition in Epitaxial $NdNiO_3$ Thin Films. *J. Appl. Phys.* **2013**, *114,* 243713.

30) Hauser, A. J.; Mikheev, E.; Moreno, N. E.; Hwang, J.; Zhang, J. Y.; Stemmer, S. Correlation between Stoichiometry, Strain, and Metal-Insulator Transitions of $NdNiO_3$ Films. *Appl. Phys. Lett.* **2015**, *106*, 092104.

31) Iglesias, L.; Sarantopoulos, A.; Magén, C.; Rivadulla, F. Oxygen Vacancies in Strained $SrTiO_3$ Thin Films: Formation Enthalpy and Manipulation. *Phys. Rev. B* **2017**, *95*, 165138.

32) Heo, S.; Oh, C.; Son, J.; Jang, H. M. Influence of Tensile-Strain-Induced Oxygen Deficiency on Metal-Insulator Transitions in $NdNiO_{3-\delta}$ Epitaxial Thin Films. *Sci. Rep.* **2017**, *7*, 4681.

33) He, F.; Wells, B. O.; Ban, Z.G.; Alpay, S. P.; Grenier, S.; Shapiro, S. M.; Si, W.; Clark, A.; Xi, X. X. Structural Phase Transition in Epitaxial Perovskite Films. *Phys. Rev. B* **2004**, *70*, 235405.

34) Chen, J.; Mao, W.; Gao, L.; Yan, F.; Yajima, T.; Chen, N.; Chen, Z.; Dong, H.; Ge, B.; Zhang, P.; Cao, X. Electron-Doping Mottronics in Strongly Correlated Perovskite. *Adv. Mater.* **2020**, *32*, 1905060.

35) Hwang, J.; Zhang, J. Y.; Son, J.; Stemmer, S. Nanoscale Quantification of Octahedral Tilts in Perovskite Films. *Appl. Phys. Lett.* **2012**, *100*, 191909.

36) May, S. J.; Kim, J.-W.; Rondinelli, J. M.; Karapetrova, E.; Spaldin, N. A.; Bhattacharya, A.; Ryan, P. J. Quantifying Octahedral Rotations in Strained Perovskite Oxide Films. *Phys. Rev. B* **2010**, *82*, 014110.

37) Garcia-Munoz, J. L.; Rodriguez-Carvajal, J.; Lacorre, P.; Torrance, J. B. Neutron-Diffraction Study of $RNiO_3$ (R= La, Pr, Nd, Sm): Electronically Induced Structural Changes across The Metal-Insulator Transition. *Phys. Rev. B* **1992,** *46*, 4414.

38) Yoo, P.; Liao, P. First Principles Study on Hydrogen Doping Induced Metal-to-Insulator Transition in Rare Earth Nickelates $RNiO_3$ (R = Pr, Nd, Sm, Eu, Gd, Tb, Dy, Yb). *Chem. Chem. Phys.* **2020,** *22,* 6888–6895.

39) Eyring, H. The Activated Complex in Chemical Reactions. *J. Chem. Phys.* **1935**, *3*, 107.

40) Due to the high computational process, ΔG herein is approximated as the calculated barrier bottleneck without the evaluation of the vibrational frequencies in the saddle configuration.

Supporting information for CHAPTER 3

Tunable Proton Diffusion in $NdNiO_3$ Thin Films under Regulated Lattice Strains

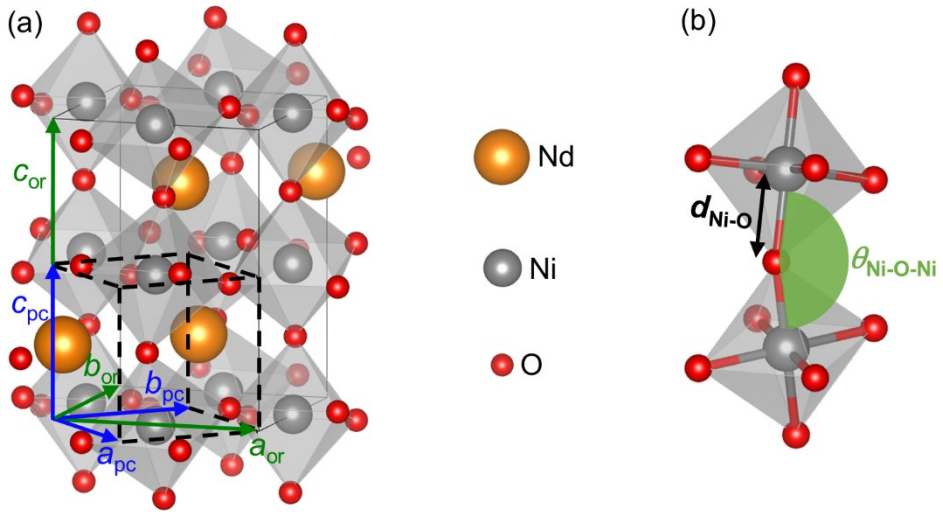

Figure S3.1. (a) Relationship between the orthorhombic (a_{or}) and pseudocubic (a_{pc}) lattice constants in the perovskite NNO structure. Regardless of the specific structure adopted, it is convenient to describe the actual NNO material with respect to the pseudocubic unit cell. For example, when assessing structural similarity among different compounds, it is practical to compare their a_{pc}. (b) Schematic of the three-dimensional oxygen octahedra network with Ni–O bond length ($d_{Ni–O}$) and Ni–O–Ni open angle ($\theta_{Ni–O–Ni}$).

The crystalline structure of NNO is shown in Figure S3.1. The lattice constants of NNO, KTO, STO, LSAT, and LAO in bulk are noted in Table S3.1. Bulk NNO possesses an orthorhombic perovskite structure with ordered NiO_6 octahedral networks and Nd cations in the cavities. The ideal NNO perovskite structure is cubic with the space group Pm-3m, where the lattice constant a and the ionic radii r_i should satisfy the relation $a = \sqrt{2}(r_{Nd} + r_O) = 2(r_{Ni} + r_O)$. In reality, this relation does not exist in nature for bulk NNO and structural distortions occur to compensate for the ionic packing. The tendency to deviate from the cubic ideal can be estimated by the Goldschmidt tolerance factor t, defined as $t = 2(r_{Nd} + r_O) / \sqrt{2}(r_{Ni} + r_O)$.[1,2] The combination of tilts, distortions, and rotations of the corner-sharing NiO_6 octahedral networks forming the Ni–O–Ni open angle ($\theta_{Ni–O–Ni}$) and Ni–O bond length ($d_{Ni–O}$) leads to an orthorhombic structure from the cubic ideal.[2]

Table S3.1. Lattice constants of bulk NNO, KTO, STO, LSAT, and LAO[3–6]

Crystal	Structure	a_{bulk} (Å)	b_{bulk} (Å)	c_{bulk} (Å)
$NdNiO_3$ (NNO)	Orthorhombic	5.389	5.381	7.610
	Pseudocubic	3.807	3.807	3.807
$KTaO_3$ (KTO)	Cubic	3.989	3.989	3.989
$SrTiO_3$ (STO)	Cubic	3.905	3.905	3.905
$(La,Sr)(Al,Ta)O_3$ (LSAT)	Cubic	3.868	3.868	3.868
$LaAlO_3$ (LAO)	Pseudocubic	3.789	3.789	3.789

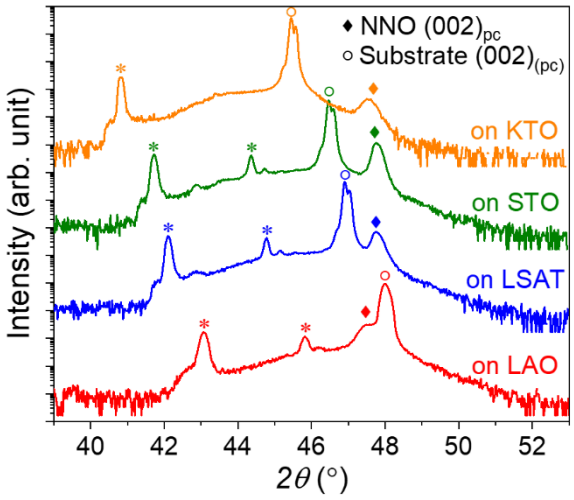

Figure S3.2. 2θ-ω XRD curves (Cu Kα) of the pristine NNO films grown on KTO, STO, LSAT, and LAO substrates. The peaks marked by an asterisk (*) originated from the substrates.

Figure S3.2 shows 2θ-ω XRD curves for the pristine NNO films. The $(002)_{pc}$ peaks of NNO films can be seen at 2θ ~47.46–47.76°. The peaks at 2θ ~45.43°, 46.48°, 47.00°, and 48.03° are assigned to $(002)_{(pc)}$ of KTO, STO, LSAT, and LAO substrates, respectively. The peak positions are in good agreement with those in previous diffraction studies.[7,8] It is seen

from the curves that, regardless of the substrates, *c*-axis-oriented NNO films were grown without any detectable impurity phase.

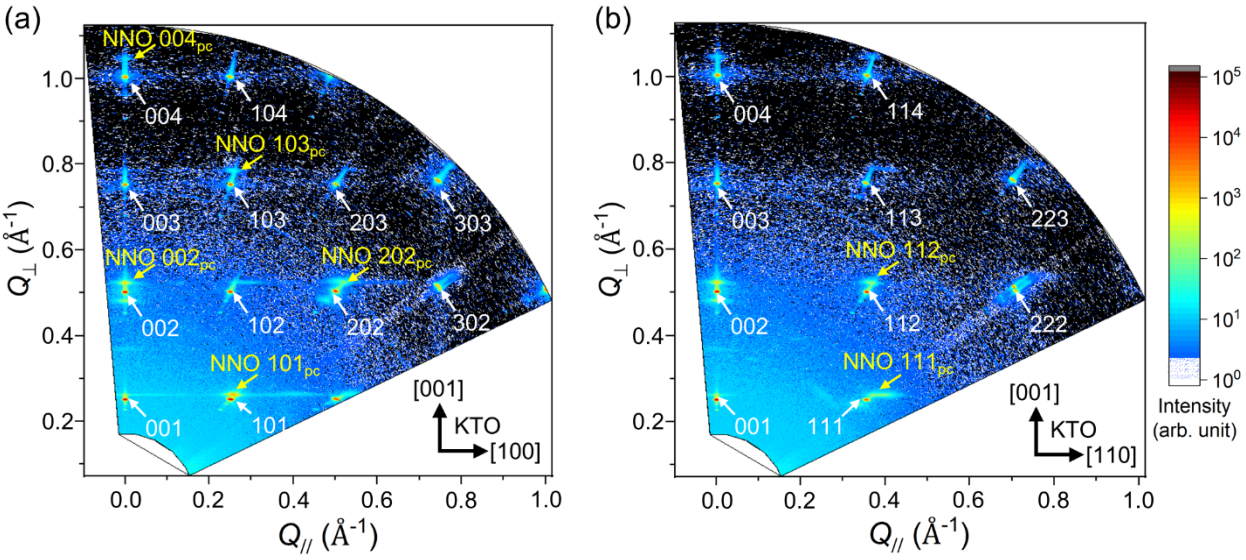

Figure S3.3. Wide RSMs of pristine NNO on KTO with the in-plane directions of (a) [100] and (b) [110]. Some intense NNO film peaks and substrate peaks are denoted with and without NNO labels, respectively. NNO peaks are located close to the corresponding substrate peaks in both in-plane directions.

In addition, all NNO films were also grown epitaxially along the in-plane directions, that is, NNO $[100]_{pc}$ was parallel to the substrate $[100]_{(pc)}$ as confirmed by wide RSMs. For example, Figure S3.3 indicates the RSM cross sections with different in-plane orientations, a) KTO[100] (in-plane) – [001] (out-of-plane) and b) KTO[110] (in-plane) – [001] (out-of-plane), for pristine NNO films on KTO(001) substrate. NNO $h0\ell_{pc}$ and $hh\ell_{pc}$ peaks are synchronized to $h0\ell_{(pc)}$ and $hh\ell_{(pc)}$ of the substrates as shown in Figures S3.3a and S3.3b, respectively. Since the substrate (001) surfaces and NNO(001) are 4-fold symmetric owing to (pseudo) cubic structures ensures an equivalent strains in $[100]_{(pc)}$ and $[010]_{(pc)}$ directions, the analysis of NNO spot with $[100]_{(pc)}$, for instance NNO 103_{pc}, is enough for the estimation of the in-plane strain

$\varepsilon_{//}$, in addition to the out-of-plane strain $\varepsilon_{\perp}$ in $[001]_{(pc)}$ direction. All RSM images were created with OriginLab using input from smoothed dataset generated by 3D Explore (Rigaku).

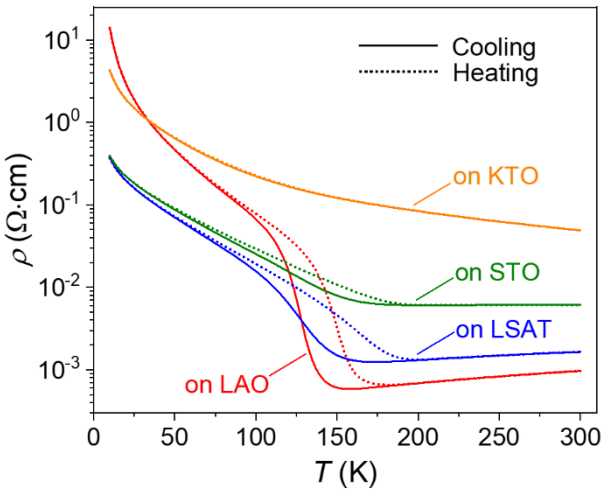

Figure S3.4. Temperature-dependent resistivity (ρ–T) curves of pristine NNO films deposited on KTO, STO, LSAT, and LAO substrates.

NNO films grown on LAO, LSAT, and STO show a sharp metal–insulator transition (MIT) during both heating and cooling cycles, as shown in Figure S3.4. The transition temperatures are 180–200 K and show similar characteristic as those described in other reports of bulk and NNO films.[9–12] On the other hand, no MIT is observed on NNO/KTO owing to the excessively large lattice mismatch at the substrate–film interface. This contributes to stabilizing the insulating state of the film at a relatively high temperature, replacing the metallic state completely. Similar transport properties have been observed in NNO films deposited on $DyScO_3$ and MgO.[10,11] In addition, resistivity in the high-temperature region increases in the order of NNO/LAO to NNO/LSAT, NNO/STO, and NNO/KTO. This can be attributed to the different levels of the lattice strain introduced in NNO films.[8,13]

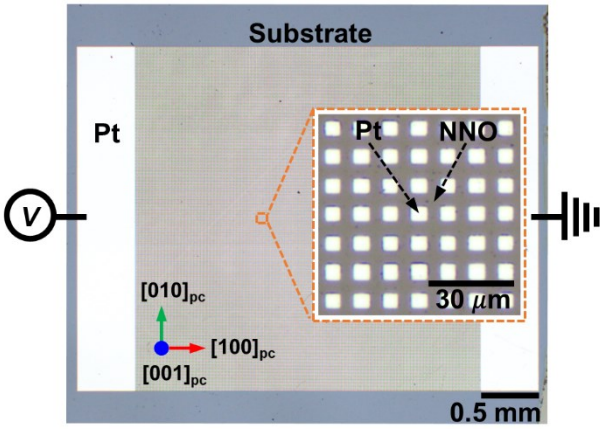

Figure S3.5. Optical microscopy image of the Pt catalyst pads deposited on the surface of NNO film. The configuration was used to examine the proton diffusion and the time-dependent resistance modulation during the catalytic proton doping process.

Figure S3.5 shows a typical optical microscopy image of ~15 nm-thick Pt catalyst deposited onto NNO film with a thicknesss of ~80 nm. The Pt catalyst pattern consists of a 5 × 5 μm^2 mesh of squares with 5 μm spacings between them. Hydrogen dissociation caused by the Pt-catalytic effect proceeds at the triple-phase boundary of Pt–NNO–H_2.

Figure S3.6a shows the reversibility of the hydrogen adsorption and desorption processes. Annealing in air at 473 K for 40 min can partially recover the resistance of NNO/STO thin film. A longer annealing duration with higher temperature and using ozone (O_3) gas has been reported to further reduce the resistance to the pristine condition. Figure S3.6b shows that the proton-induced resistance modulation was maintained for 6 days under atmospheric conditions.

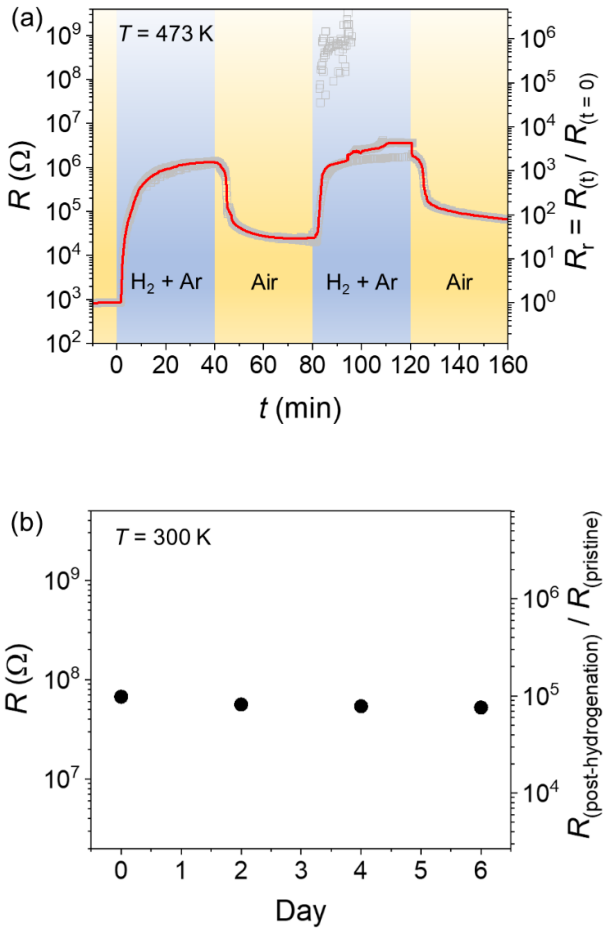

Figure S3.6. Reversibility and stability of hydrogenation for NNO/STO. (a) Reversibility characteristic under 100 mL of 5% H_2–95% Ar in air at 473 K. The raw data represented by the gray symbols were smoothed into the line graphs using the 50% percentile filter in OriginLab. (b) Retention test measured at 300 K in air. After hydrogenation at 473 K for 40 min, the samples were stored in air at room temperature under atmospheric conditions for 6 days. Values shown in the graph represent average smoothed values of retention test for duration of 30 min.

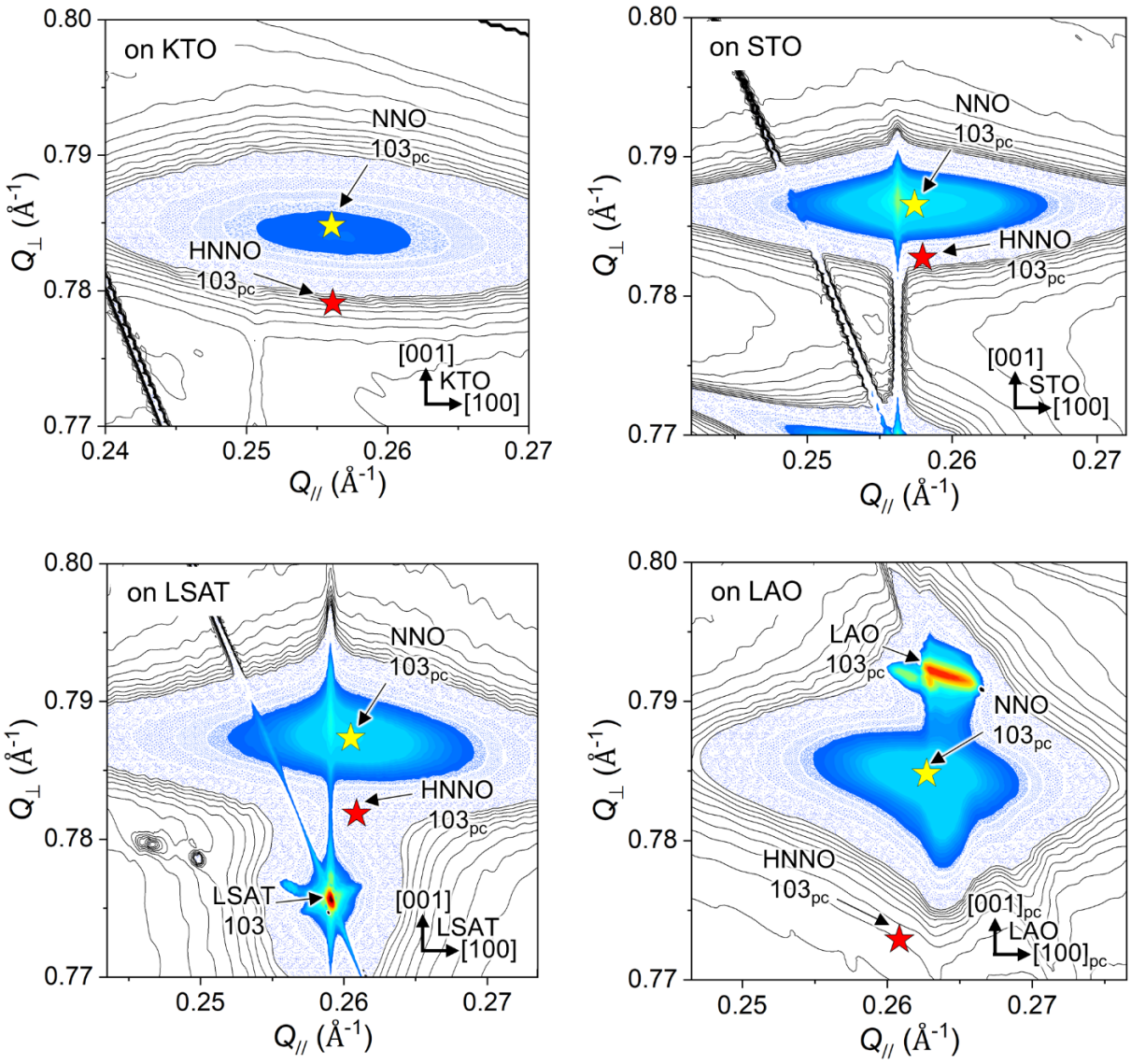

Figure S3.7. Magnified precise RSM images of pristine NNO samples from Figure 3.2a.

Magnified precise RSMs of the pristine NNO samples in Figure 3.2a are shown in Figure S3.7. The peak shapes of (H)NNO 103_{pc} were fitted with Gaussian eliminating the streaks of the surface rods and artefacts. The peak positions (Table S3.2) by the Gaussion fitting were estimated within 0.0001 $Å^{-1}$ error. The yellow stars in Figure S3.7 mark 103_{pc} peaks of the pristine NNO films. Red stars are added to indicate the shift of the corresponding 103_{pc} peaks after hydrogenation (HNNO). The hydrogenation-induced peak shift occurs preferentially along the out-of-plane direction ($Q_{\perp}$) over the in-plane direction ($Q_{//}$). The

volume increase in the pristine samples from the bulk NNO (55.18 $Å^3$) might be caused by oxygen vacancy. This effect to the electrical characteristics and hydrogenation process is considerably insignificant as shown by the good MIT characteristics in Figure S3.4 and monotonical resistance increase during hydrogenation in Figure 3.1(a), respectively. [8–13]

Table S3.2. Peak positions of the pristine NNO and hydrogenated NNO films on KTO, STO, LSAT, and LAO substrates in the pricise RSMs in Figures 3.2 and S3.6. a_{pc}* and $3c_{pc}$* represent $Q_{//}$ and $Q_{\perp}$ positions, respectively. The inverse of a_{pc}* and c_{pc}* are lattice constants a_{pc} and c_{pc}, respectively.

Substrate	Pristine NNO		Hydrogenated NNO	
	a_{pc}* (Å^{-1})	$3c_{pc}$* (Å^{-1})	a_{pc}* (Å^{-1})	$3c_{pc}$* (Å^{-1})
KTO	0.256	0.784	0.256	0.779
STO	0.257	0.786	0.258	0.782
LSAT	0.260	0.787	0.260	0.781
LAO	0.262	0.784	0.260	0.772

Table S3.3. In-plane (a_{pc}) and out-of-plane (c_{pc}) lattice constants of pristine and hydrogenated NNO films on KTO, STO, LSAT, and LAO substrates.

Substrate	Pristine NNO		Hydrogenated NNO	
	a_{pc} (Å)	c_{pc} (Å)	a_{pc} (Å)	c_{pc} (Å)
KTO	3.905	3.822	3.903	3.850
STO	3.884	3.813	3.875	3.832
LSAT	3.838	3.809	3.832	3.836
LAO	3.805	3.822	3.833	3.881

In general, the width of a peak shape is caused by two effects; one is the crystalline domain size and the other is the inhomogenous strain distribution.[14] When the inhomogenious strain is dominant, the peak width increases with far from the reciprocal space origin. I confirmed that widths of different peaks were similar. For instance, the in-plane and out-of-plane full width half maximum (FWHM) values of NNO 103_{pc} on LAO in Figure S3.7 were ≈0.0085 $Å^{-1}$ and ≈0.0030 $Å^{-1}$, respectively, while those of NNO 002_{pc} on LAO in Figure S3.8 were ≈0.0065 $Å^{-1}$ and ≈0.0017 $Å^{-1}$, respectively. This implies that the total epitaxial NNO film had a homogenous strain distribution and the peak widths were originated mainly from the crystalline domain size (e.g., ≈117–154 Å in in-plane and ≈331–606 Å in out-of-plane for NNO on LAO).

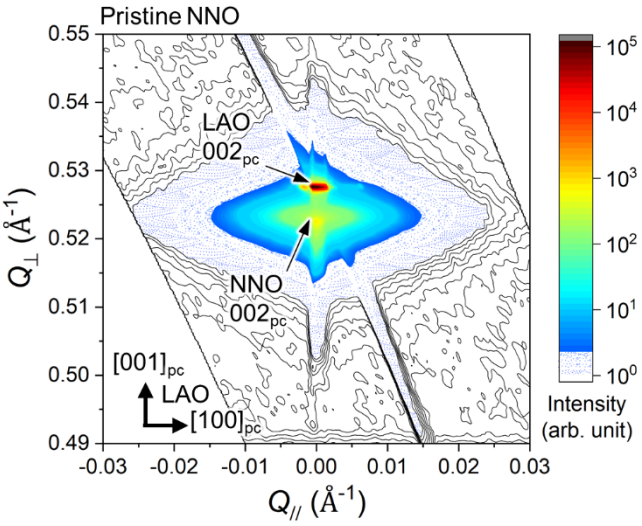

Figure S3.8. Precise RSM image of pristine NNO 002_{pc} peak on LAO substrate.

Density Functional Theory (DFT): The calculations were performed using the plane-wave Quantum Espresso (QE) code[15] and visualized using VESTA.[16] The interactions between ions and electrons were described by the projector augmented-wave (PAW) method.[17] The exchange-correlation effects were described by the generalized gradient approximation (GGA) using the Perdew–Burke–Ernzerhof functional for solids (PBEsol).[18] The strong correlation

effects of Ni 3*d* electrons were treated by the self-consistent Hubbard *U* correction, formulated by Timrov *et al*.,[19] which is implemented in the QE code. Through this method, the effective *U* value of 8.98 eV on the Ni site was obtained.

The simulated structures were constructed on the basis of a 20-atom (√2×√2×2) pseudotetragonal cell of thin films grown on the substrates. The imposed strain is expressed as the change in lattice constant *a* with respect to its original lattice value a_o, defined as $\varepsilon_{//} = ((a - a_o) / a_o)\ 100\%$, where $\varepsilon_{//} = 0\%$ denotes the strain-free system. The lattice constant along the *c*-axis is relaxed so that the energy of the system under strain is minimized. The calculated lattice constants (*a*, *b*, *c*) and corresponding in-plane Ni–O bond length ($d_{Ni–O, //}$) under various strains are listed in Table S3.4. For each strain value, I used the climbing-image nudge elastic band (CI-NEB) method[20] to estimate the proton migration energy and determine its minimum energy pathways (MEP) along the in-plane direction. The detailed analysis of the strain-dependent proton diffusion will be published elsewhere.

Table S3.4. Lattice constants (*a*, *b*, *c*) and in-plane Ni–O bond length ($d_{Ni–O, //}$) as a function of biaxial strain ($\varepsilon_{//}$)

$\varepsilon_{//}$ (%)	*a* (Å)	*b* (Å)	*c* (Å)	$d_{Ni–O, //}$ (Å)
−2	5.32	5.32	7.75	1.97
−1	5.38	5.38	7.67	2.00
0	5.43	5.43	7.68	2.02
+1	5.48	5.48	7.55	2.03
+2	5.54	5.54	7.49	2.05

Reference

1) Bhalla, A. S.; Guo, R.; Roy, R. The Perovskite Structure—a Review of Its Role in Ceramic Science and Technology. *Mater. Res. Innov.* **2000**, *4*, 3–26.

2) Travis, W.; Glover, E. N. K.; Bronstein, H.; Scanlon, D. O.; Palgrave, R. G. On the Application of the Tolerance Factor to Inorganic and Hybrid Halide Perovskites: a Revised System. *Chem. Sci.* **2016**, *7*, 4548–4556.

3) Hepting, M. *Ordering Phenomena in Rare-Earth Nickelate Heterostructures*; Springer, 2017, 145.

4) Tyunina, M.; Narkilahti, J.; Levoska, J.; Chvostova, D.; Dejneka, A.; Trepakov, V.; Zelezny, V. Ultrathin $SrTiO_3$ Films: Epitaxy and Optical Properties. *J. Phys.: Condens. Matter* **2009**, *21*, 232203.

5) Liu, J.; Kargarian, M.; Kareev, M.; Gray, B.; Ryan, P.J.; Cruz, A.; Tahir, N.; Chuang, Y.D.; Guo, J.; Rondinelli, J.M.; Freeland, J.W. Heterointerface Engineered Electronic and Magnetic Phases of $NdNiO_3$ Thin Films. *Nat. Commun.* **2013**, *4*, 2714.

6) Kristalltechnologie, Data-Sheets. http://www.crystec.de/datasheets-e.html (accessed: 19 August 2021).

7) Kumar, Y.; Choudhary, R. J.; Kumar, R. Strain Controlled Systematic Variation of Metal-Insulator Transition in Epitaxial $NdNiO_3$ Thin Films. *J. Appl. Phys.* **2012,** *112*, 073718.

8) Scherwitzl, R.; Zubko, P.; Lezama, I. G.; Ono, S.; Morpurgo, A. F.; Catalan, G.; Triscone, J. M. Electric-Field Control of the Metal-Insulator Transition in Ultrathin $NdNiO_3$ Films. *Adv. Mater.* **2010,** *22,* 5517–5520.

9) Canfield, P. C.; Thompson, J. D.; Cheong, S. -W.; Rupp, L. W. Extraordinary Pressure Dependence of the Metal-to-Insulator Transition in the Charge-Transfer Compounds $NdNiO_3$ and $PrNiO_3$. *Phys. Rev. B* **1993**, *47,* 12357.

10) Catalan, G.; Bowman, R. M.; Gregg, J. M. Metal-Insulator Transitions in $NdNiO_3$ Thin Films. *Phys. Rev. B* **2000,** *62*, 7892.

11) Guo, Q.; Farokhippor, S.; Magen, C.; Rivadulla, F.; Noheda, B. Tunable Resistivity Exponents in the Metallic Phase of Epitaxial Nickelates. *Nat. Commun.* **2020**, *11*, 2949.

12) Yamanaka, T.; Hattori, A. N.; Pamasi, L. N.; Takemoto, S.; Hattori, K.; Daimon, H.; Sato, K.; Tanaka, H. Effects of Off-Stoichiometry in the Epitaxial $NdNiO_3$ Film on the Suppression of Its Metal-Insulator-Transition Properties. *ACS Appl. Electron. Mater.* **2019**, *1*, 2678–2683.

13) Kumar, Y.; Choudhary, R. J.; Sharma, S. K.; Knobel, M.; Kumar, R. Strain Dependent Stabilization of Metallic Paramagnetic State in Epitaxial $NdNiO_3$ Thin Films. *Appl. Phys. Lett.* **2012**, *101*, 132101.

14) Takemoto, S.; Hattori, K.; Someta, M.; Hattori, A. N.; Tanaka, H.; Kurushima, K.; Otsuka, Y.; Daimon, H. Shape-Fitting Analyses of Two-Dimensional X-ray Diffraction Spots for Strain-Distribution Evaluation in a β-$FeSi_2$ Nanofilm. *J. Appl. Cryst.* **2019**, *52*, 732–744.

15) Giannozzi, P.; Andreussi, O.; Brumme, T.; Bunau, O.; Nardelli, M.B.; Calandra, M.; Car, R.; Cavazzoni, C.; Ceresoli, D.; Cococcioni, M.; Colonna, N. Advanced Capabilities for Materials Modelling with Quantum ESPRESSO. *J. Phys.: Condens. Matter* **2017,** *29*, 465901.

16) Momma, K.; Izumi, F. VESTA 3 for Three-Dimensional Visualization of Crystal, Volumetric and Morphology Data. *J. Appl. Crystallogr.* **2011**, *44*, 1272–1276.

17) Blöchl, P. E. Projector Augmented-Wave Method. *Phys. Rev. B* **1994**, *50*, 17953.

18) Perdew, J. P.; Ruzsinszky, A.; Csonka, G. I.; Vydrov, O. A.; Scuseria, G. E.; Constantin, L. A.; Zhou, X.; Burke, K. Restoring the Density-Gradient Expansion for Exchange in Solids and Surfaces. *Phys. Rev. Lett.* **2008**, *100*, 136406.

19) Timrov, I.; Marzari, N.; Cococcioni, M. Hubbard Parameters from Density-Functional Perturbation Theory. *Phys. Rev. B* **2018,** *98,* 085127.

20) Henkelman, G.; Uberuaga, B. P.; Jonsson, H. A Climbing Image Nudged Elastic Band Method for Finding Saddle Points and Minimum Energy Paths. *J. Chem. Phys.* **2000**, *113*, 9901.

CHAPTER 4

Electric Field Control for Catalytic Proton Doping

ABSTRACT

The electric-field-assisted hydrogenation and corresponding resistance modulation of $NdNiO_3$ (NNO) thin-film resistors were systematically studied as a function of temperature and dc electric bias. Catalytic Pt electrodes serve as triple phase boundaries for hydrogen incorporation into a perovskite lattice. The combination of an electric field and gas-phase annealing is shown to enable the elegant control of the diffusional doping of complex oxides.

4.1. Background

Perovskite rare-earth nickelates (RNiO$_3$, R = rare-earth element) have attracted considerable interest owing to their rich electronic phases originating from the strongly correlated electron effects.[1] Among these features, the sharp metal–insulator transition (MIT) followed by large resistance modulation in these materials has been intensively investigated to realize novel electronic devices exploiting the Mott transition.[2-5]

In recent years, resistance modulation in this RNiO$_3$ family has been successfully demonstrated through several methods, such as those based on solid gate dielectrics[6] and electric double layers with ionic liquids or gels.[7,8] However, these methods have a carrier concentration manipulation strategy based on the traditional static charge gating mechanism, which can restrict the extent of carrier density modulation, leading to a limited change in resistance. On the other hand, while areal carrier density modulation is possible with traditional static charge gating methods, ion doping can reconstruct electronic band structures in entirety by introducing an extremely high carrier density, resulting in large resistance modulation in a non-thermal manner. In addition to the large resistance modulation, ion doping also has potential to reversibly change the structural and electronic properties of correlated materials via an electric field by manipulating the ion diffusion process into or out of a material. Recently,

a reversible resistance modulation of approximately 8 orders of magnitude in $SmNiO_3$ (SNO) has been successfully demonstrated by proton doping via a chemical route (hydrogenation), where protons are dissociated from hydrogen molecules by utilizing the Pt catalytic effect and then doped into the thin film.[9] In the hydrogenation process, while the proton dopant is diffused by hopping and the concentration gradient effect, an electric field is also expected to be a driving force to diffuse the positively charged protons in the thin film. However, the dynamics of electric-field-assisted hydrogenation has not been studied to date. Such studies could be valuable for memory, chromic, or other iontronic devices utilizing proton motion in solids[10-12] as well as for theoretical studies of proton migration pathways and kinetics.[13,14]

4.2. Objective

In this work, I prepared $NdNiO_3$ (NNO) thin-film resistors with Pt-Au/Ti heteroelectrodes and directly observed the effect of electric-field-assisted hydrogenation. Bulk NNO (a = 0.3807 nm, pseudo-cubic) is a d-band electron-correlated perovskite-structured $RNiO_3$ with ordered NiO_6 octahedral networks and R cations arranged in the cavities. The three-dimensional corner-sharing network of BO_6 octahedra constitutes the fundamental structure and functional unit, and this material shows a resistance modulation of 1–2 orders of magnitude through its thermal MIT at around 200 K.[15] Compared to the previously reported SNO (MIT temperature at ~400 K),[9] the metallic behavior of "pristine" NNO at and above room temperature enables me to focus primarily on the chemically driven MIT via hydrogenation in this study. In addition, because hydrogen dissociates on the Pt electrode but not on the Au/Ti electrode, by using this two-terminal heteroelectrodes resistor configuration, I was able to investigate the effect of electric-field-assisted proton diffusion in our NNO film during hydrogenation.

4.3. Results and Discussion

An approximately 110 nm-thick NNO film was deposited on a commercial $SrTiO_3$ (100) substrate (STO, a = 0.3905 nm, cubic) by PLD. The as-deposited NNO film was 2θ-ω-scanned (out-of-plane) using an X-ray diffraction (XRD) system to investigate its crystal structure. The film was patterned by a photolithography technique. Then, RF sputtering was implemented to deposit the Pt and Au/Ti electrodes on top of the NNO film. Finally, the sample was dry-etched using an Ar ion milling system to form a two-terminal resistor configuration. The instruments detail and settings are described in Chapter 2.

Temperature-dependent resistivity measurement was performed using a physical property measurement system during heating and cooling cycles in the range of 10–250 K. The hydrogenation was performed in H_2 gas flow (5% H_2/95% Ar) under atmospheric conditions. The proton migration length along the NNO film channel was determined using an optical microscope since as doping progresses, because of the large gap that opens up, the hydrogen-doped region becomes optically transparent. The minimum resolution limit of the length-scale measurement was 0.58 μm.

4.3.1. Intrinsic Properties of NNO Thin Films

Figure 4.1a shows the 2θ-ω XRD pattern (Cu Kα) of the as-deposited NNO film grown on an STO (100) substrate. The peaks at $2\theta \sim 23.34^{\circ}$ and 47.76° are assigned to pseudo-cubic NNO 001 and 002 reflections, respectively (PDF no. 01-079-2459). It is seen from the pattern that a highly c-axis-oriented NNO film is grown without any detectable impurity phase. The intrinsic MIT characteristic of the NNO film was examined through temperature-dependent in-plane electrical resistivity (ρ versus T), as shown in Figure 4.1b. The film showed a sharp MIT during both cooling and heating cycles. The transition temperature can be seen clearly at 200–

210 K in the plot of dρ/dT% versus T in the inset of Figure 4.1b, which is indicated by the change in the sign of the temperature coefficient of resistivity from dρ/dT < 0 (insulating state) to dρ/dT > 0 (metallic state) or vice versa. Similar MIT characteristics have been observed in other reports of bulk NNO[15,16] as well as of NNO films deposited on STO substrates.[17,18] The XRD and ρ–T results prove the high quality of the as-deposited NNO film.

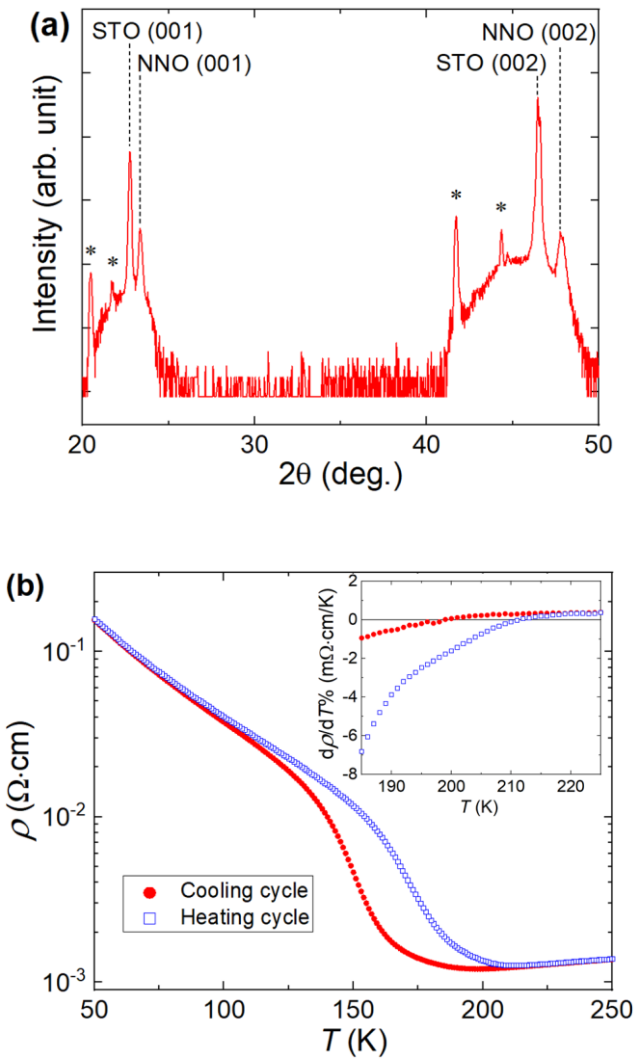

Figure 4.1 (a) XRD pattern of NNO film deposited on STO substrate. The peaks marked by * originated from the substrate. (b) ρ–T curve of NNO film. The inset shows the first derivative of resistivity with respect to temperature (dρ/dT% versus T).

4.3.2. Gas-Phase Hydrogenation on NNO Thin Films

The NNO film was then formed into a two-terminal resistor with Pt-Au/Ti heteroelectrodes, as shown in **Figure 4.2**a. In this resistor configuration, protons are incorporated into the NNO lattice via hydrogenation at the triple phase boundary of the Pt electrode (Pt-NNO-H_2), owing to the catalytic effect of Pt, which dissociates hydrogen molecules.[9] By performing the electric-field-assisted hydrogenation on a set of samples from the same NNO film, I was able to observe the effect of electric field and temperature during hydrogenation on NNO film with similar defect condition. Figure 4.2b shows the resistor after being exposed to electric-field-assisted hydrogenation at 473 K with an applied positive bias of +10 V. This figure shows the color change of the NNO channel where the region near the Pt electrode became optically transparent, while the region further away from the Pt electrode (towards the Au/Ti electrode) retained its dark color. The transparency corresponds to the hydrogenation of the NNO film. The length of the transparent region, i.e., the proton migration length (ℓ_p, defined as the total transparent NNO area divided by the NNO channel width) was measured to be 5.26 ± 0.13 μm (Figure 4.2b, right panel).

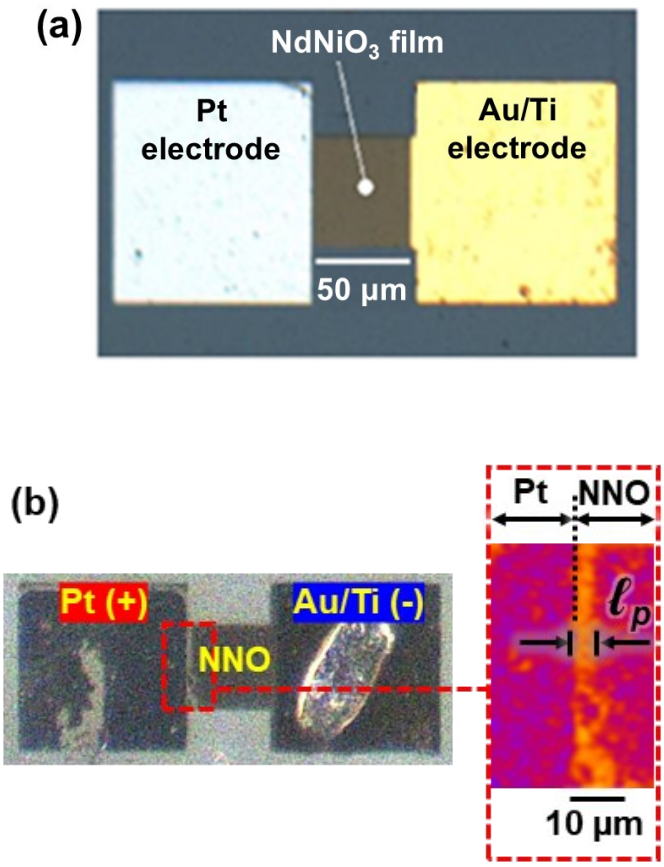

Figure 4.2 (a) Optical microscopy image of two-terminal NNO film resistor with Pt-Au/Ti heteroelectrodes. (b) NNO film resistor after electric-field-assisted hydrogenation at T = 473 K with V = +10 V for 1800 s. The magnified image (right panel) shows the proton migration length (ℓ_p = the total transparent NNO area / the NNO channel width). The color conversion was done by applying a selected color lookup tables in ImageJ to the grayscale image to produce false-color scale.

4.3.3. Effect of Electric Field Polarity during Hydrogenation of NNO Thin Films

To examine the effects of the polarity of the electric field and the temperature on hydrogenation, a series of samples were hydrogenated with positive and negative bias voltages (V = ±10 V) on the Pt electrode at various temperatures. **Figure 4.3**a presents the polarity-dependent ℓ_p at different fixed temperatures in the range of 300–473 K after 1800 s of

hydrogenation. It was confirmed that the hydrogenated region on the NNO film channel with V = +10 V was wider than that with V = -10 V at all temperatures. ℓ_p increased with the hydrogenation temperature, ranging from 0.84 ± 0.03 to 5.26 ± 0.13 μm for V = +10 V with T increasing from 300 K to 473 K. Although no transparent region was observed on the NNO channel near the Pt electrode at V = -10 V and 300–423 K, ℓ_p was 0.58 ± 0.05 μm for V = -10 V at T = 473 K. These data clearly indicate the effects of temperature and polarity on hydrogenation. Furthermore, compared with ℓ_p under zero field (V = 0 V), that at V = +10 V was large at each temperature. In contrast, ℓ_p was smaller for V = -10 V than that for V = 0 V at all temperatures except 300 K. This strongly indicates that the electric field can effectively control the hydrogenation with assistance from the thermal effect, especially lateral proton diffusion in the NNO channel, i.e., hydrogenation from the Pt edge towards the Au/Ti electrode along the electric field gradient. This control is demonstrated in Figure 4.3b, showing the thermally assisted electric field control of ℓ_p at 473 K, where lateral proton diffusion indicated by orange color area is accelerated or hindered by a positive or negative bias voltage, respectively. This implies that while a positive bias voltage and a high temperature can increase ℓ_p, the lateral proton diffusion at the Pt electrode edge is suppressed under a negatively biased voltage and a low temperature.

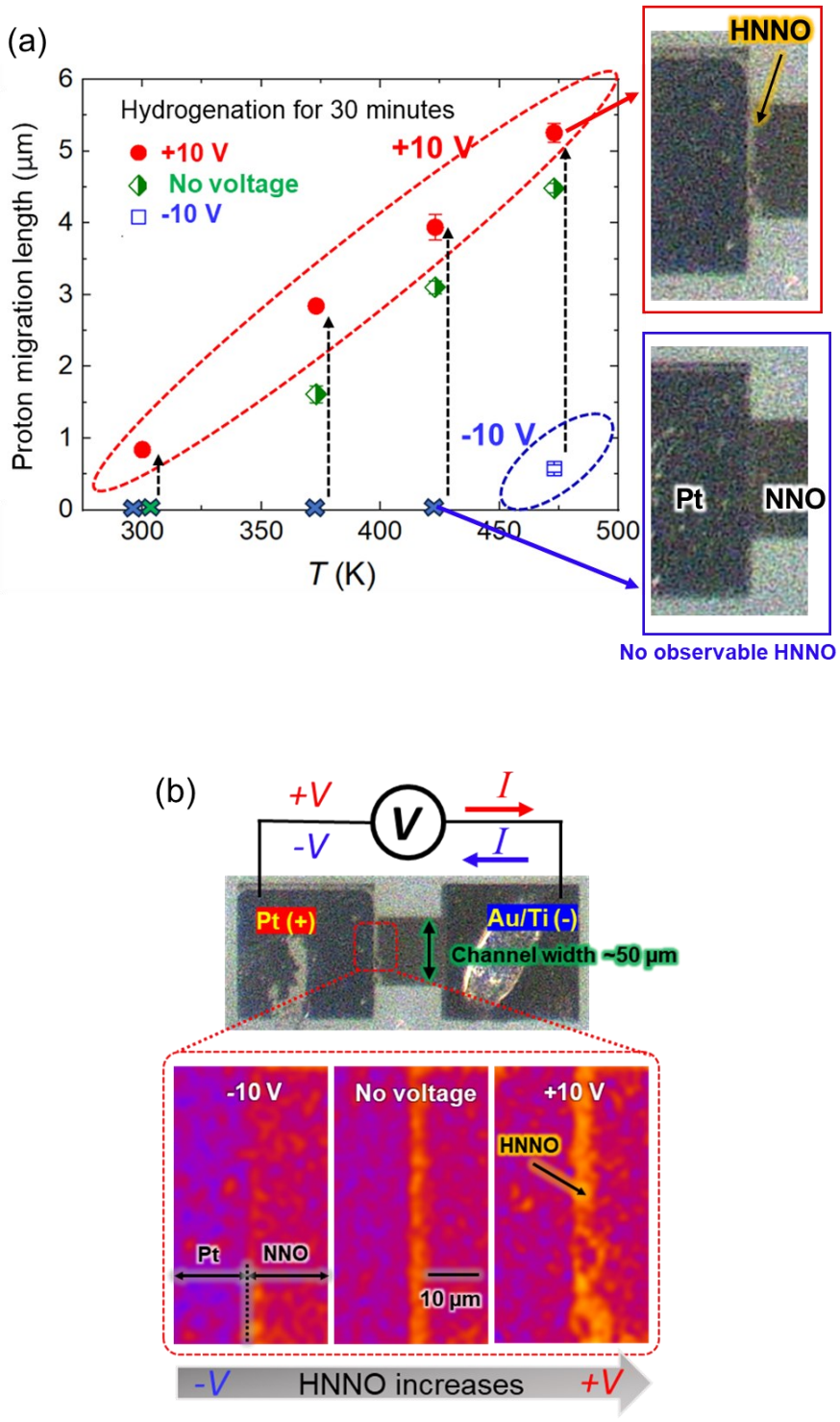

Figure 4.3 Electric-field-assisted hydrogenation. (a) Polarity dependence of the proton migration length (ℓ_p) for various fixed temperatures. The right panels show optical microscopy images of NNO channel with and without HNNO area (b) Optical microscopy images of samples after hydrogenation at 473 K with V = -10 V, 0 V, and +10 V.

4.4. Conclusion

The electrical resistance modulation of NNO thin-film resistors during hydrogenation was systematically investigated under a range of temperatures and both polarities of the applied bias voltage. By utilizing the catalytic effect in a heteroelectrode configuration, I was able to identify the correlation between the polarity of electric field and the proton migration length, which was affected by temperature. The combination of an electric field and thermal activation is shown to be an effective method for controlling the proton doping distribution in NNO film. My investigation through this set of measurements could be useful in the future to guide process envelopes for the gas-phase doping of perovskites whose properties are sensitive to hydrogen and, in a broader context, iontronic devices that rely on ion motion within a solid lattice to function.

4.5. Reference

1) Catalan, G. Progress in Perovskite Nickelate Research. *Phase Transitions.* **2008**, *81.7–8*, 729–749.
2) Shi, J.; Ha, S. D.; Zhou, Y.; Schoofs, F.; Ramanathan, S. A Correlated Nickelate Synaptic Transistor. *Nat. Commun.* **2013**, *4.1*, 1–9.
3) Ha, S. D.; Shi, J.; Meroz, Y.; Mahadevan, L.; Ramanathan, S. Neuromimetic Circuits with Synaptic Devices based on Strongly Correlated Electron Systems. *Phys. Rev. Appl.* **2014**, *2.6*, 064003.
4) Wang, L.; Dash, S.; Chang, L.; You, L.; Feng, Y.; He, X.; Jin, K. J.; Zhou, Y.; Ong, H. G.; Ren, P.; Wang, S. Oxygen Vacancy Induced Room-Temperature Metal–Insulator Transition in Nickelate Films and Its Potential Application in Photovoltaics. *ACS Appl. Mater. Interfaces.* **2016**, *8.15*, 9769–9776.

5) Chang, L.; Wang, L.; You, L.; Zhou, Y.; Fang, L.; Wang, S.; Wang, J. Band Gap Tuning of Nickelates for Photovoltaic Applications. *J. Phys. D: Appl. Phys.* **2016**, *49.44*, 44LT02.

6) Scherwitzl, R.; Zubko, P.; Lichtensteiger, C.; Triscone, J. M. Electric-Field Tuning of The Metal–Insulator Transition in Ultrathin Films of $LaNiO_3$. *Appl. Phys. Lett.* **2009**, *95.22*, 222114.

7) Asanuma, S.; Xiang, P. H.; Yamada, H.; Sato, H.; Inoue, I. H.; Akoh, H.; Sawa, A.; Ueno, K.; Shimotani, H.; Yuan, H.; Kawasaki, M. Tuning of The Metal–Insulator Transition in Electrolyte-Gated $NdNiO_3$ Thin Films. *Appl. Phys. Lett.* **2010**, *97.14*, 142110.

8) Ha, S. D.; Vetter, U.; Shi, J.; Ramanathan, S. Electrostatic Gating of Metallic and Insulating Phases in $SmNiO_3$ Ultrathin Films. *Appl. Phys. Lett.* **2013**, *102.18*, 183102.

9) Shi, J.; Zhou, Y.; Ramanathan, S. Colossal Resistance Switching and Band Gap Modulation in A Perovskite Nickelate by Electron Doping. *Nat. Commun.* **2014**, *5.1*, 1–9.

10) Oh, C.; Jo, M.; Son, J. All-Solid-State Synaptic Transistors with High-Temperature Stability Using Proton Pump Gating of Strongly Correlated Materials. *ACS Appl. Mater. Interfaces*. **2019**, *11.17*, 15733–15740.

11) Zhu, L. Q.; Wan, C. J.; Gao, P. Q.; Liu, Y. H.; Xiao, H.; Ye, J. C.; Wan, Q. Flexible Proton-Gated Oxide Synaptic Transistors on Si Membrane. *ACS Appl. Mater. Interfaces*. **2019**, *8.33*, 21770–21775.

12) Hanada, A.; Kinoshita, K.; Kishida, S. Resistive Switching by Migration of Hydrogen Ions. *Appl. Phys. Lett.* **2012**, *101.4*, 043507.

13) Shimojo, F.; Hoshino, K.; Okazaki, H. First-Principles Molecular-Dynamics Simulation of Proton Diffusion in Perovskite Oxides. *Solid State Ionics*. **1998**, *113*, 319–323.

14) Lan, C.; Li, H.; Zhao, S. A First-Principles Study of The Proton and Oxygen Migration Behavior in The Rare-Earth Perovskite $SmNiO_3$. *J. Comput. Electron.* **2020**, *19*, 905–909.

15) Alonso, J. A.; Martinez-Lope, M. J.; Casais, M. T.; Aranda, M. A.; Fernandez-Diaz, M. T. Metal−Insulator Transitions, Structural and Microstructural Evolution of $RNiO_3$ (R = Sm, Eu, Gd, Dy, Ho, Y) Perovskites: Evidence for Room-Temperature Charge Disproportionation in Monoclinic $HoNiO_3$ and $YNiO_3$. *J. Am. Chem. Soc.* **1999**, *121.20*, 4754–4762.

16) Canfield, P. C.; Thompson, J. D.; Cheong, S. W.; Rupp, L. W. Extraordinary Pressure Dependence of The Metal-to-Insulator Transition in The Charge-Transfer Compounds $NdNiO_3$ and $PrNiO_3$. *Phys. Rev. B.* **1993**, *47.18*, 12357.

17) Catalan, G.; Bowman, R. M.; Gregg, J. M. Metal-Insulator Transitions in $NdNiO_3$ Thin Films. *Phys. Rev. B*. **2000**, *62.12*, 7892.

18) Yamanaka, T.; Hattori, A. N.; Pamasi, L. N.; Takemoto, S.; Hattori, K.; Daimon, H.; Sato, K.; Tanaka, H. Effects of Off-Stoichiometry in The Epitaxial $NdNiO_3$ Film on The Suppression of Its Metal-Insulator-Transition Properties. *ACS Appl. Electron. Mater.* **2019**, *1.12*, 2678-2683.

CHAPTER 5

Strain Effect on Proton-Memristive $NdNiO_3$ Thin Film Devices

ABSTRACT

I investigate resistance switching in proton-memristive $NdNiO_3$ film devices via the diffusional migration of a proton dopant by using electric field control. Lattice strain is found to play a significant role in determining proton migration within $NdNiO_3$ thin film. Compressive strain can accelerate the migration, resulting in a switching efficiency of 28.22% that is significantly higher than 0.21% on a tensile-strained device. The results demonstrate the significance of strain engineering and will guide the development of the design of multifunctional perovskite devices for emerging iontronics memory and computing applications

5.1. Background

Correlated perovskite $RNiO_3$ (R = rare earth) thin film possesses the potential to enable densely scaled resistive switching for emerging nonvolatile memory and neuromorphic computing applications.[1–5] The remarkable switching feature in this material is characterized by the abrupt Mott phase transition that originates from strong correlations between localized transition metal valence *d* electrons.[6,7] Its complex electronic phase diagrams are extremely sensitive to external stimuli, e.g., temperature,[8,9] pressure,[10,11] confinement,[12,13] electrostatic doping,[14,15] and strain,[16–18] which can markedly transform its phase from metallic to insulating (metal–insulator transition, MIT). Among several approaches to trigger the MIT phenomenon in $RNiO_3$, proton doping via chemical reaction (hydrogenation) has been intensively investigated[19–21] since the prominent demonstration of inducing a colossal resistance modulation of ~10^8 order magnitude in $SmNiO_3$ film.[22]

A proton, compared with other ionic species, has a small radius and high ion mobility.[23,24] These characteristics enable a highly tunable proton migration and distribution area through the manipulation of external electric fields.[2] This facile electric-field-induced

proton migration can generate resistance change and potentially realize an extremely sensitive correlated-iontronics device to overcome the limitations of the typical oxide switching device. For instance, since a proton has a higher ion mobility than an oxygen ion, a protonic RNiO$_3$ device can potentially improve the switching speed and power compared with the typical oxide device that relies on the movement of oxygen vacancies in insulating oxides.[25] At the same time, there is a need for innovation in the engineering design of RNiO$_3$-memristive devices to maximize the potential use of facile proton migration to improve device performance.

5.2. Objective

In this work, I investigate strain engineering via substrate selection as an approach to accelerate electric-field-driven proton migration in strongly correlated NdNiO$_3$ (NNO) thin film devices. **Figure 5.1**a illustrates the concept of proton migration in a strained-NNO memristive device. Protons, which are initially doped via hydrogenation (HNNO region), can be redistributed via electric field control. The electric field can cause protons to migrate to expand the highly resistive HNNO region ($\Delta\ell^{E}$, proton migration length on applying an electric field). In-plane compressive strain can accelerate and thus ease the proton migration to improve switching operation. In contrast, in-plane tensile stress will suppress the migration, resulting in impaired switching performance. My results support this concept and show that lattice strain tuning is of importance in designing high-performance protonic RNiO$_3$ memristive devices.

5.3. Results and Discussion

5.3.1. Proton Doping in Strained-NNO Memristive Device

The samples were fabricated by depositing ~80-nm-thick NNO films on LaAlO$_3$ (LAO) and KTaO$_3$ (KTO) substrates by pulsed laser deposition (PLD; ArF excimer, λ = 193 nm, 3 Hz,

90 mJ/pulse). Prior to deposition, the growth chamber was evacuated to a base pressure of ~1 × 10^{-6} Pa. The deposition temperature was 923 K with an oxygen pressure of 30 Pa. The as-deposited NNO films were 2θ-ω-scanned (out-of-plane) using an X-ray diffraction (XRD) system (UltimaIV, Rigaku) to investigate the crystal structure. The 2θ-ω XRD patterns (Cu Kα) for the deposited NNO films, presented in Figure S5.1 (see: Supporting Information for Chapter 5), show *c*-axis-oriented growth with engineered strains. To accommodate hydrogenation-proton doping, the films were fabricated into two-terminal devices with different electrodes of Pt and Au–Ti, as shown in Figure 5.1a. First, the films were patterned by photolithography (PLS-1000, PMT Corp.). Then, the films were dry-etched using an Ar ion milling system (IBE-KDC75-EPD-OU-TA, Hakuto) to form the device channel with width × length = 10 μm × 10 μm. Next, after patterning the electrodes by photolithography, Pt and Au–Ti were deposited on top of the NNO films by RF sputtering (SVC-700RFII). Finally, resist lift-off using acetone at 343 K was carried out to complete the device fabrication process. In this device configuration, protons from the hydrogenation process concentrate in the vicinity of the Pt electrode only (HNNO region) but not in that of the Au–Ti electrode. This is because only Pt acts as a catalyst for the dissociation of H_2 molecules into proton ions.[23] This arrangement helps us to easily observe the effect of proton migration, which herein is driven by the external electric field. Protons were introduced into the NNO lattice via hydrogenation (95% Ar + 5% H_2) at 473 K. The electrical measurements of the films were performed using a source meter (2634B, Keithley). The voltage polarity for electric field control is referenced with respect to the Pt electrode. The intrinsic electrical properties of the films, as shown in Figure S5.2, are presented as temperature-dependent resistivity (ρ–T) plots. The plots indicate that the MIT characteristics of the films vary depending on the substrate. The 2θ-ω XRD and ρ–T plots are in good agreement with the results of previous studies and demonstrate the high quality of the fabricated NNO films.[26,27]

The three-dimensional network of NiO_6 octahedra determines the fundamental properties of perovskite NNO ($a_{\text{pseudocubic (pc)}}$ = 3.807 Å), which, at the same time, is exceptionally sensitive to lattice strain.[28,29] In this regard, selected substrates of LAO (a_{pc} = 3.789 Å) and KTO (a = 3.989 Å) will induce −0.47% compressive and +4.78% tensile strains in the NNO lattice,[30] respectively, and thus are expected to provide information on how each of these opposite strains affects the device operation.

Figure 5.1b shows the translucent HNNO region after hydrogenation for 30 min. The translucent color near the Pt electrode corresponds to the hydrogen dissociation and adsorption process.[22,31] From this figure, we can see that the HNNO region on NNO–LAO is wider than that on NNO–KTO, indicating that protons diffuse further within the NNO–LAO lattice than within the NNO–KTO lattice. After hydrogenation, the number of protons within the NNO channel was controlled to an appropriate amount by desorbing or removing protons via annealing at 473 K in air (dehydrogenation). The real-time resistance evolutions during hydrogenation and dehydrogenation are shown in Figs. S5.3 and S5.4 (see Supplementary Data), respectively.

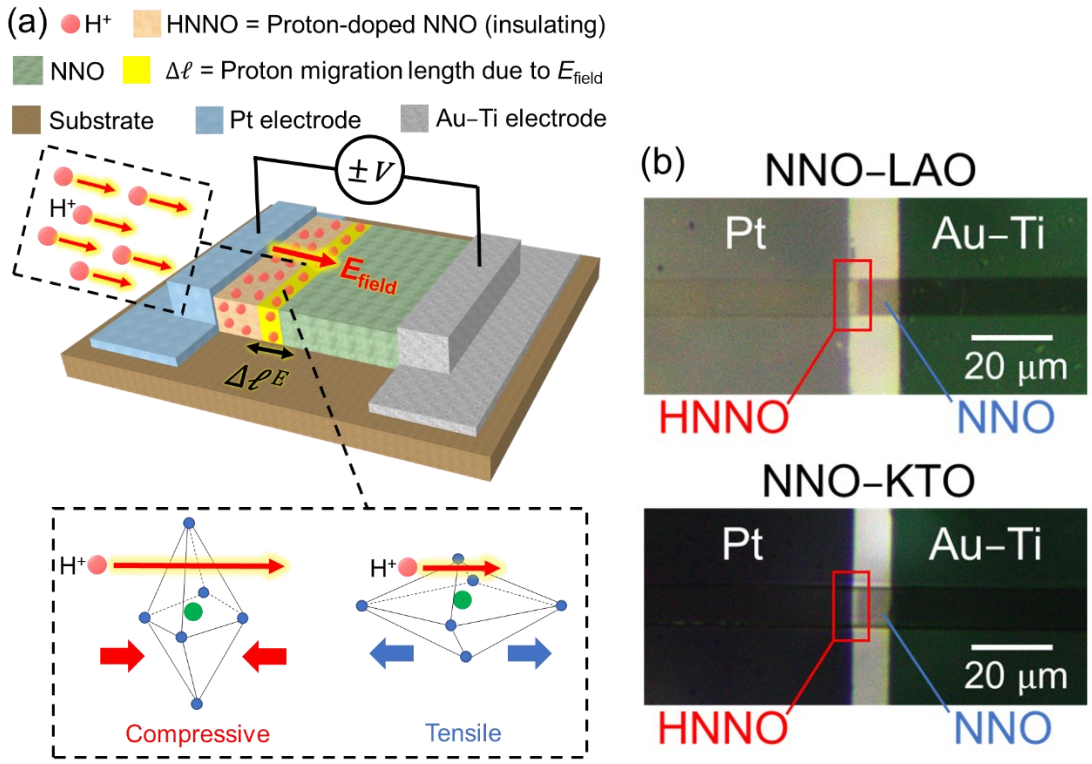

Figure 5.1. (a) Schematic illustration of proton migration in strained-NNO memristive device with electric field control. (b) Optical microscopy images of NNO–LAO and NNO–KTO devices after hydrogenation at 473 K for 30 min. The difference in image brightness between the samples originated from the optical characteristics of the substrates.

5.3.2. Electric Field-Controlled Resistance of Strained-NNO Memristive Device

Figure 5.2a indicates the electric field control of the resistance of the proton-doped NNO–LAO device. Here, an electric field was applied to the device and drove protons further within the NNO lattice. Protons migrated for a particular duration before reaching saturation, as indicated by the plateau resistance. Each curve in Figure 5.2a represents a sample with a distinct initial amount of proton doping. Here, the initial amount of doping is expressed as the resistance after hydrogenation and dehydrogenation divided by the pristine resistance ($R_{Doped}/R_{Pristine}$). The result shows that the magnitude of electric-field-driven resistance ($R_{E\text{-}field}$)

varies with each initial amount of doping. At $R_{Doped}/R_{Pristine}$ = 3, an applied voltage of +8 V at 300 K increases the resistance by ~10^2. The resistance further increases by ~10^3 and ~10^4 with higher $R_{Doped}/R_{Pristine}$ values of 10 and 55, respectively. The inset shows that an insignificant resistance change is obtained when a relatively high $R_{Doped}/R_{Pristine}$ of 190 is employed. Compared with NNO–LAO, Figure 5.2b shows no significant change in resistance after the application of an electric field to the NNO–KTO device, regardless of the amount of doping. The highest change is only ~10^2 with $R_{Doped}/R_{Pristine}$ of 40. These results show that, compared with the tension-strained film, the compressively strained NNO lattice can ease proton migration, thus resulting in a larger change in resistance.

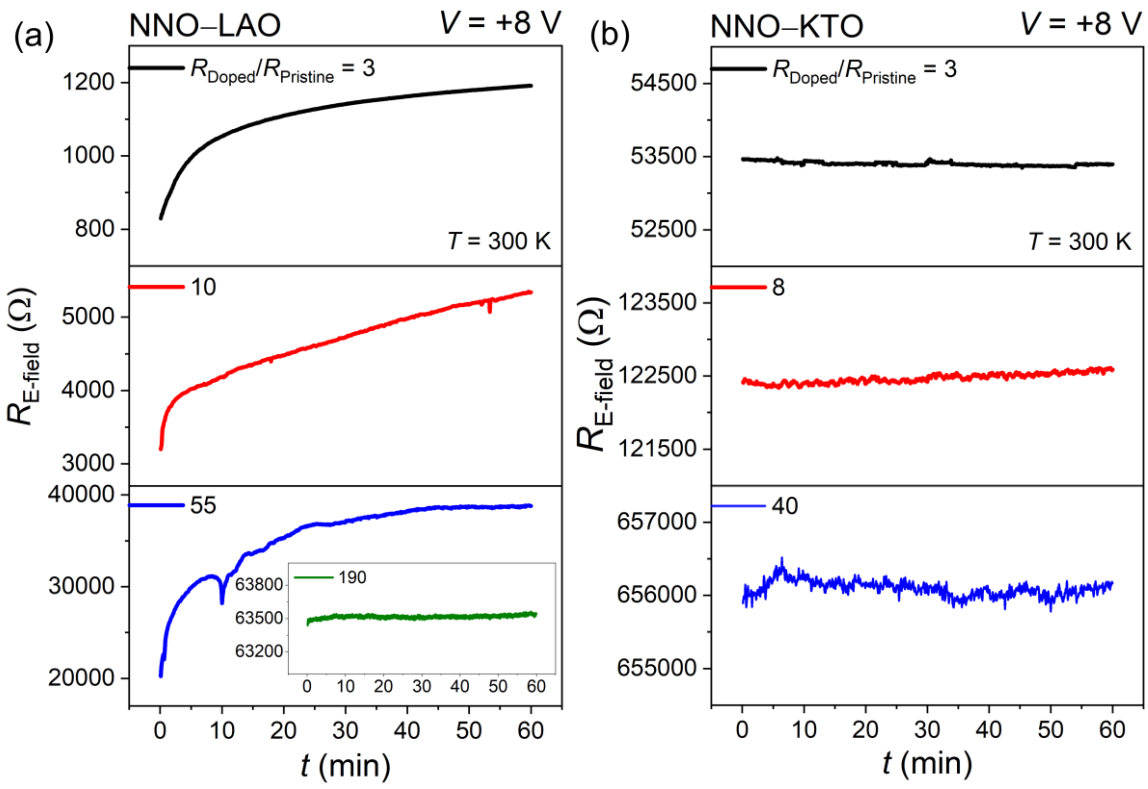

Figure 5.2. Effect of electric field shown in time-dependent resistance change of (a) NNO–LAO and (b) NNO–KTO devices with various initial amounts of doping ($R_{Doped}/R_{Pristine}$).

Figure 5.3 clearly shows this difference where the resistance modulation, presented as $R_{\text{Modulation}} = (R_{\text{After e-field}} - R_{\text{Before e-field}})/R_{\text{Before e-field}}$, is plotted against the initial amount of doping. Here, $R_{\text{Modulation}}$ is utilized to signify a marked difference between these distinct strain systems. This figure reveals that, at any initial amount of proton doping, compressive NNO–LAO attains a higher $R_{\text{Modulation}}$ than tensile NNO–KTO. Additionally, as shown for NNO–LAO, I observe a linear scaling of $R_{\text{Modulation}}$ with the exponential increment of the amount of doping before it abruptly disappears when the amount of doping exceeds the limit. However, no significant resistance change is observed on NNO–KTO at any amount of doping. This indicates that while the tensile lattice suppresses proton migration, compressive strain can accelerate proton migration, where the effectiveness can be tuned by applying a proper initial amount of doping.

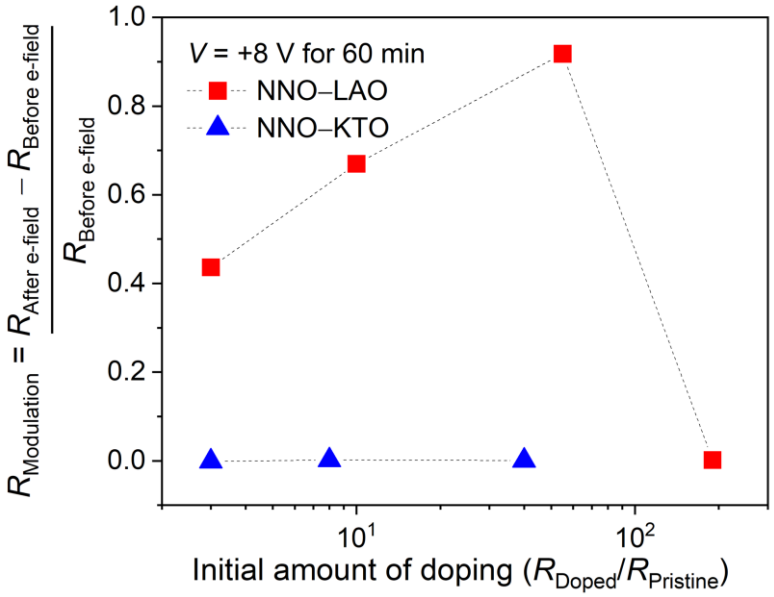

Figure 5.3. Resistance modulation plotted against initial amount of doping for electric field-driven NNO thin film devices.

5.3.3. Switching Efficiency of Strained-NNO Memristive Device

I further studied the bistate switching in our NNO devices by applying pulse voltages of ±1 V and ±8 V while keeping the pulse duration fixed at 10 s. Figure **5.4**a shows that the resistance state of the NNO–LAO device switches depending on the polarity of the applied voltage. The device, which was initially set in the high resistance state (HRS) by the application of a positive voltage (+V), can be switched to the low resistance state (LRS) by applying a negative voltage (−V). This implies that when the bias voltage is positive, the proton distribution area is expanding, which results in increasing resistance. On the other hand, the decreasing resistance when a negative bias is applied results from the reduced proton distribution area. In our measurement series, the highest switching margins between HRS and LRS ($R_+ - R_-$) in NNO–LAO are ~10^3 Ω and ~10^1 Ω for applied voltages of ±8 V and ±1 V, respectively. This shows that this operation can be controlled by the magnitude of the applied voltage; where a higher voltage provides a larger resistance change than a lower voltage. As shown in Figure 5.4b, these characteristics also appear in the NNO–KTO proton-memristive device, where the highest $R_+ - R_-$ values are ~10^2 Ω and ~10^1 Ω for ±8 V and ±1 V, respectively. For a better display of our measurement series, the average switching efficiency $\overline{\eta}$ is shown in **Table 5.1** where

$$\overline{\eta} = \frac{\sum_{i=1}^{n} \frac{R_+ - R_-}{R_-}}{n} \qquad (5.1).$$

We can see in Table 5.1 that an application of ±8 V results in $\overline{\eta}$ values of 28.22% for NNO–LAO and 0.21% for NNO–KTO. In addition, $\overline{\eta}$ values of 1.21% and 0.05% are observed when ±1 V is applied to NNO–LAO and NNO–KTO, respectively. These results show that

compressive NNO–LAO enables a higher $\overline{\eta}$ value of ~10^2 than tensile NNO–KTO. This tendency can be explained by

$$\Delta \ell^E = \frac{\Delta t \; q \; D \; V}{k_B \; T \; L} \qquad (5.2),$$

where $\Delta \ell^{E}$ is the proton migration length, Δt is the duration of applied electric field, q is the electric charge of proton, D is the diffusion constant of proton, V is the applied voltage, k_B is the Boltzmann constant, T is the temperature, and L is the device channel length. The derivation of Equation (5.2) is presented in supplementary data. Since the diffusing protons correspond to resistance switching ($\Delta R_{\text{E-field}}$), here it is assumed that $\Delta \ell^{E} \approx \Delta R_{\text{E-field}}$. Thus, from Equation (5.2), $\Delta R_{\text{E-field}}$ for a duration Δt at T is affected by D. In other words, D is the intrinsic property of protons that can be controlled to manipulate proton migration and hence resistance modulation. This is experimentally demonstrated by the translucent HNNO region of NNO–LAO that is wider than that of NNO–KTO in Figure 5.1b. The applied electric field here provides a driving force for proton migration in terms of its polarity. With regard to my results, this relationship suggests that compressive strain can ease the acceleration of D.

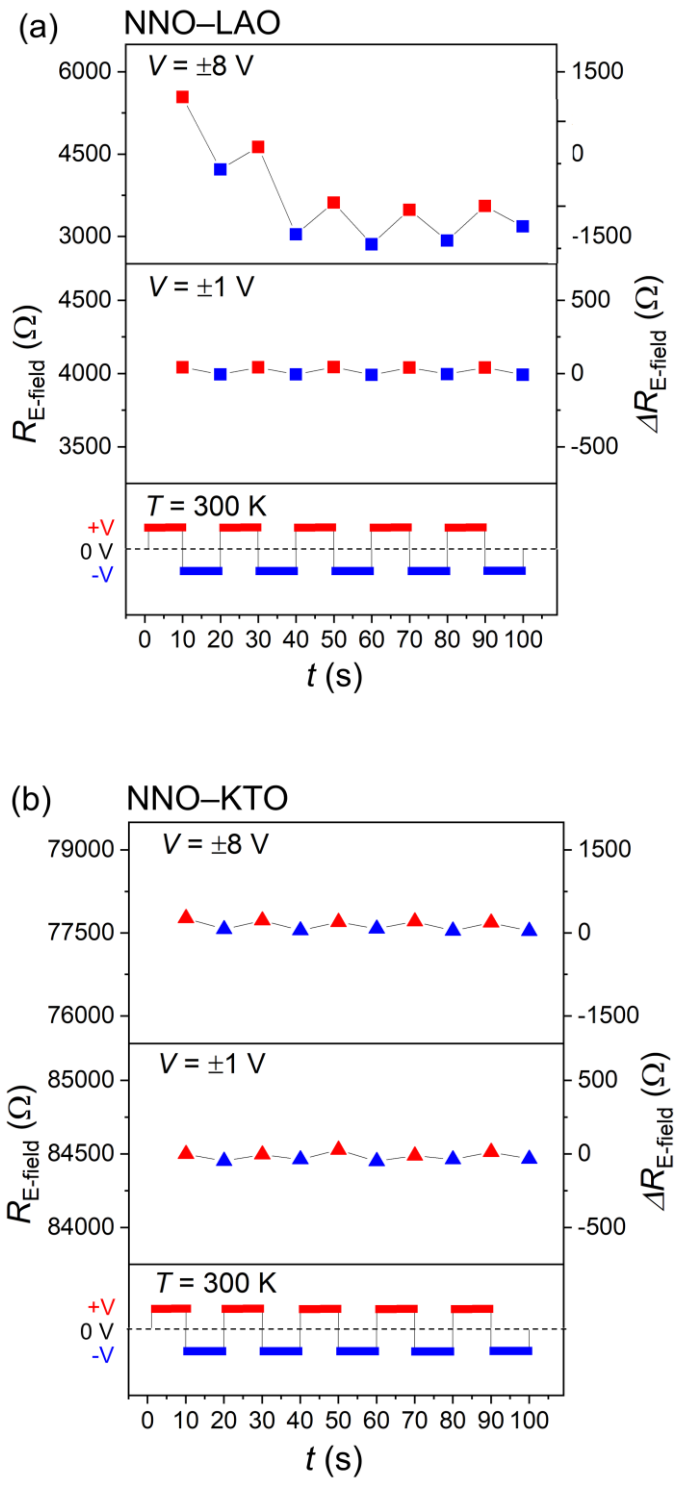

Figure 5.4. Demonstration of electric-field-controlled resistance switching in (a) NNO–LAO and (b) NNO–KTO devices measured with $V = \pm 1$ V and ± 8 V at $T = 300$ K. The y-axis at the left side is the measured resistance. ΔR is provided on the right-side y-axis for easy comparison among the panels.

Table 5.1. Switching efficiency $\overline{\eta}$ values of NNO–LAO and NNO–KTO proton-memristive devices with ±1 V and ±8 V.

	V = ±1 V	V = ±8 V
$\overline{\eta}_{\text{NNO–LAO}}$ (%)	1.21	28.22
$\overline{\eta}_{\text{NNO–KTO}}$ (%)	0.05	0.21

5.4. Conclusion

In summary, I have demonstrated resistance change in proton-memristive NNO thin film devices. I have shown that lattice strain can be a significant factor in determining the switching operation of protonic perovskite-memristive devices. These results can lead to an important strategy for overcoming the bottleneck in designing protonic RNiO$_3$ thin film devices and is of relevance for emerging computing and memory applications.

5.5. Reference

1) Ha, S. D.; Aydogdu, G. H.; Ramanathan, S. Metal-insulator transition and electrically driven memristive characteristics of $SmNiO_3$ thin films. *Appl. Phys. Lett.* **2011,** *98,* 012105.
2) Oh, C.; Heo, S.; Jang, H. M.; Son, J. Correlated memory resistor in epitaxial $NdNiO_3$ heterostructures with asymmetrical proton concentration. *Appl. Phys. Lett.* **2016,** *108*, 122106.
3) Ramadoss, K.; Zuo, F.; Sun, Y.; Zhang, Z.; Lin, J.; Bhaskar, U.; Shin, S.; Alam, M. A.; Guha, S.; Weinstein, D.; Ramanathan, S. Proton-doped strongly correlated perovskite nickelate memory devices. *IEEE Electron Device Lett.* **2018,** *39,* 1500.

4) Zhang, H. T.; Park, T. J.; Zaluzhnyy, I. A.; Wang, Q.; Wadekar, S. N.; Manna, S.; Andrawis, R.; Sprau, P. O.; Sun, Y.; Zhang, Z.; Huang, C.; Zhou, H.; Zhang, Z.; Narayanan, B.; Srinivasan, G.; Hua, N.; Nazaretski, E.; Huang, X.; Yan, H.; Ge, M.; Chu, Y. S.; Cherukara, M. J.; Holt, M. V.; Krishnamurthy, M.; Shpyrko, O. G.; Sankaranarayanan, S. K. R. S.; Frano, A.; Roy, K.; Ramanathan, S. Perovskite neural trees. *Nat. Commun.* **2020,** *11*, 2245.

5) Ha, S. D.; Shi, J.; Meroz, Y.; Mahadevan, L.; Ramanathan, S. Neuromimetic circuits with synaptic devices based on strongly correlated electron systems. *Phys. Rev. Appl.* **2014,** *2,* 064003.

6) Stemmer, S; Millis; A. J. Quantum confinement in oxide quantum wells. *MRS Bull.* **2013,** *38,* 1032.

7) Imada, M.; Fujimori, A.; Tokura, Y. Metal-insulator transitions. *Rev. Mod. Phys.* **1998,** *70*, 1039.

8) Torrance, J. B.; Lacorre, P.; Nazzal, A. I.; Ansaldo, E. J.; Niedermayer, C. Systematic study of insulator-metal transitions in perovskites RNiO$_3$ (R=Pr,Nd,Sm,Eu) due to closing of charge-transfer gap. *Phys. Rev. B.* **1992,** *45,* 8209.

9) Medarde, M. L. Structural, magnetic and electronic properties of perovskites (R= rare earth). *J. Phys.: Condens. Matter.* **1997,** *9,* 1679.

10) Zhou, J. S.; Goodenough, J. B.; Dabrowski, B. Pressure-Induced Non-Fermi-Liquid Behavior of PrNiO$_3$. *Phys. Rev. Lett.* **2005,** *94*, 226602.

11) Canfield, P. C.; Thompson, J. D.; Cheong, S. W.; Rupp, L. W. Extraordinary pressure dependence of the metal-to-insulator transition in the charge-transfer compounds NdNiO$_3$ and PrNiO$_3$. *Phys. Rev. B* **1993,** *47,* 12357.

12) Boris, A. V.; Matiks, Y.; Benckiser, E.; Frano, A.; Popovich, P.; Hinkov, V.; Wochner, P.; Castro-Colin, M.; Detemple, E.; Malik, V. K.; Bernhard, C.; Prokscha, T.; Suter, A.;

Salman, Z.; Morenzoni, E.; Cristiani, G.; Habermeier, H. U.; Keimer, B. Dimensionality control of electronic phase transitions in nickel-oxide superlattices. *Science* **2011**, *332,* 937.

13) Son, J.; LeBeau, J. M.; Allen, S. J.; Stemmer, S. Conductivity enhancement of ultrathin $LaNiO_3$ films in superlattices. *Appl. Phys. Lett.* **2010,** *97,* 202109.

14) Scherwitzl, R.; Zubko, P.; Lezama, I. G.; Ono, S.; Morpurgo, A. F.; Catalan, G.; Triscone, J. M. Electric-Field Control of the Metal-Insulator Transition in Ultrathin $NdNiO_3$ Films. *Adv. Mater.* **2010,** *22,* 5517.

15) Asanuma, S.; Xiang, P. H.; Yamada, H.; Sato, H.; Inoue, I. H.; Akoh, H.; Sawa, A.; Ueno, K.; Shimotani, H.; Yuan, H.; Kawasaki, M.; Iwasa, Y. Tuning of the metal-insulator transition in electrolyte-gated $NdNiO_3$ thin films. *Appl. Phys. Lett.* **2010,** *97,* 142110.

16) Li, M.; Gao, Z.; Wang, X.; Kang, C.; Liu, X.; Jia, C.; Luo, C.; Zhang, W. J. Non-volatile resistance switching in $LaNiO_3$ films on PMN-PT substrates. *Phys. D: Appl. Phys.* **2020,** *53,* 325306.

17) Son, J.; Moetakef, P.; LeBeau, J. M.; Ouellette, D.; Balents, L.; Allen, S. J.; Stemmer, S. Low-dimensional Mott material: Transport in ultrathin epitaxial $LaNiO_3$ films. Appl. Phys. Lett. **2010**, *96,* 062114.

18) Ouellette, D. G.; Lee, S.; Son, J.; Stemmer, S.; Balents, L.; Millis, A. J.; Allen, S. Optical conductivity of $LaNiO_3$: Coherent transport and correlation driven mass enhancement. *J. Phys. Rev. B* **2010**, *82*, 165112.

19) Chen, J.; Mao, W.; Gao, L.; Yan, F.; Yajima, T.; Chen, N.; Chen, Z.; Dong, H.; Ge, B.; Zhang, P.; Cao, X. Electron-Doping Mottronics in Strongly Correlated Perovskite. *Adv. Mater.* **2020,** *32,* 1905060.

20) Chen, J.; Mao, W.; Ge, B.; Wang, J.; Ke, X.; Wang, V.; Wang, Y.; Döbeli, M.; Geng, W.; Matsuzaki, H.; Shi, J. Revealing the role of lattice distortions in the hydrogen-induced metal-insulator transition of $SmNiO_3$. *Nat. Commun.* **2019,** *10,* 694.

21) Xu, X.; Liu, C.; Ma, J.; Jacobson, A. J.; Nan, C.; Chen, C. Physicochemical properties of proton-conducting $SmNiO_3$ epitaxial films. *J. Materiomics*, **2019**, *5,* 247.

22) Shi, J.; Zhou, Y.; Ramanathan, S. Colossal resistance switching and band gap modulation in a perovskite nickelate by electron doping. *Nat. Commun*. **2014**, ***5***, 4860.

23) Hanada, A.; Kinoshita, K.; Kishida, S. Resistive switching by migration of hydrogen ions. *Appl. Phys. Lett.* **2012,** *101,* 043507.

24) Zhang, H. T.; Zhang, Z.; Zhou, H.; Tanaka, H.; Fong, D. D.; Ramanathan, S. Beyond electrostatic modification: design and discovery of functional oxide phases via ionic-electronic doping. *Adv. Phys.: X* **2019,** *4,* 1523686.

25) Akinaga, H.; Shima, H. Resistive random access memory (ReRAM) based on metal oxides. *Proc. IEEE* **2010,** *98*, 2237.

26) Catalan, G.; Bowman, R. M.; Gregg, J. M. Metal-insulator transitions in $NdNiO_3$ thin films. *Phys. Rev. B* **2000,** *62,* 7892.

27) Scherwitzl, R.; Zubko, P.; Lezama, I. G.; Ono, S.; Morpurgo, A. F.; Catalan, G.; Triscone, J. Electric-Field Control of the Metal-Insulator Transition in Ultrathin $NdNiO_3$ Films. *Adv. Mater.* **2010,** 22*,* 5517.

28) Catalano, S.; Gilbert, M.; Fowlie, J.; Íñiguez, J.; Triscone, J. M.; Kreisel, Rare-earth nickelates $RNiO_3$: thin films and heterostructures. *J. Rep. Prog. Phys.* **2018,** *81,* 046501.

29) Hauser, A. J.; Mikheev, E.; Moreno, N. E.; Hwang, J.; Zhang, J. Y.; Stemmer, S. Correlation between stoichiometry, strain, and metal-insulator transitions of $NdNiO_3$ films. *Appl. Phys. Lett.* **2015,** *106,* 092104.

30) Hepting, M. *Ordering Phenomena in Rare-Earth Nickelate Heterostructures* (Springer, Cham, 2017) 1st ed., p. 145.

31) Zhang, Y.; Knibbe, R.; Sunarso, J.; Zhong, Y.; Zhou, W.; Shao, Z.; Zhu, Z. Recent progress on advanced materials for solid-oxide fuel cells operating below 500 C. *Adv. Mater.* **2017**, *29,* 1700132.

Supporting information for CHAPTER 5

Strain Effect on Proton-Memristive $NdNiO_3$ Thin Film Devices

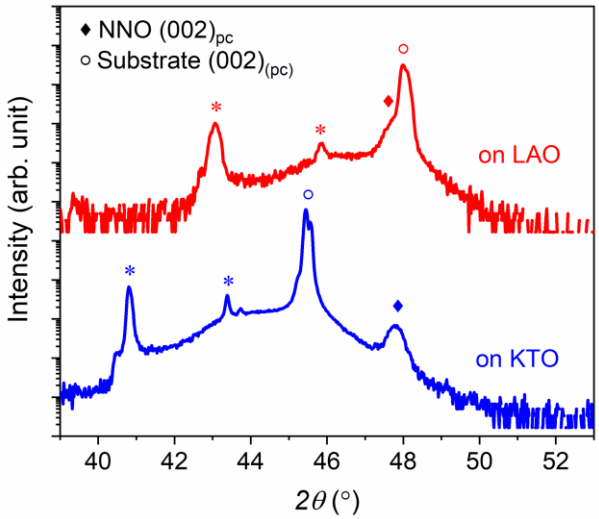

Figure S5.1. 2θ-ω XRD patterns (Cu Kα) of NNO films deposited on LAO and KTO substrates. The peaks marked by an asterisk (*) originated from the substrates.

The peaks at 2θ ~48.03° and ~45.43° are assigned to $002_{\text{pseudocubic (pc)}}$ reflections of NNO–LAO and NNO–KTO films, respectively (PDF no. 01-079-2459). It is seen from the patterns that, regardless of the substrate, *c*-axis-oriented NNO films were grown without any detectable impurity phase.

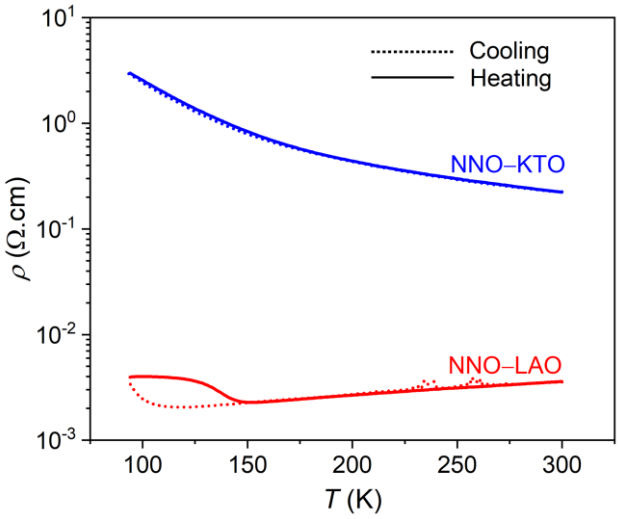

Figure S5.2. Temperature-dependent resistivity (ρ–T) curves of pristine NNO films deposited on LAO and KTO substrates.

NNO–LAO shows MIT characteristics at the transition temperature of 150 K, similarly to those described in other reports of NNO films.[1)] On the other hand, MIT was not observed on NNO–KTO. This is because of the large lattice mismatch at the substrate–film interface where similar characteristics have been reported in NNO films deposited on MgO.[1)] In addition, the different levels of lattice strain in NNO–LAO and NNO–KTO also contribute to the different magnitudes of their resistivities.[2)]

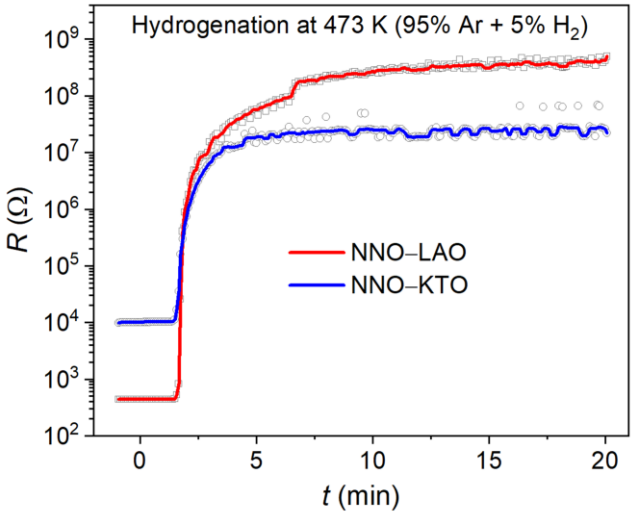

Figure S5.3. Real-time resistance evolution during hydrogenation (95% Ar + 5% H_2) of NNO–LAO and NNO–KTO devices at 473 K for 30 min. Hydrogenation started at t = 0. The raw data represented by gray symbols were smoothed into line graphs using a 50% percentile filter in OriginLab.[3)]

During hydrogenation (95% Ar + 5% H_2), the resistance of the memristor increased with time, indicating catalytic proton adsorption, as shown in Figure S5.3. The resistance of NNO–LAO increased by ~10^6 whereas a resistance modulation of ~10^3 was observed on NNO–KTO. This indicates that protons diffuse further within the NNO lattice with the compressive LAO substrate than in that with the tensile KTO substrate.

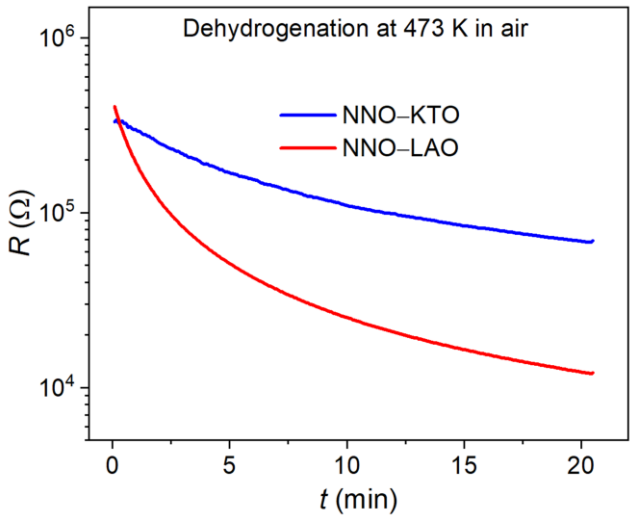

Figure S5.4. Resistance versus time during dehydrogenation of NNO–LAO and NNO–KTO at 473 K in air.

When annealed at 473 K in air (dehydrogenation), protons desorbed out from the NNO lattice. This is demonstrated by the decreasing resistance shown in Figure S5.4, where the rate was higher on NNO–LAO than on NNO–KTO.

Equation (5.2) can be derived from Einstein's relation and the formula for charged particle velocity under E_{field}:

$$D = \frac{\mu\, k_B\, T}{q}$$

$$\upsilon_d = \mu\, E_{field}$$

where D is the diffusion constant of proton, υ_d is the proton drift velocity, μ is the proton mobility, k_B is the Boltzmann constant, T is the temperature, q is the electric charge of proton, and E_{field} is the electric field. Since $\upsilon_d = \Delta\ell^E / \Delta t$, herein, $\Delta\ell^E$ can be expressed as

$$\frac{\Delta \ell^E}{\Delta t} = \frac{q\ D}{k_B\ T}\ E_{field}$$

$$\Delta \ell^E = \frac{\Delta t\ q\ D\ V}{k_B\ T\ L} \qquad (5.2),$$

where $\Delta \ell^E$ is the proton migration length, Δt is the duration of the applied electric field, V is the applied voltage, and L is the memristor channel length.

Reference

1) Catalan, G.; Bowman, R. M.; Gregg, J. M. Metal-insulator transitions in $NdNiO_3$ thin films. *Phys. Rev. B* **2000,** *62,* 7892.
2) Scherwitzl, R.; Zubko, P.; Lezama, I. G.; Ono, S.; Morpurgo, A. F.; Catalan, G.; Triscone, J. Electric-Field Control of the Metal-Insulator Transition in Ultrathin $NdNiO_3$ Films. *Adv. Mater.* **22***,* 5517 (2010).
3) OriginLab, 18.1 Smoothing, https://www.originlab.com/doc/origin-help/smoothing, accessed: April, 2022.

CHAPTER 6

General Discussion

In this study, I investigated proton diffusion phenomena in strongly correlated perovskite $NdNiO_3$ (NNO) thin film. Proton was introduced into NNO lattice via gas-phase-chemical annealing called hydrogenation process. The corresponding resistance modulation, which is a result of proton diffusion, was observed during hydrogenation process and device operation as a function of external control such as regulated lattice strain and applied electric field.

In Chapter 3, I established a correlation between lattice strain and proton diffusion in $RNiO_3$ lattice during hydrogenation. Through my innovative experimental method, supported by computational analysis, I reveal the significance of strain-controlled proton diffusion in determining the resistance modulation during the hydrogenation-induced phase transition. A compressive strain of -0.03% was shown to effectively improve proton diffusion resulting in colossal resistance modulation of $\sim 10^6$. On the other hand, a relatively small resistance modulation of $\sim 10^2$ was observed when +2.57% of tensile strain was regulated in the NNO lattice, indicating a suppressed proton diffusion. The density functional theory (DFT) supported the experimental results, reaffirming the improved diffusion speed by estimating 48 times increment of transition rate of proton in -2% compressively strained-NNO. This result successfully highlights that the rational design of strain engineering is crucial for enabling superlative diffusional doping in $RNiO_3$ perovskites.

In Chapter 4, I applied an electric field assist to control proton diffusion during hydrogenation process. The electric field can effectively boost or suppress the proton diffusion depending on the applied voltage bias. Here, I established a procedure to confirm this finding where the proton diffusion was characterized by the total area of translucent hydrogenated region. Electric field, in addition to thermal activation, is demonstrated to effectively control proton distribution along its gradient. The efficiency of electric field shown in this chapter is

important as a means to drive proton deeper into the correlated perovskite lattice. These results provide a deeper understanding of proton migration in the field of iontronics.

In Chapter 5, utilizing the findings from Chapter 3 and 4, I was able to demonstrate a remarkable improvement of performance in proton-memristive NNO thin film device. Herein, the switching efficiency was successfully improved up to ~10^2 by regulating compressive strain in NNO lattice of the memristive device. This result shows the significance of strain engineering in determining the switching operation of protonic perovskite-memristive devices.

In regard to the long-standing issue in iontronic switching device field, namely slow switching speed compared to that of electronic-transport device, I tried to estimate the enhancement of switching speed obtained in my strained thin film device. From the set of experiment in Chapter 5, the switching speed can be estimated from the average switching efficiency $\overline{\eta}$ and Equation (5.2). Since the proton migration length on applying electric field $\Delta\ell^{E}$ indicates resistance change, i.e., switching efficiency $\overline{\eta}$, thus:

$$\overline{\eta} \approx \Delta\ell^{E} = \frac{\Delta t\ q\ D\ V}{k_B\ T\ L} \qquad (6.1).$$

From Equation (6.1), thus:

$$\frac{\overline{\eta}_{\ NNO-LAO}}{\overline{\eta}_{\ NNO-KTO}} \approx \frac{D_{NNO-LAO}}{D_{NNO-KTO}} \approx \frac{\Delta\ell^{E}_{NNO-LAO}}{\Delta\ell^{E}_{NNO-KTO}} \qquad (6.1.\,\mathrm{i}).$$

The switching speed, *s*, is expressed as:

$$s = \frac{\overline{\eta}}{\Delta t} \qquad (6.2).$$

Since the pulse duration Δt was kept similar in the measurement, thus the enhancement of switching speed can be estimated from Equation (6.2) as:

$$\frac{s_{NNO-LAO}}{s_{NNO-KTO}} = \frac{\overline{\eta}_{NNO-LAO}}{\overline{\eta}_{NNO-KTO}} \qquad (6.2.\text{i}),$$

where the estimated enhancement is about ~134 times under the same level of resistance change. Since the switching speed is essentially determined by the proton diffusion, the enhancement trend of these properties should be directly related. In this regard, to confirm the estimated switching speed enhancement, I tried to compared it with the enhancement of diffusion constant D estimated from the proton migration length observed using optical microscope. Since the proton migration length on applying electric field $\Delta\ell^{E}$ (bi-state switching measurement) was not observable (probably in nanometer order), I estimated the D enhancement from proton migration length after the hydrogenation process at 473 K, denoted as $\Delta\ell^{T}$, instead (shown in Figure 5.1b, $\Delta\ell^{T}$ denotes that the proton migration length was induced by thermal energy). The relationship D and $\Delta\ell^{T}$ is described as:

$$\Delta\ell^{T} = \sqrt{2\,D\,t} \qquad (6.3).$$

Therefore, the enhancement of diffusion constant D at 473 K can be estimated by:

$$\frac{D_{NNO-LAO}}{D_{NNO-KTO}}\Big|_{473\ K} = \left(\frac{\Delta\ell^{T}_{NNO-LAO}}{\Delta\ell^{T}_{NNO-KTO}}\right)^{2} \qquad (6.3.\text{i}).$$

Since the hydrogenation and the bi-state switching measurement of the device were performed at 473 K and at 300 K, respectively, the diffusion constant estimation at this different temperature needs to be compensated. Based on the formula for the temperature dependence of reaction rate, i.e., Arrhenius equation as:

$$D = D_0\, exp\left(\frac{-E_m}{k_B\, T}\right) \qquad (6.4),$$

where D_0 is pre-exponential factor, k_B is Boltzmann constant, and E_m is effective migration barrier, thus:

$$\frac{D_{NNO-LAO}}{D_{NNO-KTO}} = exp\left(\frac{\Delta E_m}{-k_B\, T}\right) \qquad (6.4.\,\text{i}),$$

where $\Delta E_m = E_{m\_NNO-LAO} - E_{m\_NNO-KTO}$. Thus, from Equation (6.4.i):

$$\frac{\left.\frac{D_{NNO-LAO}}{D_{NNO-KTO}}\right|_{T_1}}{\left.\frac{D_{NNO-LAO}}{D_{NNO-KTO}}\right|_{T_2}} = exp\left(\frac{\Delta E_m}{-k_B}\left(\frac{1}{T_1} - \frac{1}{T_2}\right)\right) \qquad (6.4.\,\text{ii}).$$

By inserting $\left.\frac{D_{NNO-LAO}}{D_{NNO-KTO}}\right|_{473\ K}$ defined in Equation (6.3.i) into Equation (6.4.ii) where T_1 = 300 K and T_2 = 473 K, I can estimate the diffusion enhancement at 300 K as:

$$\left.\frac{D_{NNO-LAO}}{D_{NNO-KTO}}\right|_{T_1} = \left(\frac{\Delta \ell^T_{NNO-LAO}}{\Delta \ell^T_{NNO-KTO}}\right)^2 exp\left(\frac{\Delta E_m}{-k_B}\left(\frac{1}{T_1} - \frac{1}{T_2}\right)\right) \qquad (6.5).$$

From the plot of effective migration energy against strain in Figure 3.4c in Chapter 3, I obtained a quadratic fitting curve. From this, I could obtain $E_{m\_NNO\text{-}LAO}$ and $E_{m\_NNO\text{-}KTO}$ of films with strain of NNO-LAO = -0.03% and NNO-KTO = +2.57% (the same level of strain shown in the experimental results in Chapter 3.3.2). The value of $E_{m\_NNO\text{-}LAO}$ and $E_{m\_NNO\text{-}KTO}$ is 0.48 eV and 0.87 eV, respectively, which translates to ΔE_m of -0.39 eV. Furthermore, from Figure 5.1b, I estimated $\left(\frac{\Delta \ell^T_{NNO-LAO}}{\Delta \ell^T_{NNO-KTO}}\right)^2 \approx 3.50$. Thus, by inserting these values into Equation (6.5), I obtained the estimated diffusion enhancement at 300 K as $\left.\frac{D_{NNO-LAO}}{D_{NNO-KTO}}\right|_{300\ K} \approx 872$.

The estimated $\frac{D_{NNO-LAO}}{D_{NNO-KTO}}\Big|_{300\ K} \approx 872$ here is in the same order of magnitude of ~10^2 with the estimated $\frac{s_{NNO-LAO}}{s_{NNO-KTO}} \approx 134$. While they are in the same order of magnitude, it is noted that the estimated $\frac{D_{NNO-LAO}}{D_{NNO-KTO}}\Big|_{300\ K}$ is larger than the estimated $\frac{s_{NNO-LAO}}{s_{NNO-KTO}}$. This is because from Equation 6.5, $\frac{D_{NNO-LAO}}{D_{NNO-KTO}}\Big|_{300\ K}$ was estimated by using simulated or theoretical ΔE_m. The theoretical ΔE_m was simulated from ideal lattice mismatch, but the experimental lattice deformation from RSM results was smaller than the ideal lattice mismatch. Therefore, this causes ΔE_m and consequent $\frac{D_{NNO-LAO}}{D_{NNO-KTO}}\Big|_{300\ K}$ to be overestimated. In this regard, this estimation agrees well with the estimated switching speed enhancement. Moreover, these estimations verify my model about the relationship among lattice strain, diffusion constant, and switching speed in iontronic thin film devices. In particular, this also signifies the importance of my approach to tackle the long-standing issue in designing a reliable iontronic switching device, where the enhancement of switching speed is critically required. For instance, a stacked type rare-earth nickelate device prepared on Nb-$SrTiO_3$ substrate recorded ~10^{-7} s in switching speed (in Figure 1.8, ref. [7] of Chapter 1) even without substrate strain engineering. By integrating my strain engineering approach (~10^2 enhancement), a switching speed up to 10^{-9} s is expected in the future. In other words, this study can lead to a faster switching speed which is on a level with that of solid-state electronic device (~10^{-9} s), where it is required for future high-performance resistive switching device.

To summarize this study, through a sequence of experiments, I systematically established the fundamental correlation between lattice strain and proton diffusion in $RNiO_3$ perovskite lattice. Herein, the significance of strain control in determining the proton diffusion was revealed. Moreover, by utilizing the principle of this finding, I successfully demonstrated

a strain engineering for sophisticated control of proton motion within a solid lattice to achieve high-performance device functions. This established approach is not only practical to solve the long-standing issue in iontronic switching device field, but also can be useful for the development of variety of metal oxide electronics, whose peculiar properties are promising for emerging neuromorphic computing applications.

List of Publications

1. Scientific Journal

1.1) **Sidik, U.**; Hattori. A. N.; Hattori. K.; Alaydrus. M.; Hamada. I.; Pamasi. L. N.; Tanaka. H. Tunable Proton Diffusion in $NdNiO_3$ Thin Films under Regulated Lattice Strains. *ACS Appl. Elec. Mater.* **2022**, *4.10*, 4849-4856.

1.2) **Sidik, U.**; Hattori. A. N.; Li. H.B.; Nonaka. S.; Osaka. A.I.; Tanaka. H. Strain Effect on Proton-Memristive $NdNiO_3$ Thin Film Devices. *Appl. Phys. Exp.* **2023,** *16.1*, 014001.

2. Related Journal

2.1) Matsuzawa, I.; Ozawa, T.; Nishiya, Y.; **Sidik, U.**; Hattori. A. N.; Tanaka. H.; Fukutani. K. Controlling Dual Mott States by Hydrogen Doping to Perovskite Rare-Earth Nickelates. *Phys. Rev. Mat*. **2023**, *7.8*, 085003.

3. Conference: Oral Presentation

3.1) **Sidik, U.**; Hattori, A. N.; Tanaka, H. Strain-Regulated Proton Dynamics and Corresponding Proton-Induced Resistance Modulation in $NdNiO_3$ Thin Film. *Materials Research Meeting (MRM)*. Yokohama, Japan, Dec 13^{th}–17^{th}, 2021.

3.2) **Sidik, U.**; Hattori, A. N.; Tanaka, H. Dynamics of Electric Field-Assisted Hydrogenation in Proton-Doped $NdNiO_3$ Thin Film Resistors. *The 4^{th} International Conference on*

Memristive Materials, Devices & Systems (MEMRISYS). Tsukuba, Japan, Nov 01st–04th, 2021.

3.3) **Sidik, U.**; Hattori, A. N.; Tanaka, H. Proton Doping-Induced Resistance Modulation of $NdNiO_3$ Film under Electric Fields. *The 68th Japan Society of Applied Physiscs (JSAP)*. Tokyo, Japan, Mar 16th–19th, 2021.

3.4) **Sidik, U.**; Hattori, A. N.; Tanaka, H. Kinetics of Electric Field-Driven Proton Diffusion and Corresponding Metal-Insulator Phase Transition on $NdNiO_3$ Thin Film. *The 2020 Materials Research Society (MRS)*. Boston, USA, Nov 28th–Dec 04th, 2020.

3.5) **Sidik, U.**; Hattori, A. N.; Tanaka, H. Dynamics of Electric Field-Driven Proton Diffusion and Corresponding Resistance Modulation on $NdNiO_3$ Thin Films. *The 3rd Hydrogenomics Workshop*. Tokyo, Japan, Aug 20th–21st, 2020.

3.6) **Sidik, U.**; Hattori, A. N.; Tanaka, H. Effect of Electric Field-Assisted Hydrogenation on $NdNiO_3$ Thin Film Resistor. *The 67th Japan Society of Applied Physiscs (JSAP)*. Tokyo, Japan, Mar 12th–15th, 2020.

4. Conference: Poster Presentation

4.1) **Sidik, U.**; Hattori, A. N.; Tanaka, H. Kinetics of Electric Field Assisted-Hydrogenation in Proton Doped-$NdNiO_3$ Resistor. *The 2nd SANKEN International Symposium*. Awaji, Japan, Jan 9th–10th, 2020.

4.2) **Sidik, U.**; Hattori, A. N.; Tanaka, H. Dynamics of Proton-Doped Strongly Correlated $NdNiO_3$ Resistor. *11th International Symposium on Transparent Oxide and Related Materials for Electronics and Optics (TOEO)*. Nara, Japan, Oct 7th–9th, 2019.

Acknowledgements

I would like to thank the following people, without whom I would not have been able to complete this research, and without whom I would not have made it through my doctorate degree!

My academic supervisor, Prof. Hidekazu Tanaka, whose insight and knowledge into the subject matter steered me through this research. Thanks to his advice, encouragement, and stimulating discussion, I grew and matured in my scientific research and perspective. Thank you so much for giving me the chance to start my doctorate journey by letting me join your lab and enjoy my research life in Japan.

Special thanks to my co-academic supervisor, Prof. Azusa N. Hattori, who is always be there to support me whenever needed. No words can express my sincere gratitude to your steadfast support in research as well as in daily life, advice, valuable lesson, and friendship.

I'm deeply grateful to Tanaka-lab members who had been the internal support for the completion of this work: Thanks to Dr. Mahito Yamamoto, Dr. Ai I. Osaka, and Dr. Hao-Bo Li for their thoughtful advice. Fellow students in Tanaka-lab who had been friends in research and daily life: Boyuan Yu, Dr. Shingo Genchi, Hui Ren, Li, Akira Namba, Takashi Yamanaka, Shin Nonaka, Fumiya Endo, Jun Takigawa, Ryota Koizumi, Hirao, Yuki Taniguchi, Umezaki, and Masaki Tsutsumi. I would like to extent my gratitude to Mrs. Tomoko Okumoto for her helpful assistance in office administration, Michiko Sakuma and Saeko Tonda for their continuous experimental support. Their supports made me smoothly through my daily research activities. All staffs in Nanotechnology Open Facilities, Comprehensive Analysis Center, and Center of Innovation of Osaka University are also gratefully acknowledged.

I would also like to thank my colleagues across universities and faculties, without whom I have no complete content in my dissertation. Thanks to Prof. Ken Hattori, Prof. Shriram Ramanathan, Prof. Katsuyuki Fukutani, Dr. Ikutaro Hamada, Dr. Musa Alaydrus, Dr. Liliany N. Pamasi, Dr. Rupali Rakshit, Dr. Takahiro Ozawa, Dr. Osamu Nakagawara, Ikuya Matsuzawa, and Yusuke Nishiya.

And last but not least, my biggest thanks to my family for all the support they have shown me through this research, the culmination of years of learning. For my wife, Rita, thanks for all your support. You have been amazing, sorry for taking too much of our time together for the completion of this dissertation. For my mother, Emak, no words can express my feeling towards your patient and your faith in me. Thanks for always caring for me unconditionally. For my father, Bapak, I wish you were still here with us when I finally receive my PhD. You're still and will always be my inspiration. And finally, for all my brothers and sisters, thanks for always encouraging and supporting me whenever needed. Thanks for always believing in me!